SIMULTANEOUS PRODUCTION OF HIGH-PURITY HYDROGEN AND SEQUESTRATION-READY CO_2 FROM SYNGAS

Final Technical Report

Prepared By: Linda Denton (SIU), Hana Lorethova (SIU), Tomasz Wiltowski (SIU), Court Moorefield (GE-EER), Parag Kulkarni (GE-EER), Vladimir Zamansky (GE-EER) and Ravi Kumar (GE-EER)

December 2003

U.S. Department of Energy Contract No. DE-FC26-99FT40682

Contractor:

GE Energy and Environmental Research (GE-EER)

General Electric Company

18 Mason

Irvine, CA 92618

Subcontractor:

Southern Illinois University (SIU) at Carbondale

Department of Mechanical Engineering and Energy Processes

Carbondale, IL 62901

DISCLAIMER

ABSTRACT

This final report summarizes the progress made on the program "Simultaneous Production of High-Purity Hydrogen and Sequestration-Ready CO_2 from Syngas (contract number DE-FG26-99FT40682)", during October 2000 through September of 2003. GE Energy and Environmental Research (GE-EER) and Southern Illinois University (SIU) at Carbondale conducted the research work for this program.

This program addresses improved methods to efficiently produce simultaneous streams of high-purity hydrogen and separated carbon dioxide from synthesis gas (syngas). The syngas may be produced through either gasification of coal or reforming of natural gas. The process of production of H_2 and separated CO_2 utilizes a dual-bed reactor and regenerator system. The reactor produces hydrogen and the regenerator produces separated CO_2. The dual-bed system can be operated under either a circulating fluidized-bed configuration or a cyclic fixed-bed configuration. Both configurations were evaluated in this project. The experimental effort was divided into lab-scale work at SIU and bench-scale work at GE-EER.

Tests in a lab-scale fluidized bed system demonstrated the process for the conversion of syngas to high purity H_2 and separated CO_2. The lab-scale system generated up to 95% H_2 (on a dry basis). Extensive thermodynamic analysis of chemical reactions between the syngas and the fluidized solids determined an optimum range of temperature and pressure operation, where the extent of the undesirable reactions is minimum. The cycling of the process between hydrogen generation and oxygen regeneration has been demonstrated. The fluidized solids did not regenerate completely and the hydrogen purity in the reuse cycle dropped to 70% from 95% (on a dry basis). Changes in morphology and particle size may be the most dominant factor affecting the efficiency of the repeated cycling between hydrogen production and oxygen regeneration.

The concept of simultaneous production of hydrogen and separated stream of CO_2 was proved using a fixed bed 2 reactor system at GE-EER. This bench-scale cyclic fixed-bed reactor system designed to reform natural gas to syngas has been fabricated in another coordinated DOE project. This system was modified to reform natural gas to syngas and then convert syngas to H_2 and separated CO_2. The system produced 85% hydrogen (dry basis).

TABLE OF CONTENTS

LIST OF FIGURES

LIST OF TABLES

1.0 – INTRODUCTION

GE Energy and Environmental Research (GE-EER) and Southern Illinois University (SIU) at Carbondale conducted work on the project titled, "Simultaneous Production of High-Purity Hydrogen and Sequestration-Ready Carbon Dioxide from Syngas." This research work was sponsored by the U.S. Department of Energy (DOE) under contract number DE-FG26-99FT40682. This project develops a method to efficiently and simultaneously produce streams of high-purity hydrogen (H_2) and sequestration-ready carbon dioxide (CO_2) from syngas that may be produced from either gasification of coal or reforming of natural gas.

The objective of this project was to design and build a bench-scale dual-bed reactor/regenerator system for the production of high-purity H_2 and sequestration-ready CO_2. The specific objectives for this project are identified by task as follows:

Task 1: Laboratory evaluation of the process

The objective of this task was to conduct a laboratory scale demonstration of each of the individual sub-processes involved in converting syngas to separate streams of H_2 and CO_2. A thermo-gravimetric analysis system, an ambient-pressure fluidized-bed reactor system, and an ambient-pressure fixed-bed reactor system were used to identify optimum operating temperatures for the reactions.

Task 2: Engineering and economic assessment of the process

The objective of this task was to assess the engineering and economic feasibility of the proposed process. An analytical model of the complete process and the individual unit operations (such as reactors, compressors, expanders and heat exchangers) was developed. Several process flow diagrams (PFD) were developed and an optimal system configuration, with an efficiency of around 84%, was selected. If natural gas were injected then the process efficiency would be as high as 92%. The economic feasibility analysis showed that the cost of producing hydrogen along with sequestration-ready carbon dioxide is around $1.7 per kg.

Task 3: Materials evaluation

The overall objective of this task is to develop materials for CO_2 separation, H_2 production, and isolation of contaminants from the product H_2 stream.

Task 4: Process design and development

The overall objectives of this task are process optimization, cost projections, design of a bench-scale system for demonstration of the process under dynamic conditions, and a preliminary system analysis for a full-scale plant.

Task 5: Bench scale demonstration

The objective of this task will be to collect data on process operation under dynamic conditions. Bench-scale systems that are being fabricated in other DOE programs will be modified.

This is the final report of the program. The work performed was on Tasks 1-5. The full details of the final report follow.

2.0 – EXECUTIVE SUMMARY

GE Energy and Environmental Research (GE-EER) and Southern Illinois University (SIU) at Carbondale conducted work on the project "Simultaneous Production of High-Purity Hydrogen and Sequestration-Ready CO_2 from Syngas." The U.S. Department of Energy (DOE), under contract number DE-FG26-99FT40682, sponsored this work. The project developed a process for producing separate streams of high-purity hydrogen and carbon dioxide from synthesis gas (syngas). In this project the syngas was generated from reforming of natural gas; however, it can also be produced from gasification of coal.

The process studied in this research project utilizes a dual-bed reactor and regenerator system fed with syngas and oxygen. The reactor produces hydrogen and the regenerator produces CO_2 stream. The dual-bed system can be operated under either a circulating fluidized-bed configuration or a cyclic fixed-bed configuration. Both configurations were evaluated in this project.

Tasks 1 and 2 of the program "Laboratory evaluation of the process involved" and "Engineering and economic assessments of the process" were completed during DOE FY2000. In these tasks, lab-scale systems were used to identify the optimum operating temperature for producing separate streams of hydrogen and CO_2. An analytical model of the process was developed. The economic analysis estimated that the cost of producing hydrogen with sequestration ready carbon dioxide is \$1.70 per kg of H_2.

Task 3 "Evaluation of materials" was initiated by SIU in DOE FY2001. Experimental studies were conducted to determine the optimum fluidization conditions for calcium and iron oxide mixtures. It was determined that particle diameters with a sieve cut of 75-106 μm would fluidize at acceptable gas flow rates without hindering the effectiveness of the catalytic reactions. A fluidized-bed system was fabricated for materials evaluation and is capable of withstanding up to 820°C and 35 atm. In the hydrogen production experiments a simulated syngas stream, composed of 44% CO, 23% steam and 33% hydrogen was fed to the fluidized bed reactor that was filled with a mixture of Fe_2O_3 and CaO. The syngas reduced the Fe_2O_3 to FeO. The CO_2 produced was captured by CaO to form $CaCO_3$. In the regeneration step, air was fed into the fluidized bed reactor, to reoxidize the FeO to Fe_2O_3. In the regeneration step experiments $CaCO_3$ was converted back to CaO, releasing CO_2. The lab-scale system successfully demonstrated the conversion of syngas to high purity H_2 and sequestration ready CO_2, over a fluidized bed of Fe_2O_3 and CaO. Hydrogen purity reached levels greater than 95% on a dry basis.

The concept of hydrogen generation and oxygen regeneration was also demonstrated using the lab scale system. A two-step cycling test was performed, where a mixture of syngas was fed over the catalyst, and the bed was then regenerated by flowing air. Finally, the syngas was again fed over the regenerated Fe_2O_3 / CaO mixture. Up to 95% pure hydrogen on a dry basis was obtained in the hydrogen production step. After the oxygen regeneration step, the hydrogen purity fell to approximately 70% in the hydrogen production step of the second cycle. Possible causes for the decline in hydrogen purity include the non-optimized temperature and pressure conditions, and morphological changes in the iron oxide and CaO particles. Further study demonstrated the need for low pressure, high temperature regeneration that would eliminate the agglomeration of the catalyst.

Tasks 4 and 5 "Process design and development" and "Bench scale demonstration" were performed by GE-EER in coordination with the independent DOE Program: "Conversion of Natural Gas to PEM Fuel Cell Grade H_2", Contract # DE-FC02-97EE50488 from the Office of

Power Technologies, under the Fuel Cells for Buildings program. Under the DOE project, syngas was generated using the natural gas to hydrogen reformer, which is based on autothermal cyclic reforming (ACR) technology. The concept of simultaneous generation of high purity hydrogen and sequestration ready CO_2 stream was proved by modifying the ACR based fuel processor. The first reactor of the bench scale system was filled with reforming catalyst and the second downstream reactor was filled with a mixture of Fe_2O_3 and CaO. A temperature swing from 550°C to 850°C in the second bed was required to adsorb CO_2 and to regenerate $CaCO_3$. This was achieved using intermittent burners. The system successfully demonstrated the conversion of CO to CO_2 and the capture of CO_2. Dry hydrogen concentrations increased from 65% to 85% across the reactor filled with CaO and Fe_2O_3.

The technology of producing separate streams of high purity hydrogen and CO_2 from syngas is very promising. The results obtained from the lab scale and the bench scale systems and the economic analysis are promising and suggest that the technology meets the DOE targets of cost and efficiency.

3.0 – EXPERIMENTAL

3.1 Lab Evaluation, Materials Evaluation, and Process Development (Tasks 1, 3, 4)

3.1.1 Description of Thermogravimetric Analysis (TGA)

Ferric oxide samples (both fine and coarse grade) of greater than 99 % purity supplied and certified by J. T. Baker, Inc. were used in this study. Particle size distribution measurements were performed using the Microtrac laser particle analyzer (Leeds and Northrup Instruments, Model 7995-10). The average of 5 measurements shows that the median sizes of the fine (powder) and coarse (particle) samples were 1.22 μm and 58.6 μm, respectively. The average specific surface areas of the fine and coarse samples, as determined by a BET analyzer, were estimated to be 5.2 m^2/cm^3 and 0.37 m^2/cm^3, respectively. The thermogravimetric analyses of the gaseous reduction of the fine and coarse ferric oxide samples were accomplished using a Perkin Elmer TGA-7 analyzer. The solid samples were preheated to a desired temperature under an inert gas atmosphere of nitrogen, followed by the introduction of carbon monoxide. Experiments were carried out at temperatures between 800 – 900^oC.

3.1.2 Description of Cold Flow Fluidized Bed Modeling

When a gas is passed upward through a bed of fine, solid particles, the system has been found to consistently pass through several phases. At the point at which the solids are just suspended in the flow, the bed is considered fluidized. A higher inlet gas flow rate will create more vigorous solid motion and the bed is considered to be a bubbling fluidized bed. The last phase of any fluidized bed, entrainment, occurs when the gas flow rate is high enough to carry solids out of the bed.

Measurement of values for minimum fluidization velocity, bubbling velocity and initiation of entrainment/elutriation are normally made using the pressure drop across the bed, along with visual observations where possible. Ideally the pressure drop across the bed increases proportionally with gas velocity until the point of fluidization, where it remains fairly steady until the point of elutriation and solids begin leaving the reactor.

Several anomalies can affect the operation of the fluidized bed. Slugging is a result of a coalescence of the gas bubbles, until a large bubble with a diameter equal to the bed diameter forms beneath the solid. The solid is carried upward as a whole until the bubble pops and the particles rain downward. This usually occurs in narrow beds and can be determined by an extreme fluctuation in bed pressure drop as the bubble expands, moves the bed and disintegrates. Channeling occurs when the gas flows through an isolated area of the solid bed and contact between the two phases is limited. Other problems occur with mixtures of particles with narrow size cuts of diameter ratios greater than 6:1. The smaller particles may fluidize in the spaces between the larger particles. Also, actual particle diameters involved in a real application will change with time due to physical attrition and chemical changes.

Pressure drop across the bed can be related to gas flow linear velocity, particle diameter and bed geometry by the Ergun equation, as described in the results section. The minimum fluidization velocity of gas needed for particles of a given diameter and Reynolds number less than 20 can be simplified to be

$$u_{mf} = \frac{d_p^2(\rho_s - \rho_g)g}{1650\mu} \qquad (1)$$

Terminal velocity is estimated from the free-fall velocity of the particle as described in results section.

For mixtures of particles with a varying size distribution, the mean particle diameter is determined as a weighted average dependent upon the surface area of a sphere with the same diameter.

Minimum bubbling fluidization velocity was found using the model in CGS units suggested by Abrahamsen and Geldart, (as cited by Gupta & Sathiyamoorthy [5]):

$$u_{mb} = 100\bar{d}_p \qquad (2)$$

Studies by Baeyens and Geldart (as cited by Yates [6]), found that slugging was not significantly affected by particle size and size distribution, but that a ratio between bed height and bed diameter was a determining factor in the formation of slugs. The critical bed height (in centimeters) was described as:

$$L = 60D^{0.175} \qquad (3)$$

In beds with height less that critical, the minimum slugging velocity (in cm/s) can be found by:

$$u_{ms} = 0.07(gD)^{1/2} + 1.6x10^{-3}\left(L - L_{mf}\right) + u_{mf} \quad (4)$$

For bed depth greater than the critical value, the minimum slugging velocity can be modeled as:

$$u_{ms} = 0.07(gD)^{0.5} + u_{mf} \quad (5)$$

The bed in this study operated at a bed height of approximately 15 cm, well below the critical bed height of 70.6 cm for a one-inch diameter reactor.

3.1.3 Cold Flow Fluidized Bed Equipment and Instrumentation

This study was designed to investigate the fluidization characteristics of hematite (Fe_2O_3), limestone ($CaCO_3$) and lime (CaO), separately and in mixtures, under atmospheric pressure and room temperature, in order to model their behavior separately and in mixture under high pressure/high temperature conditions.

A sealed glass tube of diameter 6.37 cm was fitted with a porous glass frit to serve as the reactor model. Solids were introduced into a port at the top of the reactor, which was then sealed. Nitrogen was used as the fluidizing medium, with flow rates monitored by a Cole-Parmer rotameter for low flows and a Gilmont rotameter for high flows. Differential pressure across both the diffuser and bed was measured with a water-filled manometer for low flows and a Capsuhelic Differential Pressure Gage for high flows. The pressure drop across the frit at various flow rates was measured separately and removed from the experimental differential pressure to determine the pressure drop across the particle bed. A Hastelloy thermocouple inserted into the center of the glass tube monitored temperature. Hematite, limestone and lime samples were sieved to separate particles of different diameters. Particle sizes were measured by a Microtrac Particle size Analyzer capable of measuring diameters from 0.7 to 125 microns. Bed height and diameter were measured with a vernier caliper of least count 0.001 cm.

3.1.3.1 Experimental Set-up

Particle sizes and mixture combinations are described in Table 1. A low-flow setup was utilized in the first part of the study to determine the pressure drop across the bed and to find the minimum fluidization of each individual compound visually, as well as graphically. Ferrous oxide and calcium oxide in a 1:2 mass proportion were then layered and mixed under the low-flow set-up. Finally, Ferrous oxide, calcium oxide and calcium carbonate were layered in a 1:1:1 mass ratio to observe fluidization behaviors at low flow.

Qualitative observations indicated that channeling and slugging were problems that could be overcome at higher fluidization velocities. The high flow set-up was used to qualitatively and quantitatively study behaviors of individual compounds and layered mixtures under those conditions most closely related to actual reactor conditions, although temperature and pressure were still limited to 1 atmosphere and 20°C.

Solid	Compound Density (g/cm^3)	Mean Particle Size (μm)	Standard deviation (μm)	Mass Ratio for Mixture #1	Mass Ratio for Mixture #2
Fe_2O_3	5.24	20.18	11.23	1	1
CaO	3.34	11.54	8.72	2	1
$CaCO_3$	2.71	23.73	17.41	0	1

Table 1: Solid Particle Characteristics – Cold Flow Fluidization Study

3.1.4 Pressurized Fluidized Bed

A fluidized bed reactor capable of withstanding temperatures of 820°C and pressures of 35 atmospheres was constructed of INCONEL 800 HT. It consisted of a three inch double extra heavy gauge exterior pipe, with a suspended schedule 40 INCONEL one inch pipe serving as the actual reactor as shown in Figure 1. The interior pipe was welded and sealed to a flange, which was sandwiched between two 3", 900-pound flanges welded to the exterior pipe and outlet tube with details shown in Figure 2. The design allowed for the use of graphite spiral wound gaskets to seal the 900-pound flanges at each end of the reactor, by keeping the flange temperature below 400°C through radiation and convective cooling. The one inch suspended pipe contained a quartz frit welded between two plates to act as a diffuser for the inlet gas, with frit housing shown in Figure 3. The internal pipe was completely removable, and experienced little differential pressure. The outlet products of the fluidized bed passed through the inner pipe, and to the analysis branch. The seal between the inner and outer pipe was assured by welding the inner pipe to a raised face flange (Figure 4) and sealing to the top flange with a graphite gasket (Figure 5). A crane was used to position the reactor for suspension on a steel support (Figure 6). The reactor was heated with a custom high- temperature ceramic furnace and add-on pre-heater, as shown in Figure 7. The furnace heated a 41-inch length of the reactor beginning 47 inches

below the top flange. This allowed the inlet gas to be heated in a 28-inch length of the reactor before entering the fluidized bed area. The estimated, maximum bed height of 7 inches was designed to be contained within the highest temperature area of the reactor, heated by the custom ceramic furnace. This allowed a 41-inch length of pipe to cool the gas stream and to provide a disengagement zone by slowing of the exiting gas velocity. Initial testing and observations during experimentation supported the cooling design, with the topmost flanges operating near room temperature at most gas flowrates, and minimum elutriation of solids.

The preheater provided a constant 400^{o}C for the 18 inches at the inlet to preheat the entering gas and to also provide steam for the reactor. Water entered through a nine-inch long, ¼" diameter stainless steel pipe constructed within the preheated zone shown.

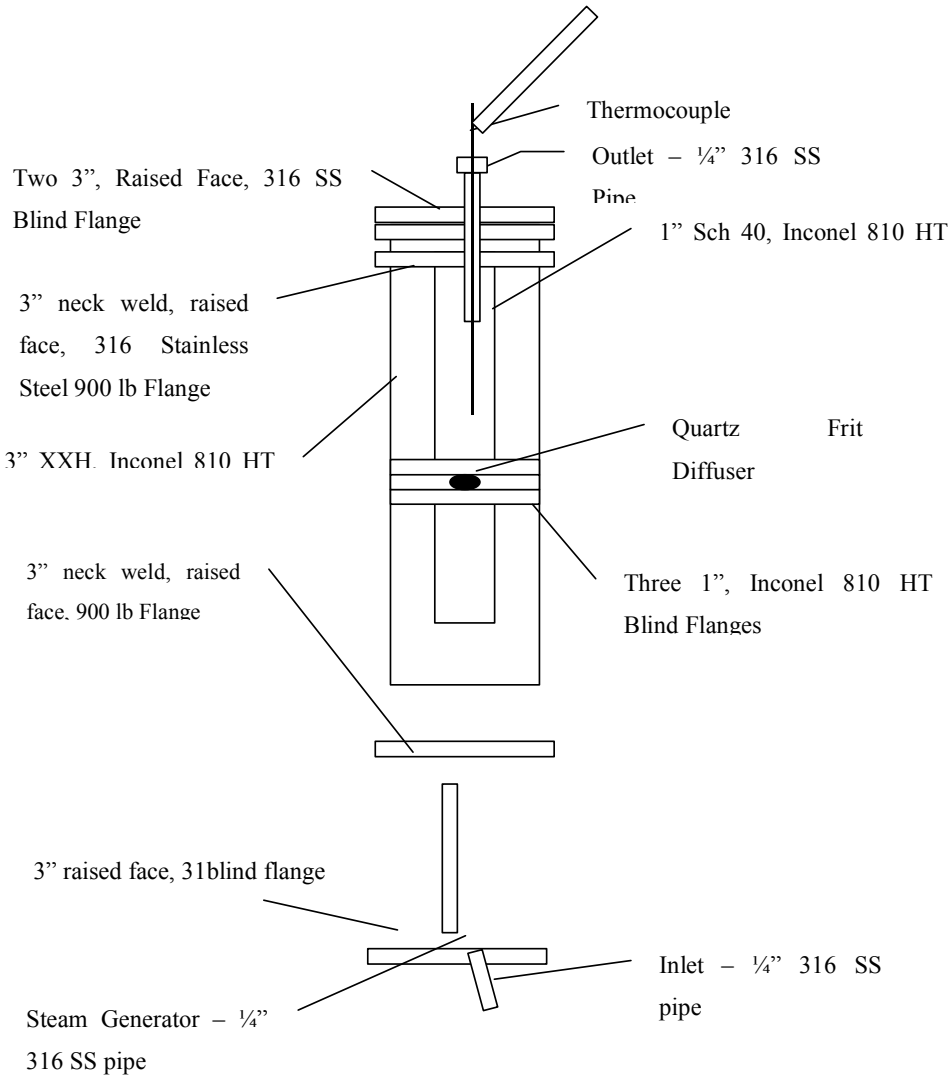

Figure 1: Fluidized Bed Reactor Schematic

Three-inch XXH Pipe Dimensions:

3.5 in o.d.

2.3 in i.d.

One-inch Schedule 40 Pipe Dimensions:

1.315 in o.d.

1.049 in i.d.

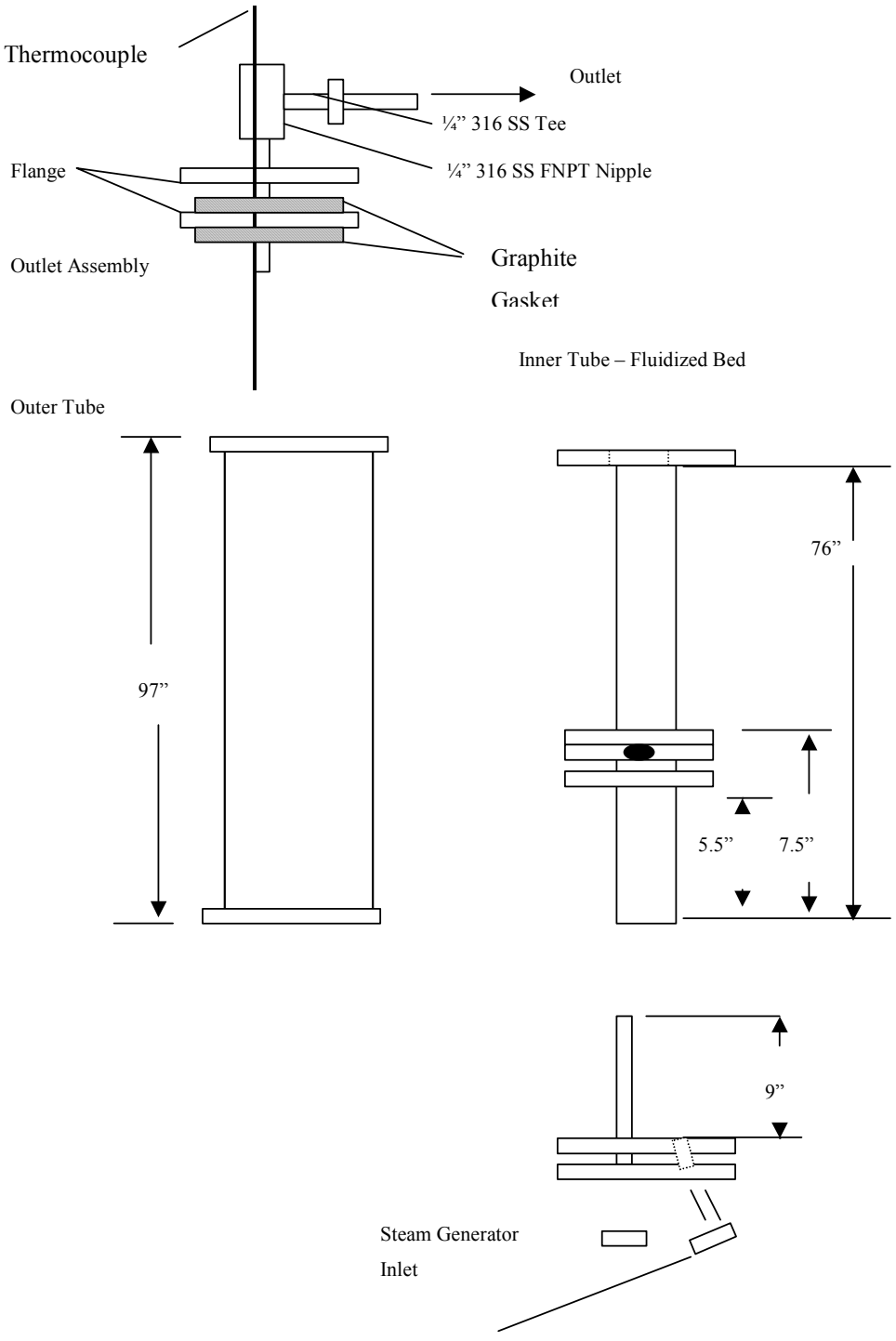

Figure 2: Section Details - Reactor

Figure 3: Frit Housing of Fluidized Bed Reactor

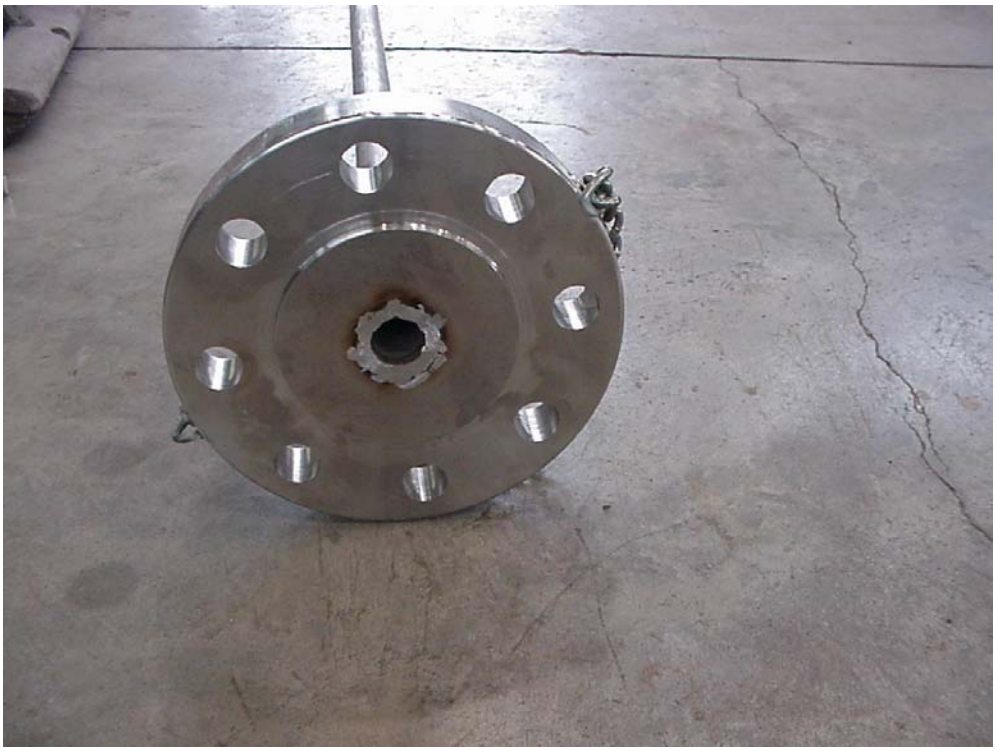

Figure 4: Top Flange of Inner Tube of Fluidized Bed Reactor

Figure 5: Inner Tube of Fluidized Bed Reactor with Top Flange and Outlet Pipe

Figure 6: Installation of Inner Tube in Reactor

Figure 7: Assembled and Mounted Fluidized Bed Reactor, Furnace and Preheater

in Figure 8, which allowed the inlet water to reach a temperature above the condensation point before entering the outer tube of the reactor. Water was introduced into the system by a high pressure metering piston pump with minimum flow rate output of 0.1 ml/min, maximum output of 3.0 ml/min and accuracy of +/- 0.3% full scale.

Gas was provided to the inlet stream through the use of high-pressure tanks. Sierra 820 Series Top-Track Mass Flow Meters and metering valves controlled the inlet flow rate of all inlet gases. Nitrogen was used as a low-pressure purge. The mass flowmeters, when used with a single gas, provided an accuracy of 1.5% of full scale, but when used with the syngas mixture had an accuracy between 5% and 10%. The outlet flowrate was measured with a Sierra 820 Series Mass Flow Meter for a portion of the experiments and a Gilmont Accucal variable area flowmeter, with a +/- 10% maximum error.

Figure 8: Steam Generator Located in Bottom Flange of Reactor

3.1.5 Adsorption and Regeneration of Solids

Ferric oxide particles, 100 μm in diameter, were mixed with 20 μm diameter calcium oxide particles and placed in a one inch diameter fluidized bed constructed of INCONEL 810 HT with a quartz diffuser. Total mass of the solids was 50 grams at a 1:7 ferric oxide to calcium oxide mass ratio. A mixture of 44% hydrogen, 33 % carbon monoxide and 23% steam (by volume), was introduced for five minutes to the sorbents at a linear flow rate of fifteen times the minimum fluidization velocity for the ferric oxide particles, and at a temperature of 670°C and pressure of 250 psi. This was followed by a nitrogen purge for 55 minutes and a reactor temperature reduction to 580°C. A dry oxygen flow of fifteen times minimum fluidization velocity was introduced to allow the sorbents to regenerate. After fifteen minutes, the reactor was again purged with nitrogen. After 90 minutes, and a temperature increase of the reactor to 700°C, the syngas mixture was reintroduced for fifteen more minutes for the second hydrogen generation cycle. Nitrogen was used for thirty more minutes as a purge.

3.2 Bench Scale System CO_2 Separation of Syngas with a Fixed Bed (Task 5)

A 200 kW (thermal) bench-scale syngas production unit designed for integration with a Proton Exchange Membrane (PEM) fuel cell was fabricated and successfully operated on natural gas. This work was conducted through an independent DOE grant ("Conversion of natural gas to PEM Fuel Cell grade H_2", Contract # DE-FC02-97EE50488) from the Office of Power Technologies, under the Fuel Cells for Buildings Program. A picture of the 200 kW natural gas reformer is shown in Figure 9. The bench-scale unit utilizes two fixed-bed reactors to produce syngas from natural gas.

The bench-scale system is currently operating with independent funding from the DOE Office of Power Technologies ("Conversion of natural gas to PEM Fuel Cell grade H_2", Contract # DE-FC02-97EE50488).

The bench-scale system utilizes the Autothermal Cycling Reforming (ACR) process. The ACR process is an advanced GE patented technology and has been successfully demonstrated using high-sulfur diesel fuel and natural gas as feed-stocks to generate syngas. ACR utilizes two fixed bed reactors loaded with NiO to reform natural gas to syngas.

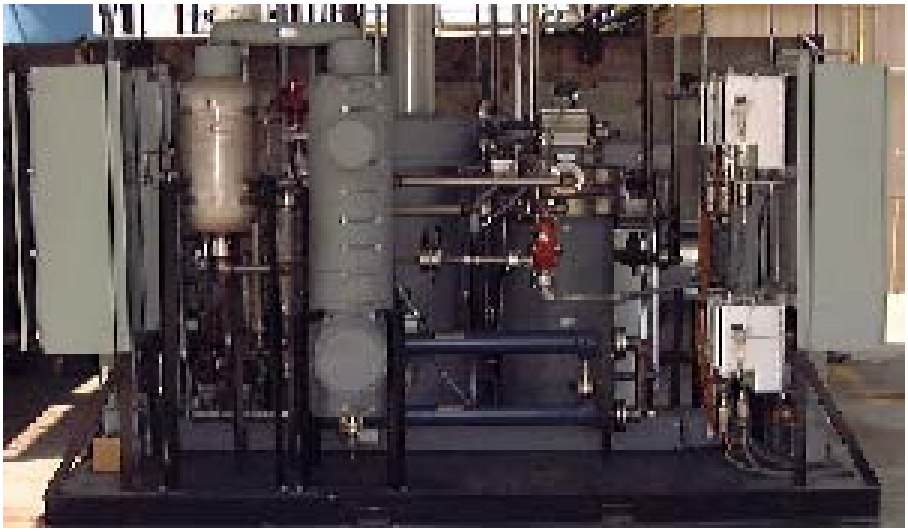

Figure 9: Top: Bread-board 100 kW H_2 Production Unit. Bottom: Modified Prototype 200 kW H_2 Production Unit (From DOE Grant "Conversion of Natural Gas to PEM Fuel Cell Grade H_2", Contract # DE-FC02-97EE50488)

3.2.1 Modifications to the Bench Scale System

The ACR prototype system was modified to reform natural gas to syngas in the first bed and to convert syngas to H_2 and CO_2 in the second bed. Reactor 1 was loaded by Ni (reforming catalyst) and the downstream reactor 2 was loaded by Fe_2O_3 and CaO. As shown in Figures 10

and 11, each reactor repeatedly cycles between the three steps of the process: reforming, air regeneration and fuel reduction.

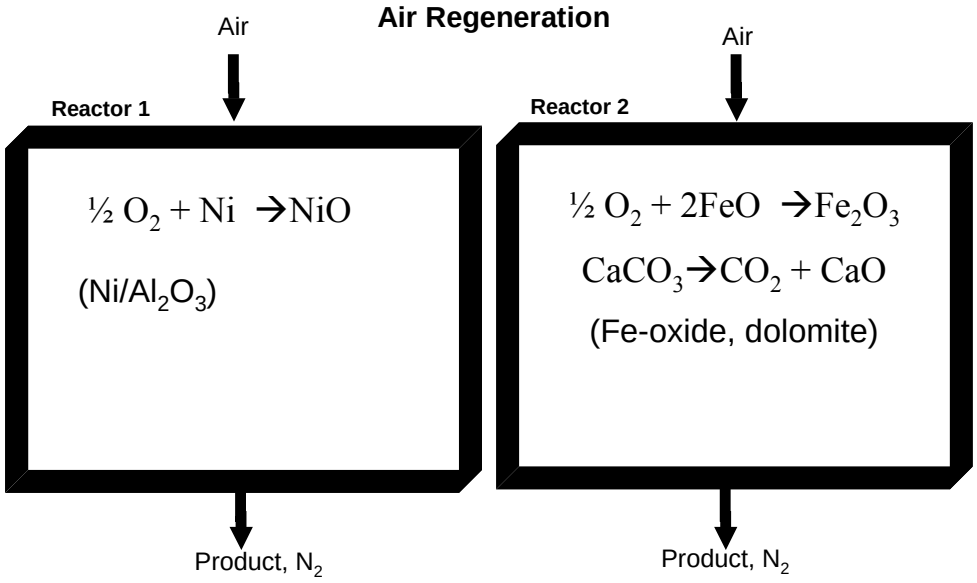

Figure 10: Illustration of the Autothermal Cyclic Reforming (ACR) Process: Air Regeneration step

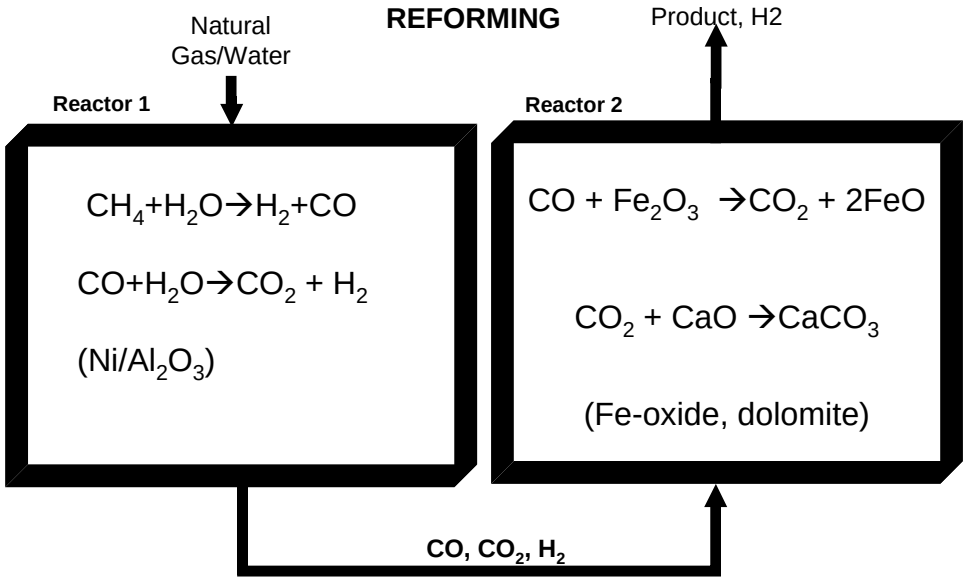

Figure 11: Illustration of the Autothermal Cyclic Reforming (ACR) Process.

During the endothermic reforming step (see figure 11), fuel and steam react over the Ni catalyst in the first reactor bed to produce syngas through conventional steam methane reforming

(SMR) chemistry. In the second reactor bed, Fe_2O_3 and CaO are used to convert CO to CO_2 as well as to adsorb CO_2, converting CaO to $CaCO_3$.

During the exothermic regeneration step, oxygen is passed through the packed bed to oxidize Ni in the first bed and oxidize FeO in the second the bed (figure 10). During the regeneration step any sulfur that is adsorbed during the reforming step is oxidized and released as SO_2, separately from the syngas. At the same time $CaCO_3$ is converted back to CaO, releasing the CO_2. The heat released by the oxidation reactions raises the temperature of the packed bed, thus providing heat for the endothermic reforming step. In addition, some of the released heat is utilized for the release of CO_2 from $CaCO_3$, which is an endothermic reaction.

In the mildly endothermic fuel reduction step, fuel is introduced to the packed bed. By adding the appropriate amount of fuel, only NiO in the upstream portion of the bed is reduced back to the elemental Ni form. Two reactors and switching valves are required to produce a continuous stream of H_2 and CO_2 by repeatedly cycling between the three steps. When one reactor is in the reforming step (~10 mins) the other reactor is in either the air regeneration step (~6 mins) or the fuel reduction step (~4 mins). In summary, the primary reactions that occur during each step are as follows:

Reforming Step (Endothermic; Syngas formation over nickel catalyst, followed by CO_2 formation over Fe_2O_3 and $CaCO_3$ production from CaO and CO_2)

$CH_4 (g) + H_2O (g) \rightarrow CO (g) + 3\ H_2 (g)$ $\quad \Delta H_{rxn} = 205$ kJ/mol

$CO (g) + H_2O (g) \rightarrow CO_2 (g) + H_2 (g)$ $\quad \Delta H_{rxn} = -41.2$ kJ/mol

$CO (g) + Fe_2O_3 (s) \rightarrow CO_2 (g) + 2\ FeO (s)$ $\quad \Delta H_{rxn} = 1.3$ kJ/mol

$CaO (s) + CO_2 (g) \rightarrow CaCO_3 (s)$ $\quad \Delta H_{rxn} = -166.3$ kJ/mol

Air Regeneration Step (Exothermic; Ni oxidation, followed by FeO oxidation to Fe_2O_3 and CO_2 release, converting the $CaCO_3$ back to CaO).

$Ni (s) + 1/2\ O_2 (g) \rightarrow NiO (s)$ $\quad \Delta H_{rxn} = -244$ kJ/mol

$2\ FeO (s) + ½\ O_2 (g) \rightarrow Fe_2O_3 (s)$ $\quad \Delta H_{rxn} = -279$ kJ/mol

$CaCO_3 (s) \rightarrow CaO (s) + CO_2 (g)$ $\quad \Delta H_{rxn} = 166.3$ kJ/mol

Fuel Reduction Step (Endothermic; Nickel oxide only reduction to elemental Ni)
$NiO\ (s) + 1/4\ CH_4\ (g) \rightarrow 1/4\ CO_2\ (g) + 1/2\ H_2O\ (g) + Ni\ (s) \quad \Delta H_{rxn} = 44\ kJ/mol$

The above reactions show that the reforming (production of syngas from natural gas) and syngas separation (adsorption of CO_2) steps can be combined by loading appropriate amounts of NiO, FeO and CaO in the two fixed bed ACR reactors and by cycling between the steam reforming step, regeneration step and fuel reduction steps. In this configuration syngas is first generated from natural gas by reforming. The CO in the syngas is then converted to CO_2 and finally CO_2 is separated from the syngas, so that pure hydrogen is produced from natural gas.

Thus the bench-scale 200 kW syngas production unit (From DOE Grant "Conversion of natural gas to PEM Fuel Cell grade H_2", Contract # DE-FC02-97EE50488) can be used for the production of high purity H_2 and sequestration-ready CO_2 by adding FeO and CaO in the downstream portion of the catalyst bed.

4.0 – RESULTS AND DISCUSSION

4.1 TGA Results (Task 1)

4.1.1 TGA Introduction

This portion of the work presents the evaluation of the kinetics of Fe_2O_3 reduction at high temperatures in a continuous stream of pure carbon monoxide. In addition to the reduction to wusite and metallic iron, carbon monoxide disintegration by the reverse Boudouard's reaction [7, 8] and carbidization [9, 10, 11] are expected to occur simultaneously. A thermodynamic analysis indicates that relatively low temperatures (less than 1000 ^oC) and high CO concentrations along with the presence of metallic iron lead to carbon deposition (Figure 12). Increase in temperature and CO concentration leads to reduction in iron oxides.

The reduction of iron oxide and various ores containing iron oxide have been studied in the past [12-26]. Various controlling mechanisms have been suggested in their research. Shimokawabe [12] suggested a random nucleation mechanism for the reduction of hematite (Fe_2O_3) while phase boundary mechanism was evoked in Sastri *et al.*'s research [13]. In 2001, Tiernan *et al.* [24] concluded that reduction of hematite to magnetite (Fe_3O_4) was via phase boundary while that of magnetite to free iron was via random nucleation. El-Geassy's work [18]

on the reduction of hematite at temperatures ranging between 1173 – 1473 K concluded that the reduction of hematite to wusite (FeO) was controlled by a mixed reaction mechanism in the early stages followed by interfacial chemical reaction while the reduction of wusite to iron was controlled by a mixed chemical reaction. Similar conclusions were arrived at by Moon *et al.* [19, 20]. An experimental study on the kinetics of reduction of iron oxide in a fluidized bed reactor [22] showed the existence of two stages of reduction. In the first stage, the rate of reduction was controlled by mass transport in the gas phase and in the second stage, the rate-controlling mechanism was chemical reduction within small grains of the iron ore particles. Ishii *et al.* [14] found that the reduction of Fe_2O_3 was 10 times faster in H_2 atmosphere as compared to CO atmosphere. In 1997, Moon and Rhea [19] estimated that the reaction rate for Fe_2O_3 reduction with CO was 2-3 times lower than that with H_2. They estimated the value of the apparent activation energy for iron oxide reduction to be 14.6 kJ/mol in a carbon monoxide atmosphere. In a later work [20], they estimated the activation energy for the reduction reaction in CO to be 19.8 kJ/ mol in pure CO stream, the value of which increased with reducing CO partial pressure in a CO-H_2 gas stream. The value of the activation energy was found to be 42.1 kJ/mol in a 100% hydrogen atmosphere. Table 2 lists the activation energies for iron oxide reduction in various reducing atmospheres reported in the literature.

The focus of this research is to investigate these reaction conditions that result in the oxidation of carbon monoxide to carbon dioxide. Carbon dioxide can subsequently be removed by lime. A plot of the Gibbs free energy change with temperature is shown in Figure 13. The data show that the reduction of hematite to wusite is favored at high temperatures. However, the capture of carbon dioxide via lime is generally favored at temperatures less than 900^{o}C. Nonetheless, the temperature window of 725–900^{o}C affords thermodynamically favorable reaction conditions for both the oxidation of CO to CO_2 using iron oxide and the subsequent sequestration of CO_2 by lime. In addition, carbon monoxide disintegration and iron carbide formation is not thermodynamically favored at temperatures greater than 725^{o}C. Hence, in this investigation, the temperature range of 725–900^{o}C was studied for the oxidation of CO. A kinetic model was developed and the data from thermogravimetric experiments were fitted to the model to extract the numerical values for the reaction rate parameters. X-ray diffraction analysis was used to identify the various products of the reaction.

Reference	Activation Energy kJ/mol	Reducing agent
Shimokawabe *et al.* [6]	74-117	H_2
Sastri *et al.* [7]	57-73	H_2
Moon and Rhea [13]	35	H_2
Moon and Rhea [13]	14.6	CO
Moon *et al.* [14]	42.1	H_2
Moon *et al.* [14]	19.8	CO
Tiernan *et al.* [18]	96-106	H_2

Table 2: Activation Energies For Iron Oxide Reduction Reported in Literature

% 16 percentile (μm)	% 50 percentile (μm)	% 84 percentile (μm)	Mean Diameter (μm)	Surface Area (m^2/cm^3)	Standard Deviation
Fe_2O_3 fine sample (powder)					
0.81	1.22	1.69	1.2	5.2	0.44
Fe_2O_3 coarse sample (particles)					
15.84	58.58	97.75	57.8	0.37	41

Table 3: Particle Size Measurements.

CASE	B	C	C_1	C_2
I $\alpha \neq 1$ (a) $\beta \neq 1$ $\alpha \neq \beta$	$\frac{2}{\alpha-1}A_o e^{-k_1 t} + C_1 e^{-\alpha k_1 t}$	$\frac{2\alpha Ao}{(\alpha-1)(\beta-1)}e^{-k_1 t} + \frac{\alpha C_1}{\beta-\alpha}e^{-\alpha k_1 t}$ $+ C_2 e^{-\beta k_1 t}$	$B_o - \frac{2A_o}{\alpha-1}$	$C_o - \frac{2\alpha A_o}{(\alpha-1)(\beta-}$ $-\frac{\alpha C_1}{\beta-\alpha}$
(b) $\beta = 1$;	Same as above	$\frac{2\alpha k_1 A_o t e^{-k_1 t}}{\alpha-1} - \frac{\alpha C_1}{\alpha-1}e^{-\alpha k_1 t} + C_2 e^{-k_1}$	Same as above	$C_o - \frac{\alpha C_1}{1-\alpha}$
(c) $\alpha = \beta$ $\beta \neq 1$	Same as above	$\frac{2\alpha A_o}{(\alpha-1)}e^{-k_1 t} + \alpha k_1 C_1 t e^{-\alpha k_1 t} + C_2 e^{-\alpha k}$	Same as above	$C_o - \frac{2\alpha A_o}{(\alpha-1)^2}$
II $\alpha = 1$ (a) $\beta \neq 1$	$2k_1 A_o t e^{-k_1 t} + C_1 e^{-k_1 t}$	$\frac{2A_o}{\beta-1}e^{-k_1 t}\left(k_1 t - \frac{1}{\beta-1}\right) + \frac{C_1}{\beta-1}e$ $+ C_2 e^{-\beta k_1 t}$	B_o	$C_o + \frac{2A_o}{(\beta-1)^2} - \frac{C_1}{\beta-1}$
(b) $\alpha = \beta$	Same as above	$\frac{k_1}{2}(2k_1 A_o t + C_1)te^{-k_1 t} + C_2 e^{-k_1 t}$	B_o	C_o

$\alpha = k_2/k_1$, $\beta = k_3/k_1$

Table 4: Expressions For Concentration of *B* and *C*.

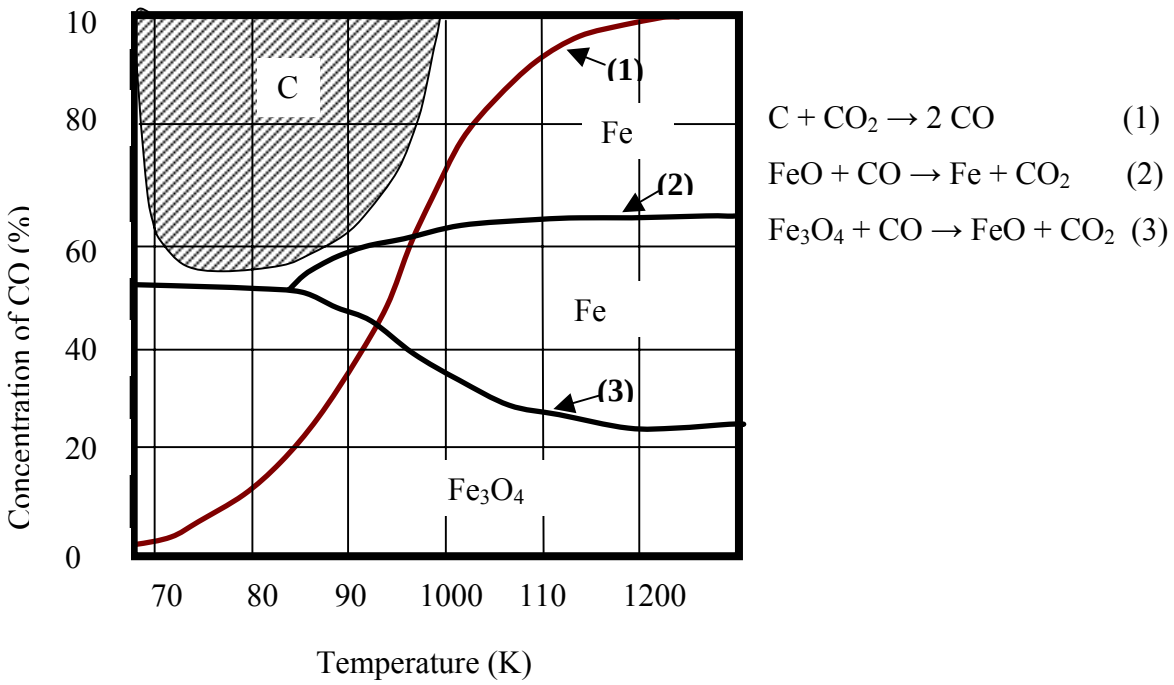

Figure 12: Gibbs Free Energy vs. Temperature

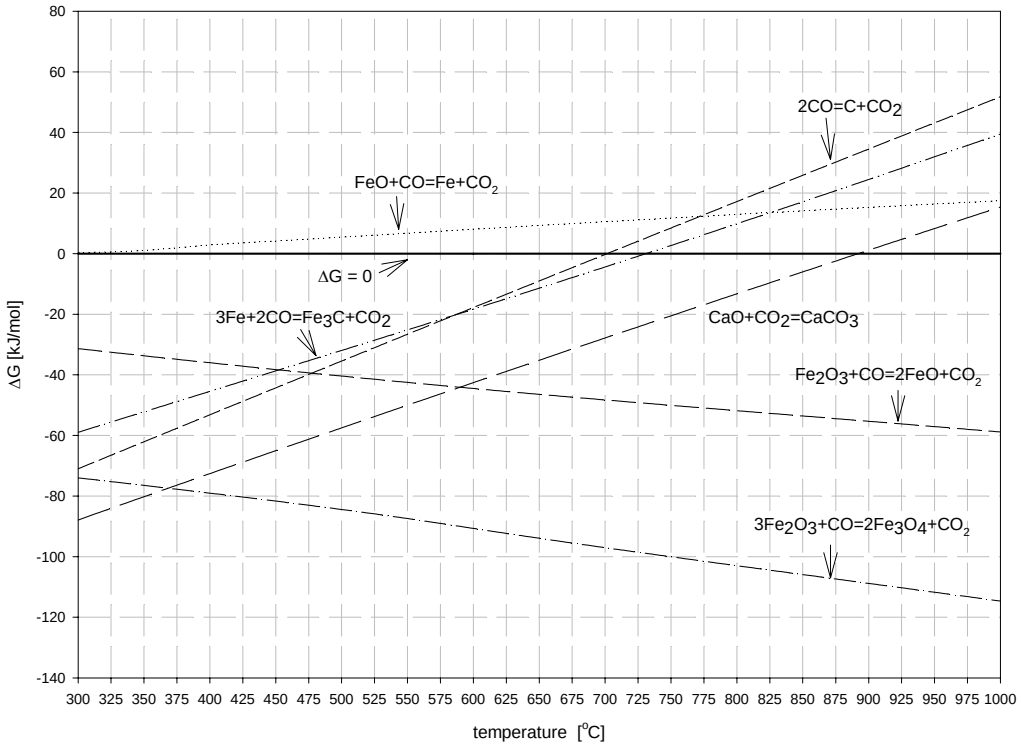

Figure 13: Gibbs Free Energy vs. Temperature.

4.1.2 Kinetic Model for Reduction of Iron Oxide using Carbon Monoxide

The reduction of ferric oxide by carbon monoxide is assumed to take place via a series pathway in which the products of the reactions are FeO, Fe and Fe_3C. In addition, the Boudouard reaction is involved to explain the formation of carbon and production of carbon dioxide. Evidence of Fe_3C was found by x-ray diffraction analysis of the products of the reaction. Several researchers [9,10,11,24] have identified various iron carbides being formed in such reducing atmospheres and the presence of carbon. The following chemical reactions are proposed.

$$Fe_2O_3(A) + 2CO \xrightarrow{k_1} 2FeO(B) + 2CO_2$$

$$FeO(B) + CO \xrightarrow{k_2} Fe(C) + CO_2$$

$$3Fe(C) + 2CO \xrightarrow{k_3} Fe_3C(D) + CO_2$$

$$2CO \xrightarrow[Fe]{k_4} C(D_1) \quad + \quad CO_2$$

The above reactions can be represented by a series irreversible reaction mechanism as shown below:

$$A \xrightarrow{k_1} B \xrightarrow{k_2} C \xrightarrow{k_3} D \qquad (6)$$
$$CO \xrightarrow[Fe]{k_4} D_1$$

The concentration vs. time profiles are analytically derived for the following cases [27]:(i) $k_1 \neq k_2 \neq k_3$; (ii) $k_1 = k_2$; (iii) $k_2 = k_3$; (iv) $k_1 = k_3$; and (v) $k_1 = k_2 = k_3$. It is reasonable to assume that the above mentioned reactions can be represented by pseudo-first order, irreversible chemical rate expressions since the experiments are carried out under the continuous flow of pure carbon monoxide. The following differential equations describe the mass balance of the chemical species involved in Eq. (6) assuming first order irreversible kinetics:

$$\frac{dA}{dt} = -k_1 A \qquad (7)$$

$$\frac{dB}{dt} = 2k_1 A - k_2 B \qquad (8)$$

$$\frac{dC}{dt} = k_2 B - k_3 C \qquad (9)$$

$$\frac{dD}{dt} = \frac{1}{3} k_3 C \qquad (10)$$

$$\frac{dD_1}{dt} = k_4 (C + D) \qquad (11)$$

The overall mass balance (i.e. sum of Eqs. (7) –(11) can be represented as following:

$$2A + B + C + 3D = C_t = 2A_o + B_o + C_o + 3D_o \qquad (12)$$

The solution to Eq. (7) is obtained by separating the variables and using the initial condition: $t = 0$, $A = A_o$:

$$A = A_o e^{-k_1 t} \tag{13}$$

Upon substitution of A from Eq. (13) into Eq. (8) results in the following expression:

$$\frac{dB}{dt} + k_2 B = k_1 A_o e^{-k_1 t}$$

The solution to the above first-order, homogeneous differential equation is given by:

$$B = 2k_1 A_o e^{-\alpha k_1 t} \int e^{(\alpha-1)k_1 t} dt + C_1 e^{-\alpha k_2 t} \tag{14}$$

where,

$$\alpha = k_2 / k_1 \tag{15}$$

and, C_1 is the constant of integration which is evaluated using the initial condition: $t = 0$, $B = B_0$. Similarly the solution to the differential equation (9) is given by:

$$C = \alpha k_1 e^{-\beta k_1 t} \int B e^{-\beta k_1 t} dt + C_2 e^{-\beta k_1 t} \tag{16}$$

where,

$$\beta = k_3 / k_1 \tag{17}$$

and, C_2 is the constant of integration which is evaluated using the initial condition: $t = 0$; $C = C_0$. Closed form solutions for B and C are reported in literature for the case when $k_1 \neq k_2 \neq k_3$, i.e. $\alpha \neq \beta \neq 1$. In Table 4, we have reported the solution for kinetic concentration of species involved for all possible scenarios, namely: (i) $\alpha \neq 1$ and (ii) $\alpha = 1$. For case (i), three possibilities exist: (a)

$\alpha \neq \beta, \beta \neq 1$; (b) $\beta = 1$, and (c) $\alpha = \beta$. For case (ii), the following two possibilities were considered: (a) $\beta \neq 1$ and (b) $\alpha = \beta$. The concentration of species D is obtained from Eq. (12). Finally, the concentration of species D_1 is obtained by integrating Eq. (11). Considering the case I-a (Table 4), we obtain the following expression for D_1.

$$D_1 = (D_1)_0 + \frac{2\alpha\beta_1 A_o}{(\alpha-1)(\beta-1)} \cdot \frac{[\beta-3]}{3} \cdot \left(e^{-k_1 t} - 1\right) + \frac{C_1\beta_1}{(\beta-\alpha)} \cdot \frac{[\beta-3\alpha]}{3\alpha} \cdot \left(e^{-\alpha k_1 t} - 1\right) + \frac{2\beta_1}{3\beta} C_2 \left(e^{-k_1 t} - 1\right) + \beta_1 k_1 (C_2)_1 t \quad (18)$$

where,

$$\beta_1 = k_4 / k_1$$

and,

$$(C_2)_1 = D_0 + \frac{2A_0}{3} + \frac{B_0}{3} + \frac{C_0}{3}.$$

The total mass of the solids, W, is given by

$$W = A\,M_A + B\,M_B + C\,M_C + D\,M_D + D_1\,M_{D1} \quad (19)$$

where, M stand for the molecular (or atomic) weight. Substituting D from Eq (12-a) into the above equation we find

$$W = A(M_A - 2/3\,M_D) + B\,(M_B - 1/3\,M_D) + C\,(M_C - 1/3\,M_D) + 1/3\,(2\,A_0 + B_0 + C_0)\,M_D + D_0 M_D + D_1 M_{D1}. \quad (20)$$

Since, A, B, C and D_1 are known as functions of time and from the mass of solids versus time data, the three rate constants can be evaluated.

4.1.3 Results and Discussion (TGA and Kinetic Model)

The size distributions of both the iron oxide samples used are provided in Table 3. The x-ray diffraction pattern of the as-received iron oxide samples and that of the products resulting from the TGA experiment in 100 % CO are provided in Figures 14, 15 (coarse) and 16 (fine) respectively. Figure 17 shows the variation of rate constants with temperature. Table 5 shows the calculated activation energy and frequency factors. Figure 18 shows the x-ray diffraction pattern for the reduced iron oxide samples in 40 and 50 % CO Atmosphere at 850^{o}C. It is seen from these figures that the feed sample contained only α–Fe_2O_3. The fine (powder) and the coarse (particle) samples are observed to have the same phase structure. The x-ray diffraction pattern of the reduced product (Figure 14), when the fine sample was used, showed the presence of Fe_3C, graphite and α – Fe. This validates the inclusion of the formation of iron carbide in our kinetic model.

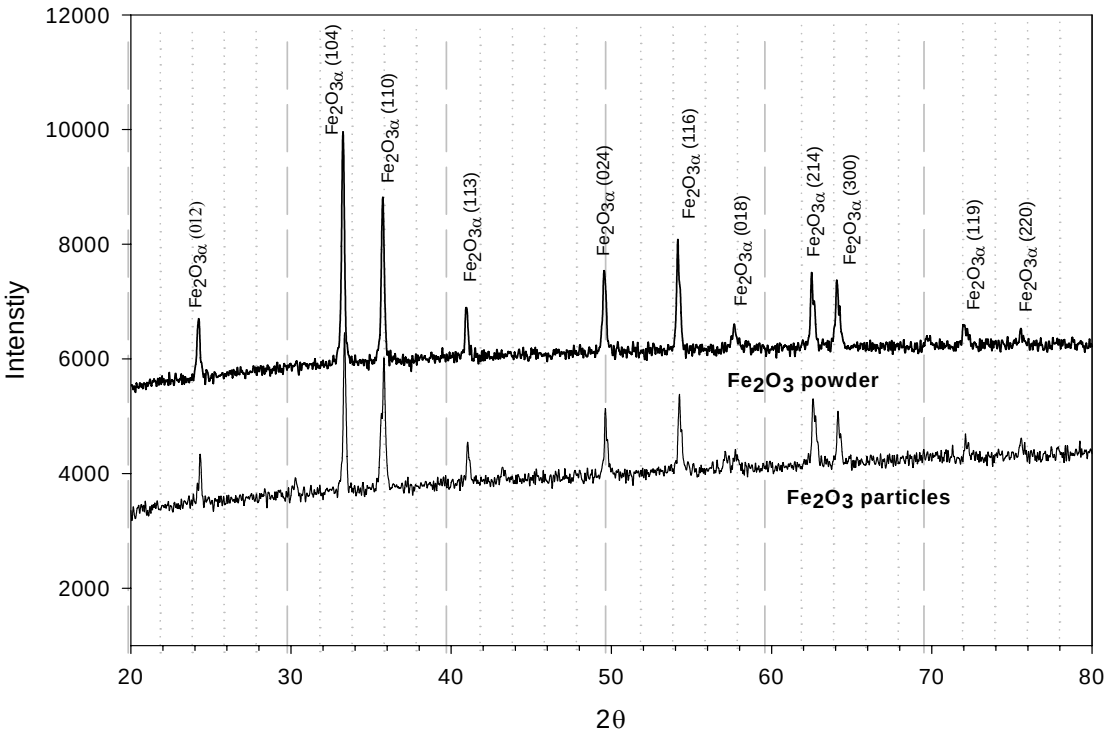

Figure 14: X-ray Diffraction Pattern for the As Received Iron Oxide Samples –Fine (powder) and Coarse (particle).

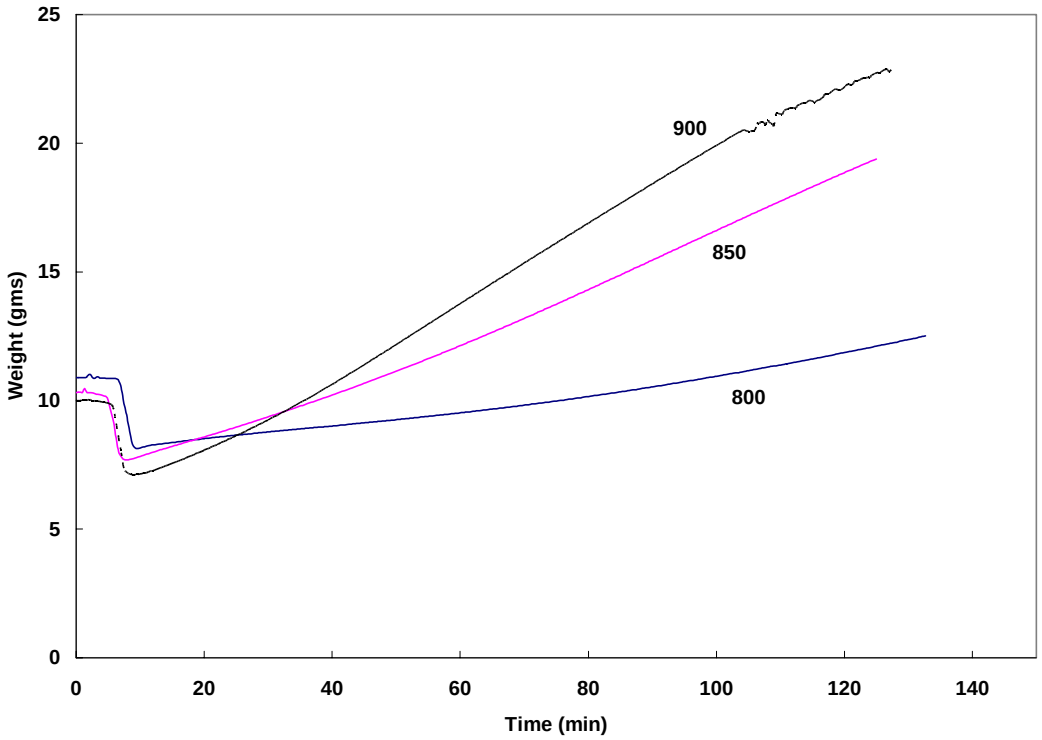

Figure 15: Experimental TGA Curves Obtained Via Reduction of Coarse Iron Oxide Samples in Pure CO at 800, 850 and 900 ^{o}C.

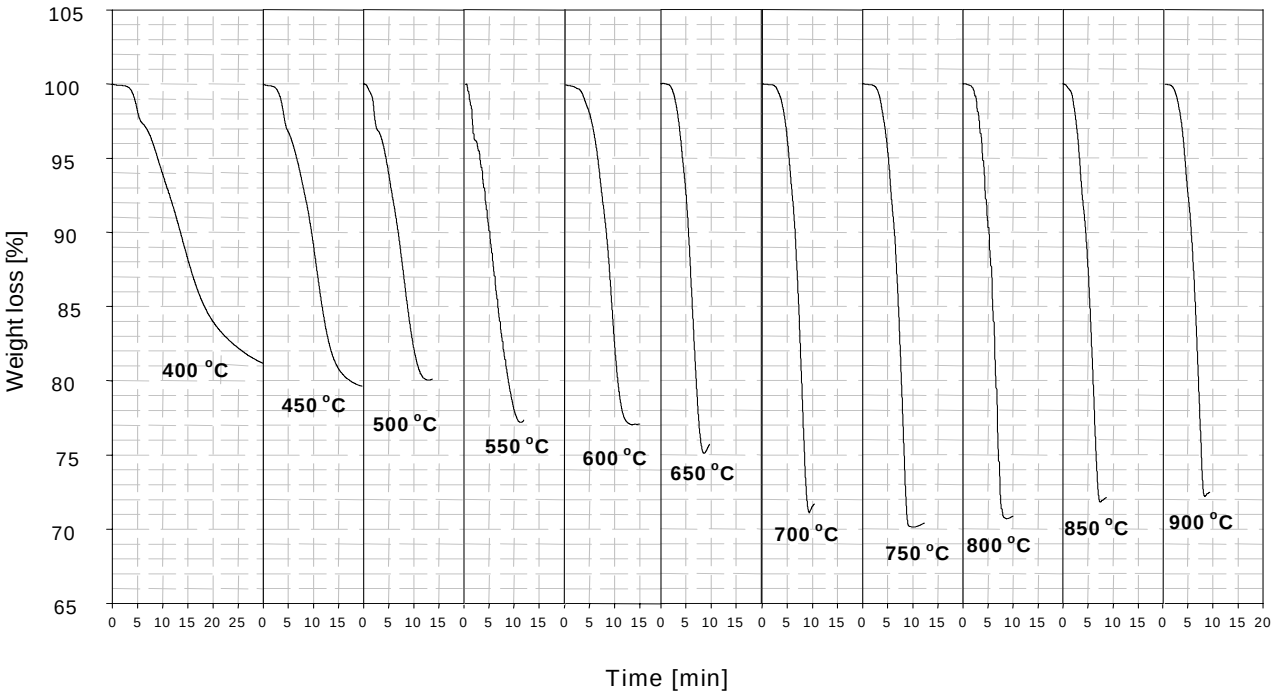

Figure 16: Experimental TGA Curves Obtained Via Reduction of Fine Iron Oxide Sample in Pure CO at Temperatures Ranging from 400°C -900°C.

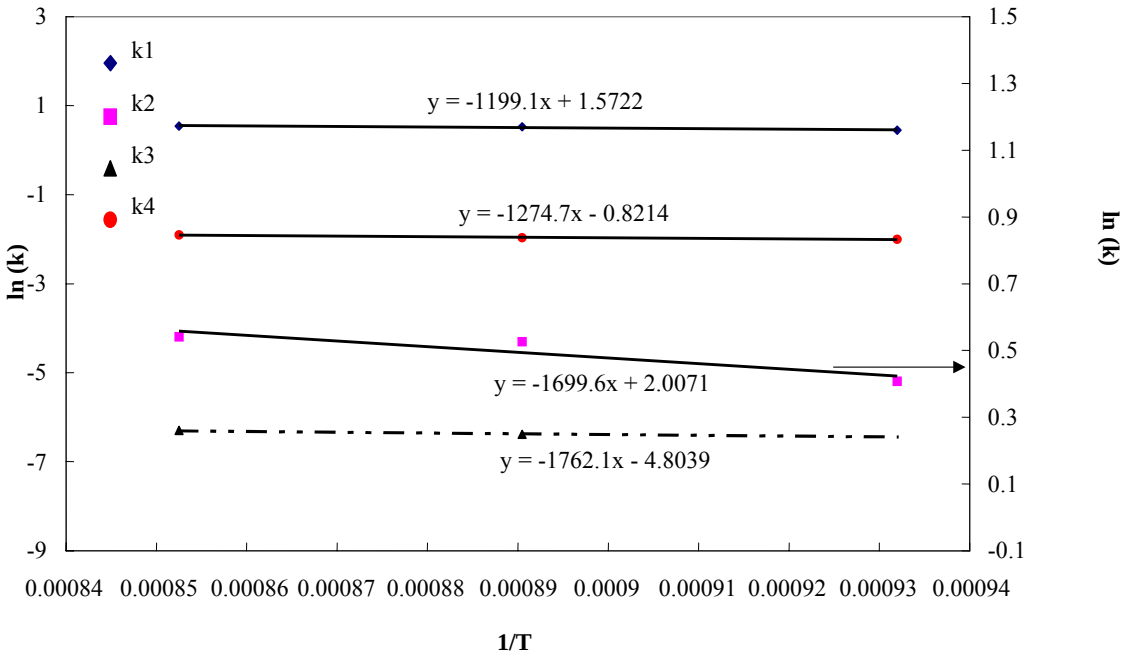

Figure 17: Variation of Rate Constant with Temperature for the Reactions in Iron(III) Oxide Reduction in CO.

	E (kJ mol^{-1})	k_0(min^{-1})
k_1	9.97	4.82
k_2	14.13	7.44
k_3	14.65	0.082
k_4	10.60	0.44

Table 5: Estimated Activation Energies and Frequency Factors for the Various Reactions Involved in Iron Oxide Reduction with 100% CO Gas Stream.

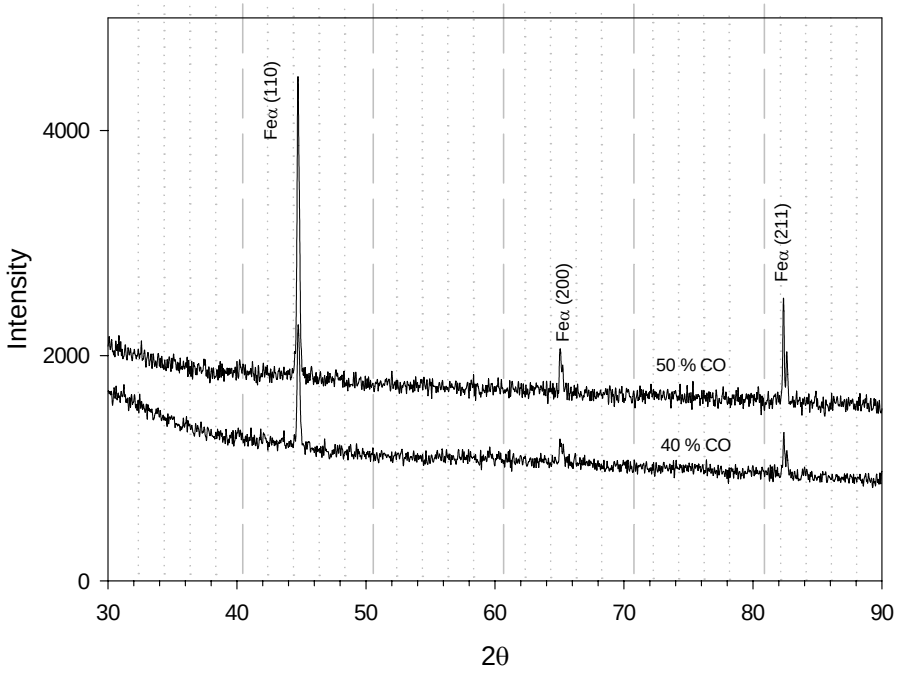

Figure 18: X-ray Diffraction Pattern for the Reduced Iron Oxide Samples in 40 and 50 % CO Atmosphere at 850^{o}C.

4.2 Economic Assessment (Task 2)

An economic feasibility analysis was conducted to estimate the production costs for hydrogen using a coal gasifier integrated with the process. The economic analysis considers the capital, operating and maintenance costs for all the subsystems. It is estimated that the cost of producing hydrogen along with sequestration-ready carbon dioxide is around $1.7 per kg. In comparison, the current cost of producing hydrogen from coal gasifiers without carbon dioxide sequestration is around $1.4 per kg. The difference between the cost of hydrogen with carbon dioxide sequestration (proposed technology) and cost of hydrogen without carbon dioxide sequestration (current market cost) was then used to estimate the cost of carbon dioxide sequestration to be $5.8 per ton of carbon dioxide avoided. Hence, if the cost of sequestering carbon dioxide is less than $9.2 per ton then the U.S. DOE goal of $15 per avoided ton of carbon dioxide could be a reality.

4.3 Cold Flow Modeling (Task 3)

4.3.1 Fluidized Bed Theory

Fluidized bed theory is included in appendix A.

4.3.2 Cold Flow Model Results

Table 6 summarizes data and results from the low gas flow trials. Slugging and channeling were consistent problems. Since the bed depth was the same, or greater than the bed diameter and the particles were very small with a high probability of static cling, these were expected at inlet gas velocities near minimum fluidization. No data was available on the sphericity of particles, so sphericity was estimated from experimental work by Brown et al, as cited by Kunii and Levenspiel [29]. $CaCO_3$ experienced channeling throughout the low flow, as indicated by the low pressure drop across the bed (Figure 19). The experimental minimum fluidization velocity of 0.02452 cm/s was below the theoretical of 0.0294 cm/s, but was within the particle diameter standard deviation of 17.41μm.

The Fe_2O_3 sample experienced slugging at minimum fluidization, shown by the high pressure drop created by the slug that stayed intact at the low gas flow velocities (Figure 20).

The minimum fluidization velocity of 0.0502 cm/s was higher than the calculated 0.0466 cm/s, but was also within the limits of the particle diameter standard deviation of 11.23 μm.

The CaO sample experienced slugging and channeling, as illustrated by the varying bed pressure drop (Figure 21). Minimum measured fluidization velocity was 0.0173 cm/s, which was slightly higher than the theoretical value of 0.0160 cm/s. Diameter standard deviation was 8.72 μm.

Minimum Fluidization Data for Low Flow-Cold Flow Fluidization Study

Solid	Bed Height (cm)	Bed Diameter (cm)	Mass of solid (grams)	Bed Void Fraction	Experimental Pressure Drop (cm H2O)	Theoretical Pressure Drop (cm H2O)	Experimental Fluidization Velocity (cm/s)	Theoretical Fluidization Velocity (cm/s)
Fe2O3	6.42	6.372	479.0	0.55	15.25	15.01	0.0502	0.0466
CaO	7.90	6.372	259.8	0.69	7.9-8.2	9.22	0.0170	0.0160
CaCO3	7.12	6.372	283.0	0.55	8.5	8.87	0.0245	0.0294
Mixture #1 Layered	slug	6.372	284.1	slug	slug	8.9	0.0214 - CaO 0.0444 – Fe2O3	0.0167
Mixture #1 Mixed	7.923	6.372	284.1	0.72	9.0	8.9	0.0245	0.0167
Mixture #2 Layered	5.83	6.372	235.7	0.66	7.66	7.39	0.053	0.063

Table 6: Minimum Fluidization

Hematite and calcium oxide were layered at a 1:2 mass proportion, with the ferrous oxide placed on the bottom. The calcium oxide fluidized as a slug (Pictures in appendix B) above the iron and a deviation in the pressure vs. flow rate can be seen near the minimum fluidization value of 0.0173 cm/s (Figure 22). The hematite fluidized separately, also as a slug, at 0.044 cm/s.

The hematite and calcium oxide were then pre-mixed before being introduced into the glass reactor. Bed pressure drop vs. flow rate is shown in Figure 23. The bed moved as a whole and a slug was formed, which never disintegrated.

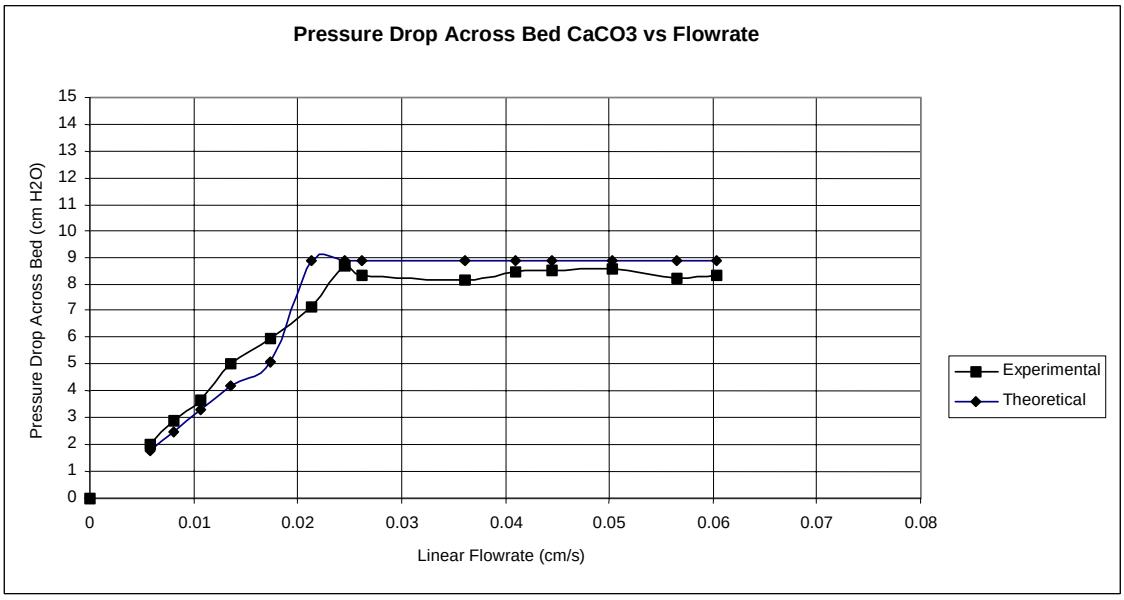

Figure 19: Pressure Drop Across Bed-$CaCO_3$ vs. Flow Rate-Cold Flow Fluidization Study
Figure Pressure Drop vs. Flow Rate

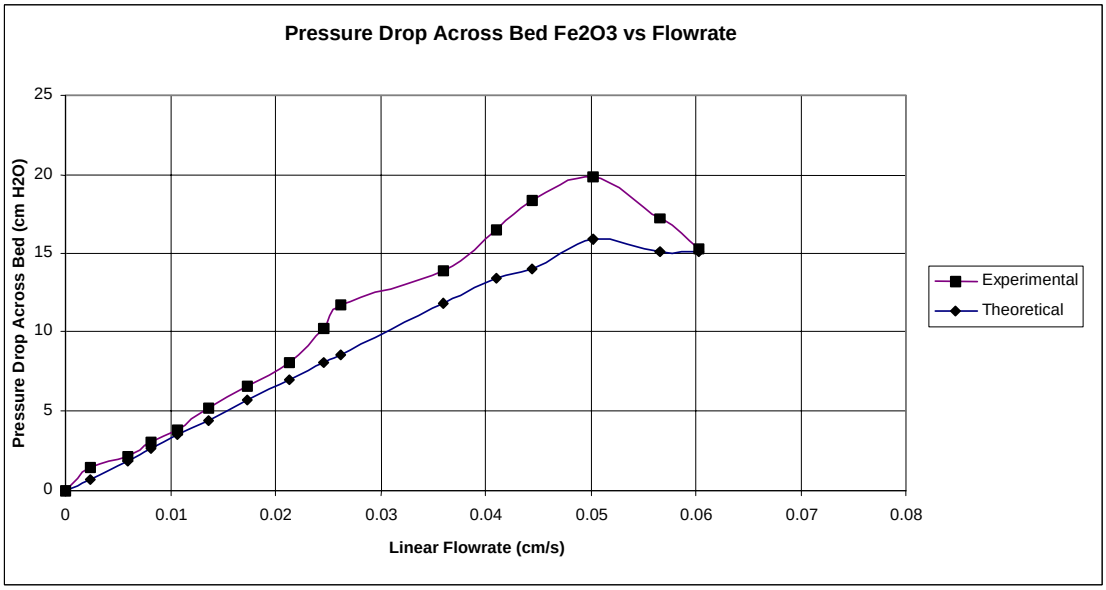

Figure 20: Pressure Drop Across Bed-Fe_2O_3 vs. Flow rate-Cold Flow Fluidization Study

The final low flow test (figure 24) involved layering $CaCO_3$, Fe_2O_3 and CaO, respectively, in a 1:1:1 mass ratio. The bed rose and split, forming a slug at the calcium oxide layer. The bed pressure drop curve shows fluctuations near the experimentally-determined minimum fluidization velocities for each individual particle: Fe_2O_3 – 0.0502 cm/s, CaO – 0.0170 cm/s, and $CaCO_3$ – 0.02452 cm/s. No mixing ever occurred at the low flow rates. Experimental pictures demonstrating the fluidization results are included in appendix B.

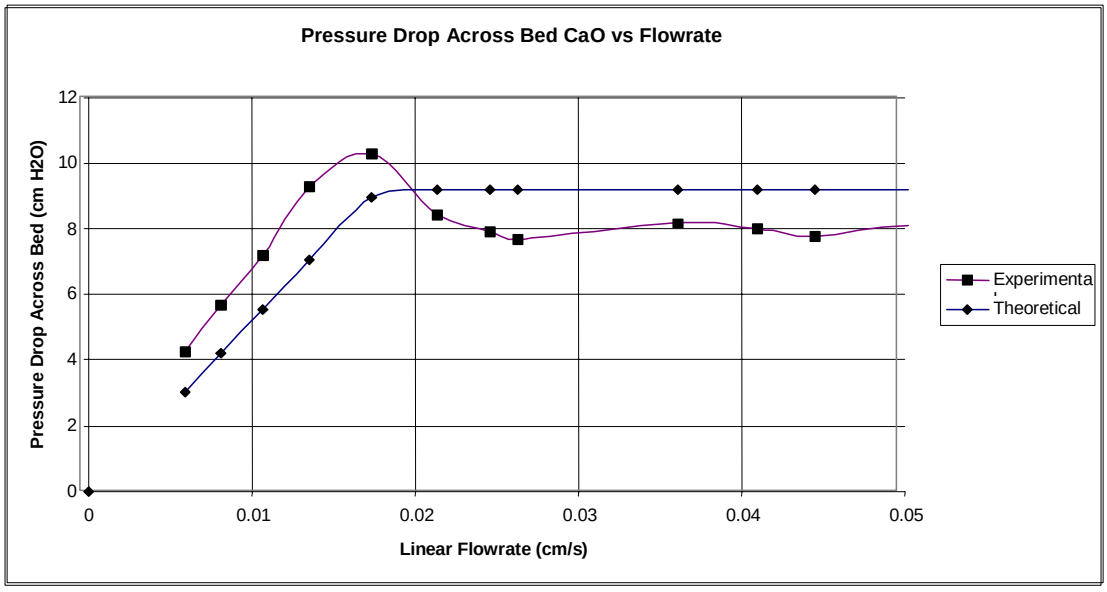

Figure 21: Pressure Drop Across Bed – CaO vs. Flow Rate – Cold Flow Fluidization Study

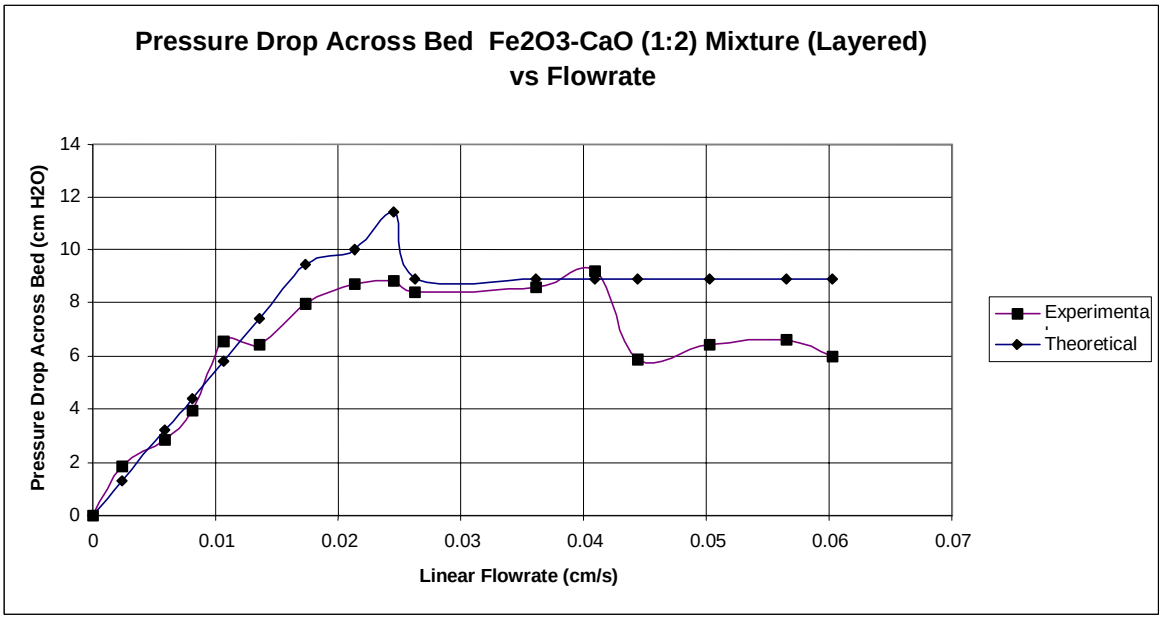

Figure 22: Pressure Drop Across Bed Fe_2O_3:CaO (1:2) Mixture vs. Flow Rate – Cold Flow Fluidization Study

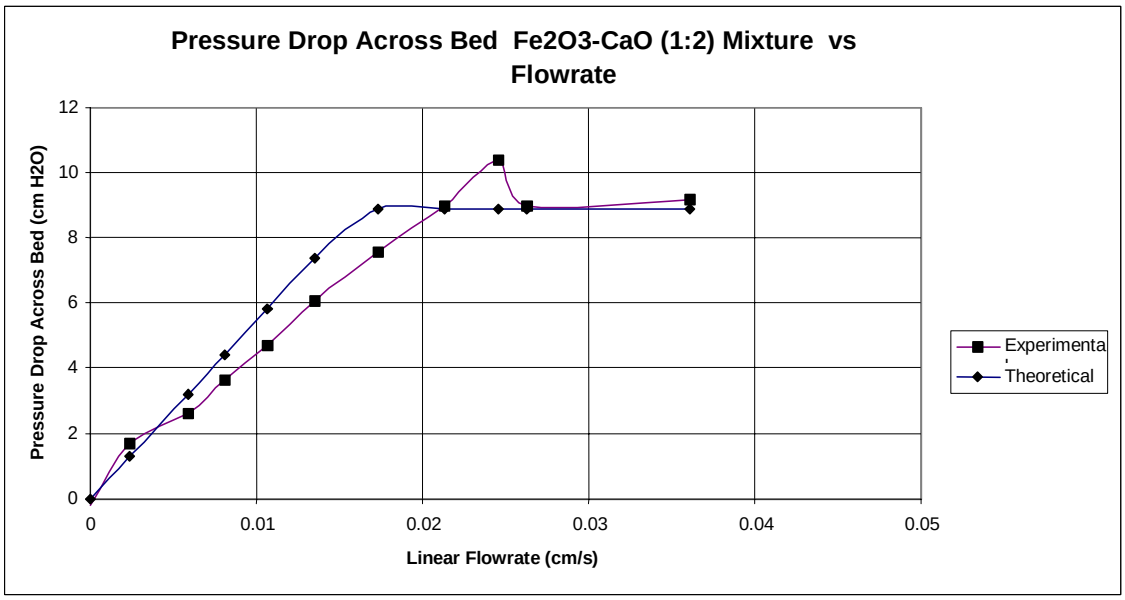

Figure 23: Pressure Drop Across Bed Fe_2O_3:CaO (1:2) Mixture vs. Flow Rate – Cold Flow Fluidization Study

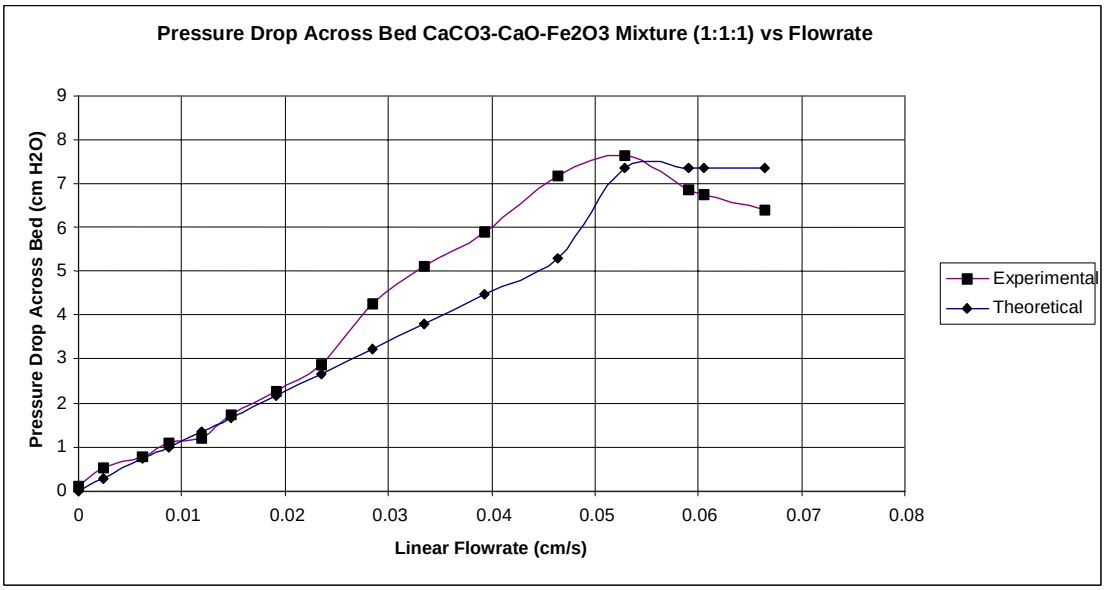

Figure 24: Pressure Drop Across Bed –$CaCO_3$:CaO:Fe_2O_3 Mixture (1:1:1) vs. Flow Rate – Cold Flow Fluidization Study

4.4 High Flow Rate Study (Task 3)

Table 7 summarizes the results of a qualitative study to determine the optimum ratio between operating velocity and minimum fluidization velocity. All references indicated that problems involving channeling and slugging in fluidized beds can often be overcome by operating at gas inlet flowrates several times higher than minimum fluidization velocity. The model by Baeyans & Geldart in Yates [30] failed to predict the slugging that was noted in the low flow study. The critical bed height was calculated as 82.97 cm; with all minimum-slugging velocities greater than 5.5 cm/s. Slugging occurred at or near fluidization.

The ratio between minimum bubbling velocity and minimum fluidization ranged from 4 to 9.7, so the first observations for high flow fluidization were taken at 15 times minimum fluidization gas velocity. The ferric oxide showed good fluidization characteristics, but the calcium compounds channeled. A better quality fluidization was noted for all three compounds at thirty times minimum fluidization, however, the elutriation of iron fines was noted. The calcium compounds reached a good bubbling fluidization at 40 times minimum, however some elutriation of fines was also noted at this value.

Hematite was layered with calcium oxide at a one to two mass ratio. Unlike the low flow studies, the calcium oxide was placed on the bottom to observe any mixing properties. The two compounds did not demonstrate any significant mixing. A mass ratio of 1:1:1 of, respectively, calcium carbonate, ferric oxide and calcium oxide were layered in the reactor. Channeling was never totally overcome, however, mixing was noted at thirty times minimum fluidization. The layers were allowed to mix for several minutes at forty times minimum fluidization velocity, but complete mixing was never achieved.

	Fe_2O3	CaO	CaCO3	Fe_2O_3:CaO 1:2 mixture (layered)	Fe_2O_3:CaO: CaCO3 Mixture (layered)
Minimum Fluidization Velocity-experimental (cm/s)	0.0502	0.0173	0.0245	0.0203	0.039
Terminal Velocity (cm/s)	6.97	1.36	4.715	1.36	1.36
Minimum Bubbling Velocity (cm/s)	0.20	0.12	0.23		
Minimum Slugging Velocity (cm/s)	5.7	5.7	5.7		
Pressure drop across bed-theoretical (in of H_2O)	5.6	3.2	3.5	3.5	2.9
U = 15 x u_{mf} Pressure drop across bed-measured (inched of water) / Visual Observation	5.9/ Bubbling	Slugging, then channeling	2.0/ Channeling	18/ Slugging	2.0/ Channeling
U = 30 x u_{mf} Pressure drop across bed-measured (inched of water) / Visual Observation	6.3/ Attrition	3.04/ Bubbling	5.9/ No Channeling, no bubbling	26/ Little mixing	1.0/ Channeling/ little mixing
U = 40 x u_{mf} Pressure drop across bed-measured (inched of water) / Visual Observation	NA	3.9/ Bubbling	4.5/ Bubbling, some attrition	40/ Little mixing/ attrition	1.5/ Channeling/ mixing

Table 7: High Flow Data Summary-Cold Flow Fluidization Study

4.4.1 Reactions Involving Lime and Limestone

Calcinations of limestone at atmospheric pressure and ambient gas transport follows the fundamental dissociation reaction: (Kunii [50])

$$CaCO_3 \xrightarrow{1000^{\circ}C} CaO + CO_2 \tag{38}$$

The dissociation occurs from the outside surface inward, usually along uniform, concentric areas between the $CaCO_3$ and the newly formed CaO. Figure 25 illustrates the influence of carbon dioxide concentration and pressure on the dissociation temperature of $CaCO_3$.

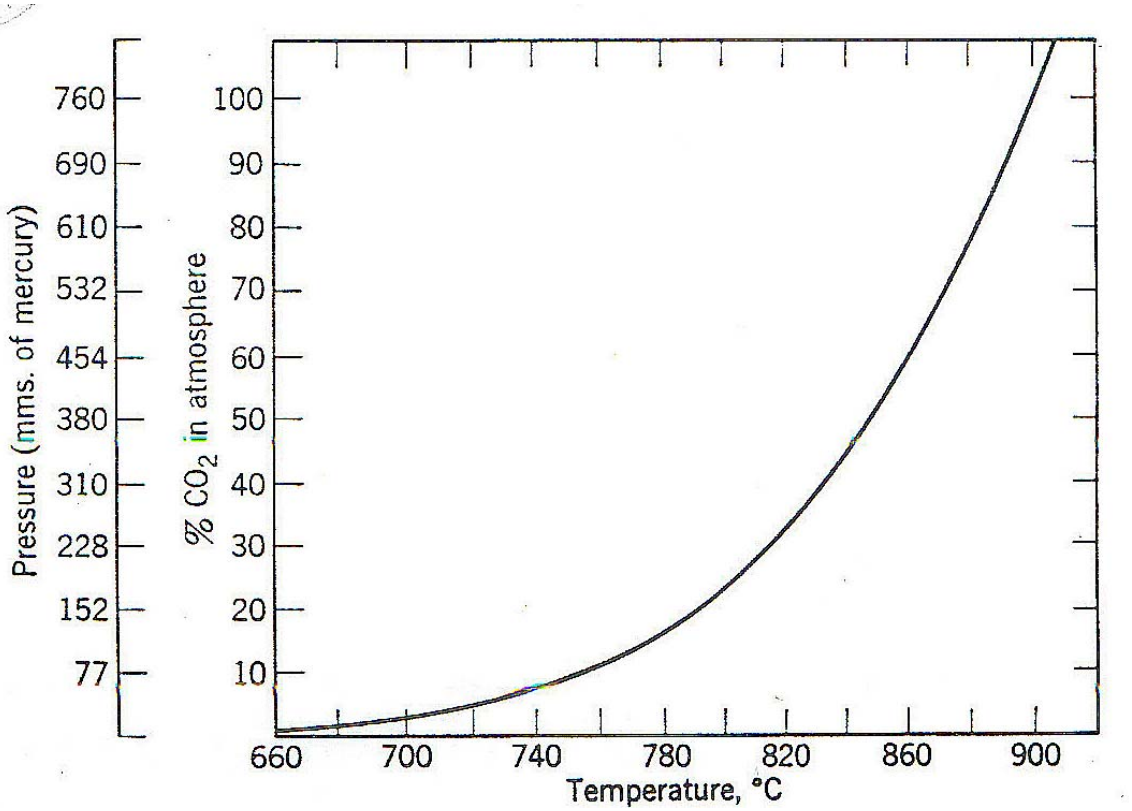

Figure 25: Influence of CO_2 Concentration and Pressure on Dissociation Temperature of $CaCO_3$ (Boynton [34])

This process is highly endothermic, requiring large amounts of outside fuel. Because of the simplicity of the process, the kinetics, mass transfer and heat transfer analysis have found to vary slightly from theory. Although various rate-controlling factors have been associated with results from studies of calcination, a review of the conclusions indicate that the controlling mechanisms vary with the reaction conditions, and follow the expected patterns of

decomposition, diffusion and heat and mass transfer associated with those conditions. Turkdogan in Sohn [31]

Satterfield and Feakes (Borgwardt [32]) found that heat transfer was the major controlling rate factor in the dissociation of 2 cm diameter cylinders of limestone under 100% CO_2, although some effect on chemical reaction was noted. Hills [33] calcined 1 cm diameter spheres in air and air/carbon dioxide mixtures and found the process to be controlled by both heat transfer and the mass transfer of carbon dioxide through the CaO layer. The porosity and thickness of the CaO was found to be the determining factor in any give application.

Borgwardt [32] determined that the rate of reaction was proportional to the initial surface area for particle sizes from 1-90 microns. His experimental activation energy was found to be between 48 and 49 Kcal/mol, with a rate constant between 1.2 and 1.5 x 10^6 mol/cm²·s (at 850°C), when minimizing the effect of CO_2 concentration in the transport gas.

Ingraham and Marier (Borgwardt [32]) determined that the decomposition rate at any given temperature was proportional to the difference between the equilibrium and ambient partial pressures of carbon dioxide. Powell and Searcy (Borgwardt [32]) calcined $CaCO_3$ crystals in a vacuum to rule out vapor phase mass transport as the determining rate factor, and found that the chemical reaction can have a significant impact on the rate and supported this with an activation energy of 50 +/- 3 kcal/mol and reaction rate of 1.1x10^6 mol/cm²·s (at 850°C)These results agree with Turkdogan (Sohn [31]), who found that the chemical reaction rate can decrease the temperature gradient, causing a rate decrease of up to 10%.

The defining relationship between the increase in the dissociation temperature of calcium carbonate and the partial pressure of CO_2 in the decomposing atmosphere was determined by Johnston and Mitchell (Boynton [34]) and has been supported by many studies over the years.

The activation energy at high temperature calcinations can be affected by sintering. Fuller and Yoos [35] found a higher activation energy for limestone samples that tended to sinter when compared to those that didn't under the same circumstances. They also determined that the activation process could be adequately described by first-order kinetics, with little excess activation energy when studied between the temperatures of 450°C to 500°C. They found the shrinking core model to adequately describe the process and that the sintering promoted by impurities tended to introduce a second-order loss term.

Fenouil [36-38] calcined limestone to study the reaction between CaO and H_2S for sulfur removal and found the calcination process to be complete in approximately 15 minutes at temperatures of 890°C-900°C and 1 bar of CO_2 for limestone particles with an original diameter of approximately 1 mm. The reaction time increased significantly with a decrease in temperature: 2 hours for total conversion at 860°C-865°C. The rate doubled in time at temperatures of 930°C to 950°C when the partial pressure of CO_2 decreased from 1 to 0.88 bar.

Turkdogan (Sohn [31]) noted that the temperature and time of calcination affect the porosity of the calcined lime layer, both decreasing the porosity. This may have the effect of creating a pressure buildup of CO_2 inside the limestone particles.

The calcination process is essentially a reversible one, and since the process is dependent upon the partial pressure of CO_2, increasing the pressure in a reactor will affect the equilibrium conditions of $CaCO_3$ and CaO. Berutro [39] made a detailed study of the thermodynamics and kinetics of carbon dioxide chemisorption on calcium oxide, which was expected to give similar results to the bulk reaction of CO_2 with CaO to form $CaCO_3$. Single crystals of very pure calcite were used with dimensions of approximately 3.8 mm x 4.5 cc x 0.8 mm. These samples were sintered over 900K and under an atmosphere of CO_2 to provide surface areas of 19 m^2/g and 12.5m^2/g. The first surface area decreased to approximately 15 m^2/g, but the second set of samples showed little change during the process. Adsorption rates were measured at 983K-1033K and 1333 Pa.

The transfer of CO_2 into the crystals proceeded very slowly, with 4-6 hrs required before weight change had reached the sensitivity of the TGA. The rate increased with temperature and with partial pressure of CO_2. The apparent enthalpy of activation of the adsorption of the carbon dioxide onto surface molecules was determined to be –61 +/- 10 KJ/mol, with the slower absorption of CO_2 into the sample rated at –303 +/- 15 KJ/mol. Adsorption enthalpy was found to be –199 +/- 2KJ/mol for reactions on 55-80% of the surfaces, compared to the standard of –181 KJ/mol.

Borgwardt [40] determined that the combined effects of H_2O and CO_2 on the sintering of CaO at a given temperature were greater than the summative effect of each gas alone, and surface area loss was more strongly affected than porosity. It was determined that grain boundary and surface diffusion mechanisms were responsible.

Silaban & Harrison [41] studied the calcination-carbonation cycling reactions using a high-pressure TGA at temperatures between 750-900°C for calcinations and 550-750°C for carbonation. Pressure varied from 1-15 atmospheres and CO_2 concentration ranged from 0-20% of the inlet gas. Total calcination was attained under the varying conditions, with particle surface area and pore volume returning to near-original sample values. It was determined that production of CaO with the optimum capacity and reactivity for the carbonation cycle was produced under the mildest conditions. Increasing the CO_2 concentration, with an increase in temperature and pressure, multiplied the decrease in reactivity and capacity of the product, due to the increased time necessary to complete the reaction and the fact that CO_2 enhances sintering of the CaO.

The recarbonation process established a consistent pattern of rapid initial weight gain, followed by a very slow rate, indicating possible pore closure and/or sintering on the outer surface. This is consistent with a shift from the rate-controlling outer surface chemical reaction to that controlled by solid-state diffusion through a non-porous $CaCO_3$ layer. The rate of carbonation was strongly controlled by the mole fraction of CO_2 in the feed gas, however, the capacity showed no relationship to the carbon dioxide concentration. The capacity of the calcium carbonate product increased with increasing temperature, consistent with solid-state diffusion, and decreased with pressure when CO_2 partial pressure was held constant. Duration tests found a decrease in carbonation capacity of 46% after 5 cycles.

4.4.2 Reactions with Iron

Hematite reduces to iron in an atmosphere of carbon monoxide (or hydrogen) in three steps (Gupta [42])

Hematite-magnetite $$3Fe_2O_3 + CO(H_2) \rightarrow 2Fe_3O_4 + CO_2(H_2O) \quad (39)$$

Magnetite-wustite $$Fe_3O_4 + CO(H_2) \rightarrow 3FeO + CO_2(H_2O) \quad (40)$$

Wustite-iron $$FeO + CO(H_2) \rightarrow Fe + CO_2(H_2O) \quad (41)$$

The reduction process is dependent upon the temperature and the percentage of CO compared to CO_2 in the reduction gas. The magnetite-wustite reaction is considered reversible, but the hematite-magnetite reduction is not, with a heat of reaction given for the exothermic process as 12 kcal/g-atom oxygen at 1000°C. The overall reduction in CO is almost iso-

enthalpic, with a heat of reaction less then 5 kcal/g-atom of oxygen removed (Evans in Sohn [31]).

Magnetite can be reduced directly to iron at temperatures below 570°C. Below this, the nonstoichiometric compound of FeO is unstable. Its composition varies with temperature and atmospheric make-up, as shown in Figure 26. According to Evans (Sohn [31]), the generation of the gaseous reductants is governed by the following reactions:

Water-gas shift $CO + H_2O \leftrightarrow CO_2 + H_2$ (42)

Boudouard reaction $2CO \leftrightarrow C + CO_2$ (43)

Gasification $C + H_2O \leftrightarrow CO + H_2$ (44)

Turkdogen and Vinter [43,44] did a series of exhaustive studies on the reduction of iron and the physical processes responsible for the reactions in the reducing atmospheres of combinations of hydrogen, carbon monoxide, carbon dioxide and water. The experiments were designed to minimize the impact of convective mass transfer on the rate of reduction by operating well above the starvation rate, although Hills [33] argued that mass transfer could still be a significant factor in the process.

Turkdogan [43] could find no single rate equation to describe the reduction of hematite under pure hydrogen, when compared over different temperatures and particle sizes. It was determined that the porosity, and the change in porosity due to temperature, must be significant, and from this determined the three major rate-controlling factors to be:

1. Uniform internal reduction
2. Limited mixed control
3. Gas diffusion in the reduced iron layer

Uniform internal reduction is independent of particle size, prevails at lower temperatures and occurs when the rate is controlled by the reaction of the gas on the pore walls of the solid. This is the suggested rate-controlling factor in the reduction of FeO to Fe and can be represented mathematically as

$$\ln(1 - F) \propto t \tag{45}$$

This appeared physically as rosettes or platelets of elemental iron within the wustite particle.

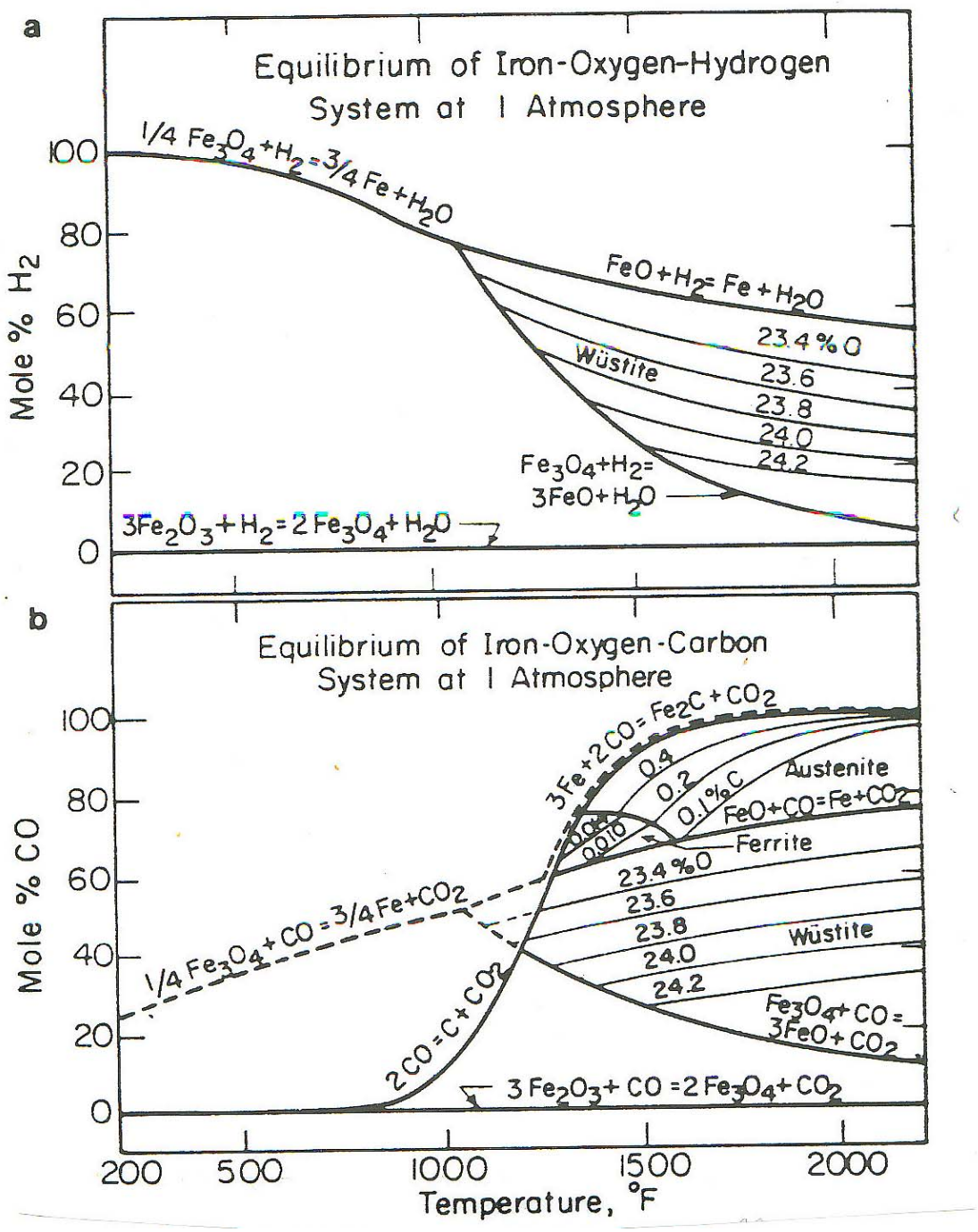

Figure 26: Iron Oxide Equilibrium at Varying Temperatures and Percentages of H_2 and CO (Szekely[45])

Limited mixed control and gas diffusion in the reduced iron layer are both considered types of topochemical reduction, which is a result of a product layer formation on the solid. This most often occurs with large, dense particles at high temperatures. Under these conditions, gas

diffusion is slow and the reaction is limited to the area of the mouth of the pore on the outer surface. Limited mixed control is a type of topochemical reaction that occurs when a thin product layer is formed and provides only a slight hindrance to the diffusion of gas. This allows the rate of reaction to be controlled by both the gas diffusion in the pores of the solid and the reaction on the pore walls. Thiele (Turkdogan [43]) developed a steady-state equation to describe the effect of gas diffusion on the rate of reaction within the pore walls of a catalyst:

$$Rate(mol/s) = 4\pi R^2 c_i \left(\rho_p Sk' D_e\right)^{\frac{1}{2}} x\left[\frac{1}{\tanh(3h)} - \frac{1}{3h}\right] \tag{46}$$

$$\text{where } h = \frac{R}{3}\left(\frac{\rho_p Sk'}{D_e}\right)^{\frac{1}{2}} \tag{47}$$

Assumptions made in the development of the model include Transport of gas by a concentration gradient; uniform and interconnected pores; unchanging surface area.

In his study of the reduction of iron oxide, McKewen (Turkdogan [43]) applied Thiele's model for a set temperature and pressure to develop:

$$\left[1-\left(1-F\right)^{\frac{1}{3}}\right]\alpha\frac{t}{R} \tag{48}$$

The second type of topochemical mode, gas diffusion, controls the rate of reduction when the thickness of the less porous product layer increases to approximately 1 to 2 mm. A model by Spitzer,et al. and by Seth & Ross (Turkdogan [43]), describes the rate of reduction of a spherical solid in a gas under control by gas diffusion as:

$$\left[\frac{1}{2} - \frac{F}{3} - \frac{\left(1-F\right)^{\frac{2}{3}}}{2}\right]\alpha\frac{t}{R^2} \tag{49}$$

In general, gas diffusion controls the rate in large particles, at high temperatures and after approximately 50% reduction significantly increases the product layer and the rate of reduction is proportional to the square of the particle radius.

Physical results from Turkdogan [43] using a scanning microscope, porosity measurements and reduction rates from thermogravimetric analysis supported the theory or reaction-rate control by these three modes.

Turkdogan [44] studied the reduction of hematite particles ranging in size from 0.4 mm to 3.6 mm in various combinations of H_2-H_2O-CO-CO_2 atmospheres. Gas flow rate was 3 liter (STP)/ minute. The times for 60% reduction of 400 μm particles of Fe_2O_3 in a CO/CO_2 gaseous reduction ratio of 9/1, ranged from approximately 10 minutes at 800°C to around 2 minutes at 1200 °C. The rate of reduction was linear at 1000°C for different particle sizes less than 7 mm in diameter. Above that, the relationship followed the inverse square law, which was consistent with rate-controlling mechanisms noted in a pure hydrogen atmosphere. Increasing the hydrogen in the CO/CO_2 gas mixture increased the rate of reduction at 1100°C to 800 μm diameter particles from about 3.8 minutes for 60% reduction using 0% hydrogen, to approximately 0.1 minutes using 100% hydrogen. A 60% hydrogen mixture had a reduction rate of around 1.25 minutes for 60% reduction.

The reduced iron contained carbon deposition when a mixture of CO/CO_2 gas was used. At 80% H_2-20% (CO/CO_2=1/9), an 800 μm diameter hematite particle reduced to 80% oxygen. At 800°C the particles experienced a carbon deposition of almost 0.8% in weight. Carbon deposition with hematite and some gas mixtures only occurred neat the completion of reduction (95% oxygen removal).

The pore area of wustite reduced from hematite ore decreased with increasing reduction temperature and with increasing CO/CO_2 concentrations in the reducing gas. At 800°C, wustite formed under an H_2/H_2O reducing gas had an internal pore surface area of around 6m²/g, but less than 2 m²/g when reduced under CO/CO_2. This decreased to approximately 7 and 3 m²/g, respectively, at 1000°C.

Szekely [45] reduced large hematite pellets (28 mm in diameter and 60% porosity) under different combinations of CO-H_2 reducing gases to study the reduction rates relating only to gas diffusion. The results were a more porous iron product when carbon monoxide was used compared to the resulting product with hydrogen. As found in Turkdogan [43,44] the reaction

rate was markedly faster using hydrogen. The time for 60% reduction using pure hydrogen was less than five minutes, but increased to just under 16 minutes using pure carbon monoxide.

In a TGA study of the decomposition of hematite by pure CO, Ray [46] implied that the rate controlling mechanism might change with temperature, due to varying TGA curves. The Boudouard reaction was significant at temperatures just under 600°C. At lower heating rates (20C°/ min and 30C°/min) carbon deposition did not occur until over 30% reduction.

Sohn [31] noted that iron oxides tend to swell during the reduction process, with some samples showing around a 40% increase in volume. Referred to as catastrophic swelling, it seemed to be caused by the formation of iron needles throughout the oxide pellet, rather than iron grains.

Pressure appears to have an affect on the rate of reduction according to studies cited in Sohn [31]. Pressure proportionally increased the reduction rate of iron up to one atmosphere, but the relationship decreased until around 10 atmospheres, above which little relationship was observed.

Doherty [47] studied the reduction of hematite to wustite in a fluidized bed. Particles were used ranging in diameter from 180-250 μm with reducing gases composed of CO, CO_2, H_2O and H_2. Gas flows ranged from 6-13 moles/hr, which corresponded to 7-15 times the minimum fluidization velocity. No significant carbon deposition was observed on the resulting wustite, and reduction rates increased with an increase in temperature, flow rate, reducing potential of the reducing gas and hydrogen content of the reducing gas. With a reduction by the carbon monoxide-carbon dioxide mixture at 700°C, the study found a rate constant of 1.3×10^{-5} mol/atm·m²·s for a reduction of 12%.

Using the hydrogen-water mixture, a rate constant of 5×10^{-5} mol/atm·m²·s was determined for 17% reduction. The time for 25% reduction increased approximately 60% when a mixture of $CO\text{-}CO_2\text{-}H_2O\text{-}H_2$ was used as a reducing gas, as opposed to using only $CO\text{-}CO_2$. The $CO\text{-}CO_2\text{-}H_2O\text{-}H_2$ mixture reduction time was not significantly different from the reduction time using $H_2O\text{-}H_2$. Monitoring outlet gas composition, it was shown that carbon monoxide utilization increased while hydrogen use decreased, indicating a significant water-gas shift.

The hematite-magnetite reduction was mostly topochemical, and the magnetite-wustite reaction was uniform internal reduction. The expected product layer formation during the magnetite-wustite reaction was not found. Solid-state diffusion was determined to be

insignificant, and the effect of mass transfer in the gas to solid phase was effectively accounted for by use of a two-phase fluidized bed model.

The structural changes during reduction suggested that any porosity increase that occurred through chemical reaction, was destroyed by sintering at temperatures as low at 700°C. Changes in the pore structure were monitored by examining samples from truncated runs. At temperatures up to 700°C, rows of pores approximately 1 μm in diameter were observed that ran along grain lines. In some instances, deep cracks were observed. Above 700°C, slit-like cavities began forming. Surface areas for products formed with the CO/CO_2 combination were much lower than those formed with hydrogen. This could have been due to the longer reduction time for carbon-based gases.

Finally, in a study of the feasibility of the production of hydrogen using a combination of the water-gas shift (WGS) and adsorption of CO_2 by calcined dolomite, Han and Harrison [49] were able to produce high-purity hydrogen by removing between 0.995-0.999 of carbon oxides using various syngas compositions of CO, H_2O, N_2, H_2 and CO_2 at pressures between 5-15 atm and temperatures of 400°C and 550°C. A fixed bed tube reactor was used in the study. In a multi-cycle test to determine the durability of the dolomite, CO_x concentrations did not decrease at either 5 or 11 cycles, although some deterioration of the 149-210 μm sorbent was noted. [50]

4.5 Theory Applied to the Problem (Task 4)

The purpose of this project is to develop a process capable of taking a composition of CO/H_2 gas mixture, representative of that provided by a Vision 21 syngas plant, and converting it into high-purity hydrogen and carbon dioxide, with the lowest thermodynamic penalty. The operation will use ferric oxide as a solid oxygen carrier and calcium oxide as a carbon dioxide absorber in a pressurized, fluidized bed reactor to produce hydrogen. The reactor sorbents will be cycled through a regenerator, utilizing an oxygen and steam gas feed.

In the high-pressure, high-temperature fluidized bed system, syngas composed of 44% CO, 23% steam, and 33% hydrogen, mole ratios similar to a Vision-21 gasifier, were introduced to the reactor, where a portion of the carbon monoxide will be water-gas shifted to produce H_2 and CO_2. The remaining CO should be oxidized by a reaction with ferric oxide, which is reduced to ferrous oxide. The gas stream exiting the reactor then consists of high-purity hydrogen in steam. The ferrous oxide and calcium carbonate are transferred to a regenerator where the iron

compound is oxidized exothermically with an inlet gas composition of 23% steam and 77% O_2. This provides the enthalpy necessary to calcine the lime, releasing carbon dioxide. The gas stream leaving the regenerator will contain carbon dioxide and steam, which is capable of being processed for permanent sequestration or resale.

Thermodynamic properties of the iron and calcium reactions indicate that the reactor process is feasible between the temperatures of 725-900°C, as illustrated by Figure 26 (Loreth [48]). Between these temperatures, the Gibb's Free energy favors the formation of $CaCO_3$ over CaO, and the formation of Fe_3C is suppressed. Based on the theoretical heat of reaction and stoichiometry listed in Table 8, the generation and regeneration cycle is also feasible. The fact that these compounds are relatively inexpensive and readily available, make them attractive to larger scale studies and industrial applications.

Previous studies indicate that an increase in temperature and pressure is expected to increase the rate of reaction for both the decomposition and oxidation of the iron compounds. The Boudouard reaction should not be significant if the operating temperature is over 600°C and the decomposition process is halted before elemental iron. Rate controlling mechanisms should be topochemical and uniform internal reduction. An inlet reactor gas composed of hydrogen and carbon monoxide will further increase the rate of reaction, but will contribute to sintering. These conditions for very fast iron reactions compared to the relatively slow calcium reactions, will determine the mass ratio of sorbents in the system. Sintering under these conditions will determine sorbent life in the cycling process.

Generator Reactions	Heat of Reaction at 25°C (ΔH_r) kcal/mol
$Fe_2O_3 + CO = 2FeO + CO_2$	+0.31
$CO + H_2O = CO_2 + H_2$	-9.5
$CO_2 + CaO = CaCO_3$	-39.9
Regenerator Reactions	
$2FeO + ½\ O_2 = Fe_2O_3$	-67.0
$CaCO_3 = CaO + CO_2$	+39.9

Table 8: Chemical Processes and Heat of Reactions for Reactor and Regenerator

According to the literature review, temperature and CO_2 partial pressure should have the greatest effect on the calcium carbonate-calcium oxide reactions in this study. Low partial pressure of CO_2 will optimize the calcination process, while a high partial pressure will optimize the recarbonation process. High temperatures increase the rate of reaction, but sintering occurs even at temperatures near 700°C, with enhanced sintering occurring in a carbon dioxide atmosphere. This can have an effect on the quality of sorbent in a cycling process. Pressures of 15 atmospheres in the cycling process seem to decrease the capacity of CaO, which will be a determining factor in sorbent life.

Preliminary thermogravimetric studies of the kinetics of the carbonation of the calcium oxide samples (Loreth [48]) indicate a very fast surface reaction, with the rate controlled by chemical reaction, followed by a slower reaction whose rate is controlled by diffusion through a nonporous $CaCO_3$ layer. Only a 33% weight increase was noted over a one-hour period, under a CO_2 atmosphere heated from 50-900°C.

Total carbonation requires a 78.5% weight increase. It is theorized that higher pressures may enhance the gaseous diffusion through the product layer. Initial studies by Loreth [48] of the kinetics, also with a thermogravimetric analyzer, of the reduction of the iron oxide samples indicate a very fast reaction, with reduction to FeO occurring within approximately 10 minutes under a CO atmosphere at 450°C.

The rate of reduction and carbonation, based on time for mass changes in the TGA, indicate a workable mass ratio of 1:7 for Fe_2O_3:CaO. This should allow the hematite to reduce near wustite, while allowing the quicklime to totally carbonate.

Physical properties of the sorbents will limit the lower temperature boundary of the regenerator. Lower temperatures will cause less sintering of the CaO and produce a more favorable limestone for the reactor. Since wustite is unstable below 570°C, 600°C is an acceptable lower limit.

Addition of inexpensive hematite to the production/regeneration cycle should enhance the process by adding an increase in energy through the exothermic oxidation process and by shifting the CO/CO equilibrium ratio of the WGS.

4.6 Dispersion Model Analysis (Task 4)

Because of the inner/outer tube design of the reactor a method to analyze the data needed to be developed. A dispersion model was found to represent the system well. The dispersion model is based on the basic concept of plug flow superimposed with back mixing to produce fluctuations in the flat velocity profile of the fluid through the reactor, and can range in extremes from plug flow to completely mixed flow. Turbulence is introduced to the system through molecular diffusion and back mixing, as measured by the vessel dispersion number:

$$D/uL, \tag{50}$$

where D is the axial dispersion coefficient, u is fluid velocity, and L is the length of the tube.

The dispersion number can be related to the normalized response (C) curve of a step input tracer by measuring the spread of the distribution response curve through its variance. Variance is a measure of the spread of the response distribution about the mean and is determined from the following equation (Levenspiel:

$$\sigma^2 = \frac{\Sigma\left(t^2[CO_x]\Delta t\right)}{\Sigma[CO_x]\Delta t} - \overline{t^2} \tag{51}$$

where σ^2 is variance, [CO_x] is the concentration of carbon oxides, t is time and the mean time of the response curve is found as

$$\bar{t} = \frac{\Sigma(t\Delta t[CO_x])}{\Sigma[CO_x]\Delta t} \tag{52}$$

A large variance is indicated by a wide spread of the response curve when compared to the input curve.

If dispersion is small, the variances of reactors in series is additive. Each reactor adds its own dispersion number, with the end result being the sum of all vessels. This additive property does not account for the order of the reactors, since the addition of variances is commutative, but will give the same results regardless of order of fluid contact.

The reactor designed for this study contains an outer shell, which runs the length of the reactor, and an inner shell containing the fluidized bed. The inlet fluid enters the outer shell, undergoes mixing, along with the water-gas shift and Boudouard, and then enters the inner 1" diameter tube serving as the inlet to the fluidized bed. The large length-to-diameter ratio assures laminar gas flow and flat velocity profiles.

A step input of syngas (33%H_2, 44%CO and 23%H_2O) was introduced to the empty reactor for temperature/pressure combinations of: 725^{o}C/50 psi, 750^{o}C/ 250 psi, 725^{o}C/515 psi and 800^{o}C/ 250 psi,. In appendix D, the output is shown in Figures 38 through 47, odd. Under all conditions, the empty reactor produced a consistent 1:1 ratio of CO/CO_2 in the outlet. This implies that the WGS has adequate time to reach and maintain equilibrium within the reactor for the range of conditions under study. The lag time from initiation of input to initial tracer measurement ranged from 10 to 22 minutes and is dependent on volumetric fluid flow rate and consistency of flow rate. The flow rate was determined by fluidization conditions for anticipated solid/gas properties for hydrogen production.

The variance in each situation is rather large, as measured by the spread of the response curve. Based on the dispersion model, this is used as a measure of deviation from plug flow, and should be caused by the back mixing in both the outer sleeve and the diffuser of the fluidized bed.

As a comparison to the empty reactor, fifty grams of hematite was added to the reactor and experiments were formed under the same pressure and temperature conditions as the empty experiments. Because of different gas input duration for conditions of 725^{o}C/250psi and 800^{o}C/ 250 psi between the empty and hematite-loaded reactor only experimental conditions of 725^{o}C/50 psi, 725^{o}C/515psi and 800^{o}C/250 psi were compared for dispersion analysis. Example outlet gas compositions are shown in figure 27 while more figures are included in the appendix D. The reduction of hematite is exothermic and the rapid increase in temperature pushed the gases through the reactor more quickly, resulting in a shorter retention time.

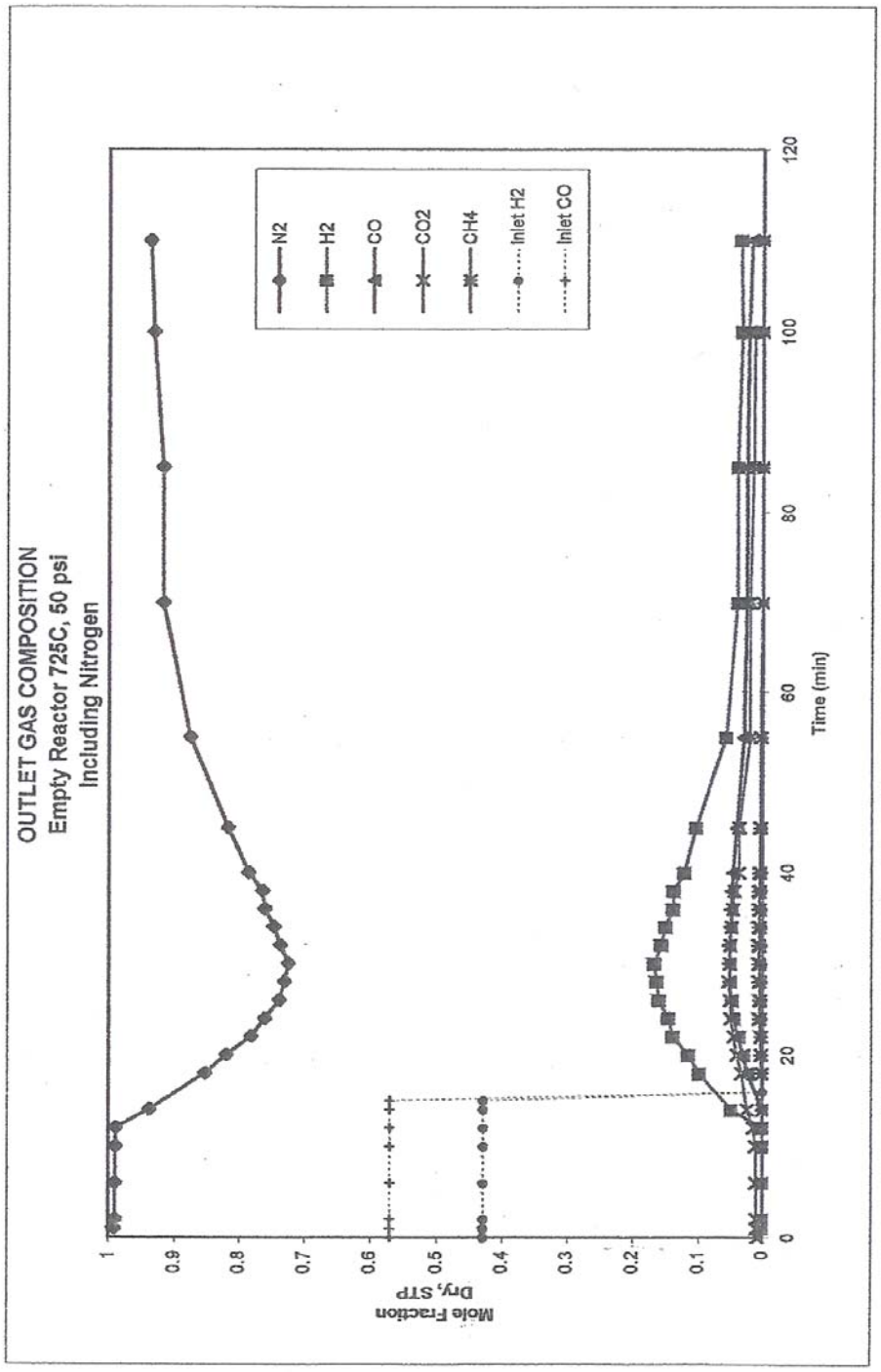

Figure 27: Outlet Gas Composition of Empty Reactor – 725^{o}C, 50psi

The same conditions were then examined with the addition of 50 g of Fe_2O_3 in the fluidized bed. The reduction of hematite is exothermic and produced a large temperature change in the bed. The system is assumed to be under constant pressure and the thermal increase had the effect of increasing the velocity of the output gases and decreasing the initial lag time between input and response measurement, as illustrated by the decrease in mean time of the C-curve. However, the variances of the two conditions, as indicated by the spread of the response curve, varied a from values of 6.25% to 13.9%, less than the 14.14% cumulative instrumentation error of the flow measurement system. C-curve results are shown in Figures 28 through 30.

Addition of the iron compound to the system did not change the general performance of the reactor in terms of the C-curve. An increase in operating pressure increased the holding time of the gas in the reactor. However, an increase in operating pressure increases the spread of the output curves.

Although a fluidized bed is considered to perform as mixed flow, with high dispersion, the small volume of this bed compared to the remainder of the tube reactor made its contribution to the outlet flow variance negligible. The large length to diameter ratio of the inner tube before and after the fluidized bed area guaranteed laminar flow at the inlet and outlet of the inner tube reactor area.

Based on the consistency of variances between the loaded and unloaded reactor and the physical properties of the reactor, the loaded reactor was modeled as a series of two different reactors. The first has a high dispersion, allows the WGS to reach equilibrium, and provides an input stream to the second. The second reactor was assumed to be a perfect plug flow, open end tube reactor, adding no significant dispersion to the gas flow ($\Delta D/uL \rightarrow 0$). The difference between the variances of the response curves was assumed to be solely a result of the exothermic reduction of the iron in the fluidized bed. Variances and mean times are listed in Table 9.

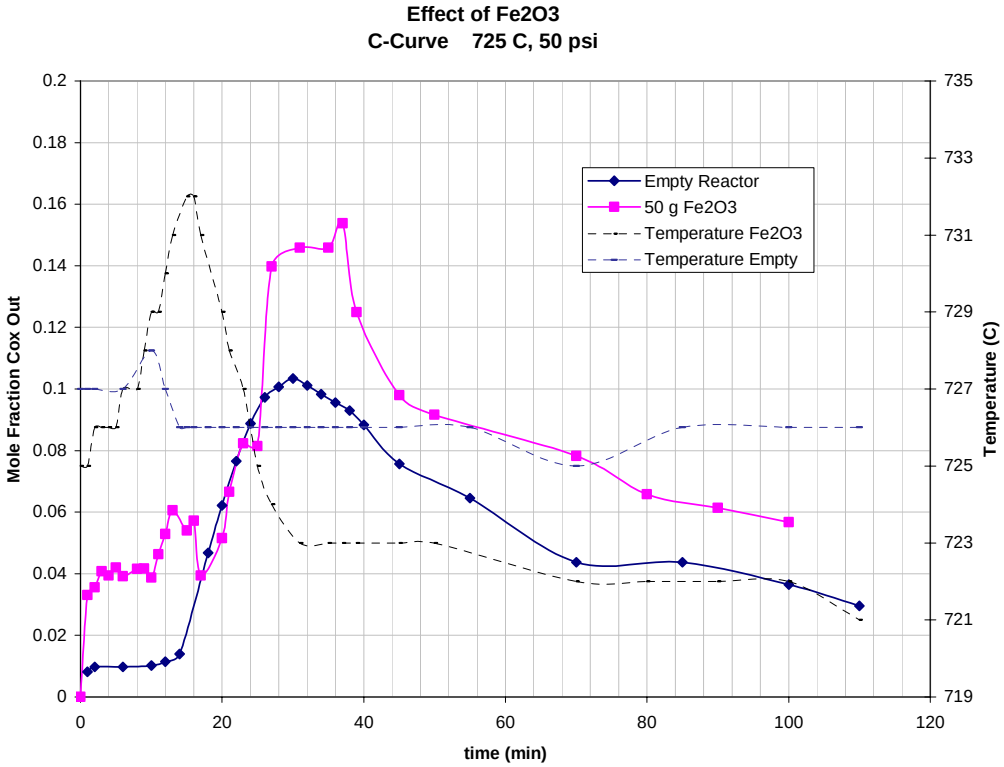

Figure 28: Effect of Fe_2O_3 on Empty Reactor C-Curve – 725°C, 50 psi

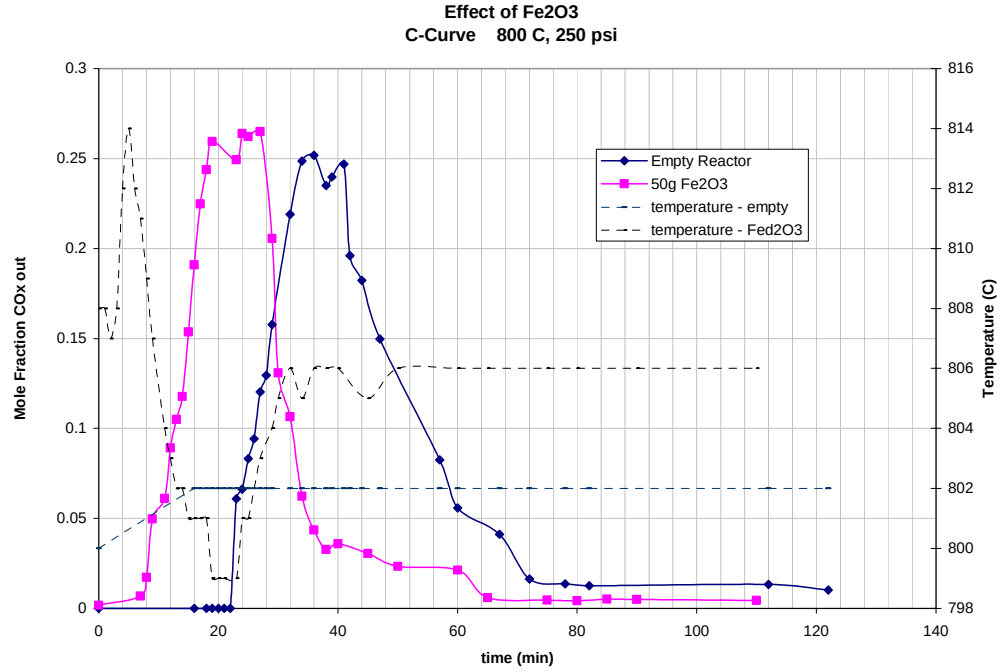

Figure 29: Effect of Fe_2O_3 on Empty Reactor C-Curve – 800°C, 250 psi

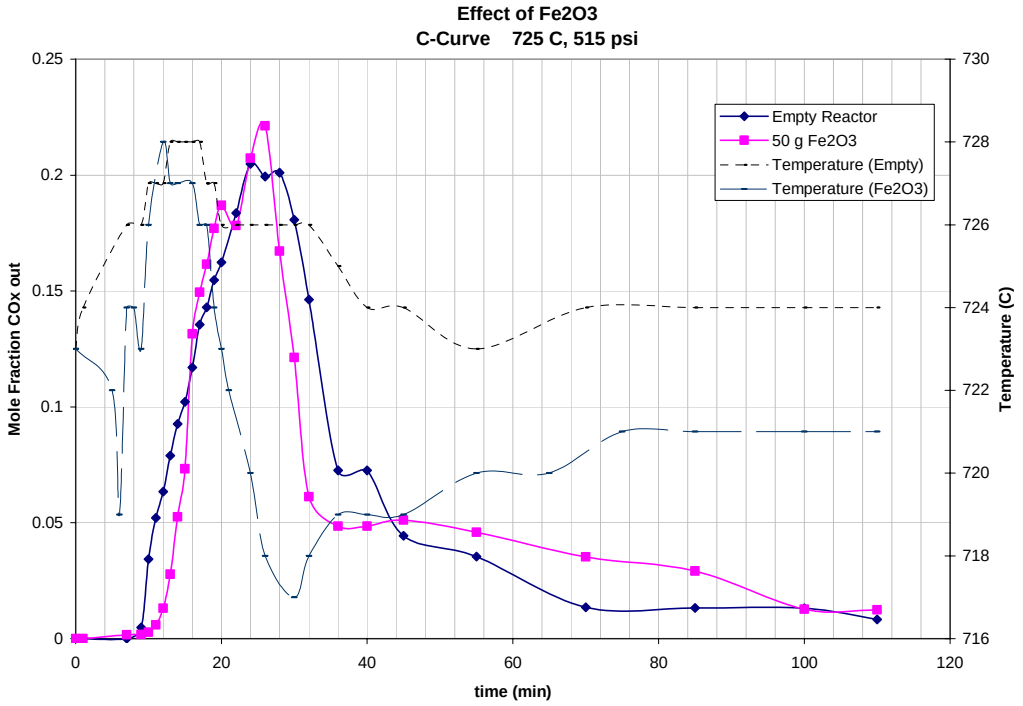

Figure 30: Effect of Fe_2O_3 on Empty Reactor C-Curve – 725°C, 515 psi

Temperature & Pressure	725°C 50 psi		725°C 515 psi		800°C 250 psi	
Solid Load	Empty	Fe_2O_3	Empty	Fe_2O_3	Empty	Fe_2O_3
Median time (min)	55.6	54.1	36	41.8	45.0	30.5
Variance	838	893	548	631	303	325
% Difference in Variance	6.25		13.9		7.00	

Table 9: Effect of 50g Fe_2O_3 on Dispersion Characteristics

4.6.1 Factor Response Experiment

The initial experiments were designed to find conditions for the production of high-purity hydrogen from wet syngas with composition of 44% CO, 33% H_2, and 23% H_2O, using 50 grams of a 1:7 mass ratio of Fe_2O_3:CaO loaded into the fluidized bed reactor. Pressure was varied between 50 psi and 515 psi and temperature between 725°C and 800°C in a response surface study. Flow rate was consistent with 15 times minimum fluidization for the 100 micrometer average diameter of the ferric oxide and 30-40 times minimum fluidization velocity

for the 20 micrometer average diameter of the CaO particles, as determined in the fluidization study. A factor-response table for the study design is shown in Table 10. Outlet gas composition is shown in appendix D.

Factor	Response					
Temperature (C)	Pressure (psi)	Maximum % H_2 (15 min)	Maximum % CO (15 min)	Maximum % CO_2 (15 min)	Maximum % CH_4 (15 min)	Mass of pure H_2 (g)
750	50	97.8	0	0	5.4	0.0705
800	515	94.2	15.2	8.4	18.4	1.27
725	50	98.8	0	0	3.9	0.0894
725	515	60.7	24.7	29.5	35.4	0.671
750	250	92.3	0	0	22.0	0.412
725	250	96.8	0	0	19.9	0.385
800	50	81.7	20.6	20.5	4.1	0.0738
800	250	95.5	7.9	2.8	7.2	0.599

Table 10: Factor-Response for Initial Response Surface Study of Hydrogen Production

Both temperature and pressure, either alone or interacting with each other, were significant in the production of all outlet gases within a 95% probability, as shown in Table 11. The conditions producing the least CO/CO_2 and greatest percentage of H_2 in the outlet were at the lowest pressures and temperatures. This is illustrated by the response surface plots, produced by Design-Expert Software, a product of DesignEase and shown in the appendix E. However, the most significant factor effecting the production of mass of hydrogen was pressure, with the greatest masses produced by the highest pressures, presumably because of the higher standard flow rates.

RESPONSE	SIGNIFICANT FACTORS (95%)	F-VALUE	P-VALUE	SURFACE MODEL	R^2 (FIT)
Percentage of H_2	Temperature-pressure interaction	43	0.022	Quadratic	0.97
Percentage of CO	Temperature-pressure interaction	28	0.033	Quadratic	0.98
Percentage of CO_2	Temperature & Temperature-Pressure interaction	31 79	0.031 0.012	Quadratic	0.99
Percentage of CH_4	Temperature Pressure	7 27	0.046 0.0035	Linear	0.87
Mass of H_2 in 15 Minutes	Temperature	217	0.0001	2FI	1
	Pressure	1709	< 0.0001		
	Temperature-Pressure interaction	169	0.0002		

Table 11: Significant Effects on Production Response

In order to produce larger amounts of hydrogen with an acceptable level of purity, it was necessary to operate at an elevated pressure. Since the purity of hydrogen was uniformly above 95% at 250 psi, with no CO_x, this was chosen as the optimum pressure at which to produce hydrogen for the cycling experiments. Tests were also designed to determine the production capabilities of different temperatures at 250 psi.

One surprising result of the analysis of the outlet gas was the discovery of methane. In the shake down experiments, a significant amount was produced. It was determined that the methane was a result of a reaction with carbon deposited on the reactor walls due to the Bouduard reaction, and catalyzed by the stainless steel of the reactor. It is well known that Bouduard progresses toward the forward reaction near 873 K with small CO concentrations. Although the fluidized bed portion of the reactor was always set at 998 K or above, the reactor

was designed with a significant thermal gradient to allow the use of manufactured graphite gaskets. It was noted that carbon deposition occurred in the outer shell area and in the inlet of the inner INCONEL tube. This also coincided with areas of temperature less than 900 K. No carbon deposition was ever noted at the outlet, probably due to the low carbon dioxide concentrations.

In order to rectify this, a paintable ceramic liner was applied to the outer shell and inlet area of the inner shell. This dramatically decreased methane production, but did not stop it completely, especially at high pressures. This coincides with the statistical analysis of a linear relationship between the effects of temperature and pressure with the production of methane (Figure 31 below. Other response surface curves are included in the appendix E). Carbon was deposited within cracks that developed in the liner, as well as thin liner areas. An increase in temperature decreased the area of the reactor below the optimum temperature of 900 K, thus decreasing methane production. An increase in pressure produced a greater concentration gradient within the walls, which acted as a catalyst for the methane production.

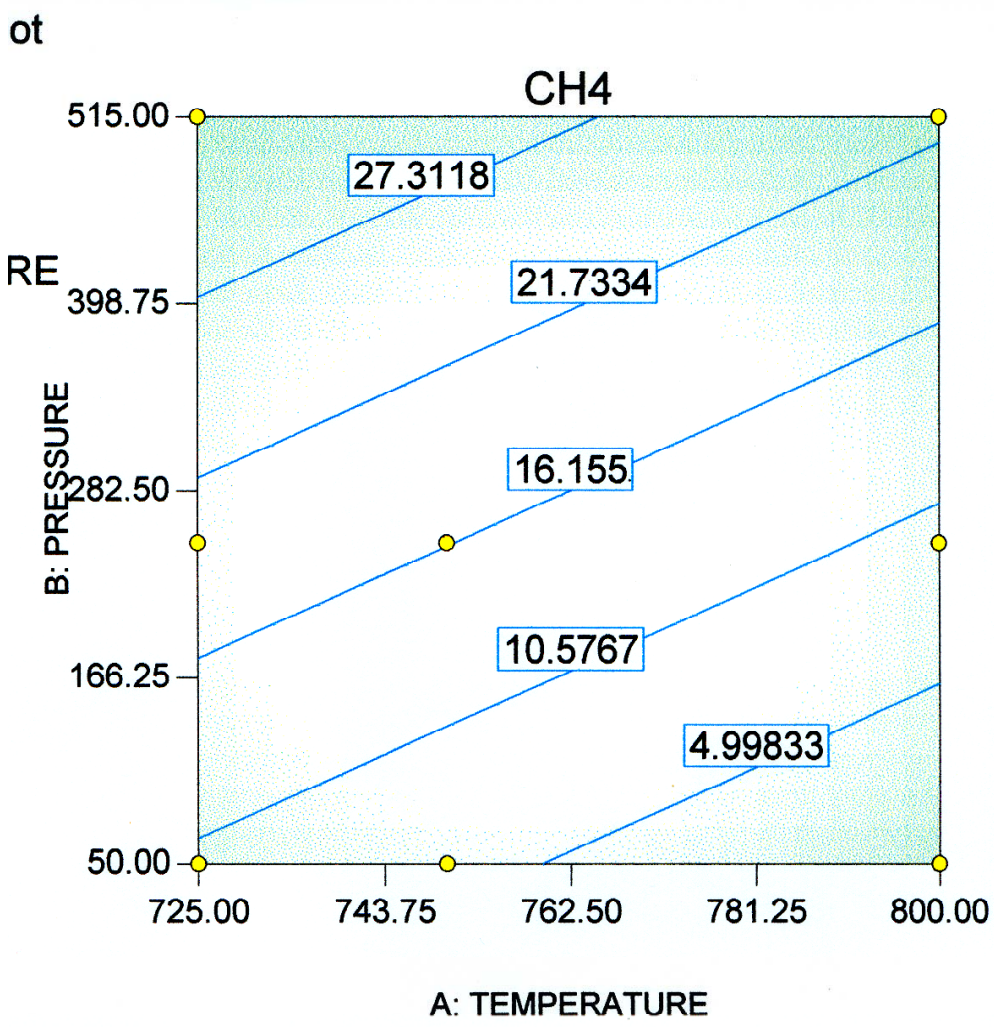

Figure 31: Response Surface Results of Percentage of CH_4 Appearing in Outlet Gas in First Fifteen Minutes

The methane production increased linearly with pressure between 725°C and 800°C, with maximum development at higher pressures. The mass of CO_x in the output gas composition was zero for the minimum fifteen minute testing period at all combinations of 725°C, 750°C and 50psi, 250 psi.

Although high-purity hydrogen (no CO_x) was produced at the above combinations, the greater mass of hydrogen in the output occurred at higher pressures because of the higher flow rates required for fluidization under these conditions. This is confirmed by the statistical finding that the mass of high-purity hydrogen produced during the fifteen minute testing interval increased most significantly with pressure.

In combining the results, the maximum high-purity hydrogen production occurred in the vicinity of 725°C and 250 psi.

4.6.2 Solids Addition to CO_x Conversion Compared to WGS in Empty Reactor

The purpose of the addition of the ferric oxide to the operation of hydrogen production was to decrease the equilibrium ratio of CO/CO_x , increasing the carbon dioxide concentration and shifting the $CaO/CaCO_3$ carbonation/decomposition in favor of carbonation through a non-catalytic gas-solid reaction. In order to determine the effect of the addition of the ferric oxide, 50 grams of hematite were added to the reactor and the outlet gas composition was compared to the outlet gas composition of the empty reactor under the same conditions. The effect of the iron was considered to be additive to the empty reactor. The outlet composition of the empty reactor, excluding nitrogen, is shown in the appendix F.

The effect of the iron was measured as the ratio of CO/CO_x in the outlet with and without 50 grams of hematite, along with the fractional conversion of carbon monoxide at each study condition (appendix G). The loaded reactor was treated as a semi-batch tube reactor with plug flow. Solids were loaded as batch, with inlet flows being pseudo steady state and provided by the empty reactor, as predicted by the reactor-in-series assumption. The pseudo steady state assumption predicted inlet concentrations and flow rates remaining constant within each gas-collection sample period. This allowed a dimensionless time variable to be determined as:

$$\tau = (t - t_r) / \left(n / \bar{v} \right), \tag{53}$$

where $\bar{v}$ is the inlet molar flow rate of CO_x, n is the number of moles of solid, t is the time and t_r is the holding time.

The holding time, or the length of time from introduction of the reducing gases to the sample time of first measurable product, varied with the different fludization flow rates required for the different production conditions. Holding time also varied between the empty and loaded reactor, because of the exothermic nature of the reduction of hematite and its products. This condition causes an increase in velocity of the outlet gases, corresponding to the increase in temperature. In order to compare the outlet compositions from the loaded/unloaded conditions, zero dimensionless time was considered as the first appearance of measurable product. This allowed a standardization of outlets and retained the series reactor assumption.

As a dynamic, non-isothermal, quasi-steady state system, the reactor used to produce the results cannot easily provide specific kinetic or rate-controlling information for any specific reaction under any one set of conditions. However, certain generalizations can be made using the data of fractional conversion of carbon monoxide for the various conditions. The fluidized bed was operated at starvation gas velocities to model the operation of a production facility, making gas film diffusion a significant rate-controlling factor. If this is considered a constant factor, the temperature dependence of the fractional conversion, as illustrated by the strong correlation between the conversion and temperature curves during the non-isothermal processes, indicates that chemical reaction is an important rate-controlling factor at the beginning of the ferric oxide decomposition for all conditions. This would be expected for the small particles used. At 250 psi, the two curves diverged between $\tau = 0.1$ to 0.2, indicating a change in rate-controlling factor – most likely to that of ash layer diffusion control. At 50 psi, the conversion-temperature correlation is not as strong, with a change in rate-controlling factor strongly indicated at $\tau = 0.012$. Gas film diffusion is likely to be more significant at this low pressure than at elevated pressures. At 725^{o}C and 515 psi, the curves converged after $\tau =$ 0.4.

The additive effect of the reduction of hematite on the conversion of CO in this process is summarized in Table 12.

Temperature (^{o}C)	Pressure (psi)	Initial Ratio (CO_{Fe2O3}/CO_{WGS})	Dimensionless Time to Zero Fractional Conversion
725	50	0.14	0.40 (est)
725	250	0.6	0.35
725	515	0.45	0.8
725	250	0.6	0.35
750	250	0.65	0.3
800	250	0.80 (constant)	Not measured

Table 12: Additive Effect on Fractional Conversion of CO to CO_2 by the Reduction of Iron Oxide

Initially, the CO/CO_x ferric oxide-loaded outlet ratio decreased under all conditions when compared to the empty reactor and the results of only the WGS. The highest fractional CO conversions occurred at 725°C in combination with 50 psi and 515 psi. At 250 psi, increasing the temperature decreased the capacity of the solid, as measured by the maximum fractional conversion in combination with dimensionless time to zero conversion. At the target temperature of 725, fractional conversion was approximately 0.40 with dimensionless time to extent of 0.35. At 750°C, this decreased to 0.35 and 0.30. At 800° C, the conversion was only 0.20, although it stayed fairly constant, never reaching zero.

At 725°C, increasing the pressure increased both the conversion of CO and time to zero conversion when comparing 50 psi and 515 psi. However, 250 psi resulted in only a maximum CO conversion of 0.40 and time to zero conversion of 0.35. In summary, the highest conversion rate and maximum capacity of the ferric oxide to decrease the amount of carbon monoxide leaving the reactor due to its reduction occurred at conditions of 725°C and 50 psi.

The mass balance of the experiments used a solid load of 50 g of Fe_2O_3. From stoichiometry, and the step-wise decomposition of hematite to iron, a product of Fe_3O_4 should produce a 1.67g surplus of oxygen; FeO should produce a 5 g surplus; and elemental iron, a 15 g surplus of oxygen. Based loosely on this assumption, conditions at 800°C and 250 psi produced mostly Fe_3O_4. Conditions at 725°C and 50 psi produced FeO. Conditions of 725°C and 515 psi along with 750°C and 250 psi continued until the iron began re-oxidizing. Conditions at 725°C and 250 psi appear to also have allowed the iron to re-oxidize. This is verified by the increase in CO_{Fe2O3}/CO_{WGS} and points to the significance of the hematite residence time as a variable in a commercial operation.

4.6.3 Addition of CaO

The ultimate goal of this reactor was to adsorb all CO_x to produce high-purity hydrogen. The initial tests for hydrogen production focused the study in the areas of 725°C and 250 psi. The reactor was loaded with 50 g of a 1:7 mass ratio of Fe_2O_3:CaO. Analysis of the additive performance of the CaO and as a CO_x adsorber in combination with the Fe_2O_3 was performed by determining the fractional conversion of CO_x to $CaCO_3$ as compared to the CO_x concentration in the outlet of the empty reactor (involving only the WGS) under the same conditions. Dimensionless time, reactor flow and fluidization velocity were treated the same as with the iron

solids analysis. An example of Fractional CO_x conversions is shown if Figure 32. Further figures are included in the appendix H.

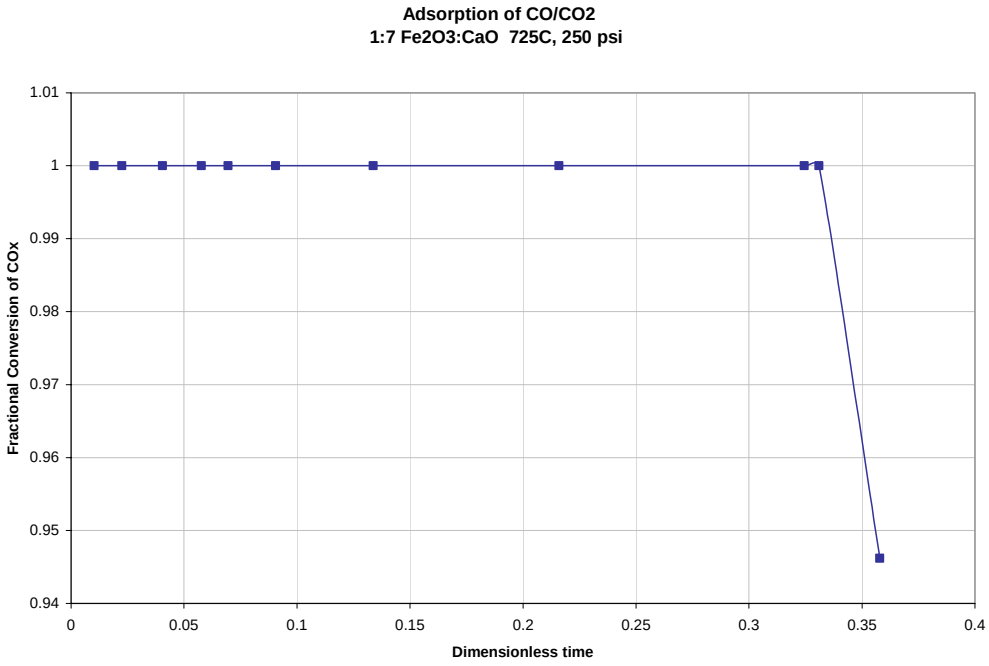

Figure 32: Adsorption of CO_x – 1:7 Fe_2O_3:CaO – 725°C, 250 psi

The CO_x adsorption by the CaO in the reactor was affected by the reduction of ferric oxide under all conditions. Carbon oxides were completely adsorbed during the reaction for significant amounts of time at all combinations of 725°C, 750°C, 50 psi and 250 psi. The flow rate at 725°C and 50 psi was too low to measure the limits of the reaction capacity. At 250 psi and temperatures of 725°C and 750°C, the fractional conversion dropped below 1 when the CO conversion from ferric oxide reduction fell to around 10%. However, this was not the case at 725°C and 515psi. Even though the CO conversion reached 0.10 after a dimensionless time of 0.6, the CO_x adsorption only reached a maximum of near 65%. Although the CO_x adsorption was still proportional to the fractional conversion of CO by Fe_2O_3, the calcium oxide was unable to adequately adsorb the CO_x. This may be due to physical changes in $CaO/CaCO_3$ at high pressures. Agglomeration of the solid was noted at 250 psi, and was acute at 515 psi. Figures in Appendix I show the solid at each condition after a single run. The high pressure could also

effect the surface of the calcium oxide particle, creating a non-porous external layer, as noted in the literature review.

At 800°C and 250psi, the CO_x adsorption was fairly constant, with scatter around 0.8. The fractional conversion of carbon monoxide during ferric oxide reduction was also fairly constant at 0.17. Even though this was above the 10% limit noted at lower temperatures at 250 psi, complete adsorption never occurred. The high temperature obviously shifts the calcium oxide/calcium carbonate reaction toward decomposition

X-ray diffraction analysis of the solids removed from the reactor supports these conclusions (figures in appendix J). At 725°C and 50 psi, only $CaCO_3$ and $Ca(OH)_2$ are present, with no CaO indicated. However, both CaO and $CaCO_3$ are present in the results for all combinations of temperatures at 250 psi and at 725°C and 515 psi. Since higher partial pressure of CO_2 should shift the calcium reaction toward carbonation, the appearance of CaO is probably a result of the observed agglomeration and possible surface changes in the pore structure. The inability of the CaO to adsorb all CO_2 in the reaction at 800°C and 250 psi is most likely a result of a combination of agglomeration / surface pore clogging and the decomposition shift caused by higher temperature.

From stoichiometry, a total of 24.375 g of oxygen was expected to be lost if the entire 6.25g of Fe_2O_3 was converted to FeO and all of the 43.75g of CaO was completely carbonated to $CaCO_3$. Both CaO and $CaCO_3$ were found in the solids by x-ray diffraction for all conditions except 725°C and 50 psi. All CO_x was adsorbed, with none appearing in the outlet for these conditions, even though the mass balance showed only a 4.924 g deficit of oxygen. This was explained by the appearance of $Ca(OH)_2$, which resulted from the conversion of the remaining CaO and adsorbed some of the oxygen from the inlet. The low volume flow rate of CO into the system at 50 psi probably explains the secondary formation of $Ca(OH)_2$ from the steam. An increase in the volume of CO to reach the CaO would prevent this from occurring.

The experiment performed at 725°C and 250 psi resulted in a 36.212 oxygen deficit, however some CaO remained. This may be explained by the existence of Fe_3O_4 as well as FeO in the solid. The iron reaction did not continue to completion, leaving some magnetite from the decomposition. All other mass balance numbers indicate only a partial carbonation of the lime, agreeing with the x-ray results.

The lack of $Fe_2O_3$and Fe_3O_4 in the x-ray diffraction results indicate that the length of each run was appropriate to reduce the iron without allowing re-oxidation, with the exception of the 725^{o}C, 250 psi experiment. Input of reactant gases for conditions of 800^{o}C, 250 psi; 725^{o}C, 50psi; and 725^{o}C, 250psi was extended in order to determine the limits for high-purity hydrogen production and to catch the limit of CO_x adsorption. The 40 minutes used for input of syngas was too long, and allowed the re-oxidation of the FeO.

Iron carbide was found under all conditions except 725^{o}C, 250 psi and 725^{o}C, 50 psi. The carbonation of iron only occurs near the completion of the decomposition process and the formation of elemental iron. Adjusting the inlet gas composition and/or shortening production time should prevent FeC formation by limiting the extent of the decomposition of the iron compounds.

4.6.4 Mass Balance

Errors in the mass balance of the empty reactor are quite high, considering the only reaction causing a change in the number of molecules of a substance would be the deposition of carbon caused by the Bouduard reaction. However, the cumulative error in the flow rate measuring system was calculated at 14.2%. Coupled with the gas chromatograph error of 0.25%, the results can be considered reasonable. The reversible WGS resulted in water condensation at both the top and bottom flanges, allowing only an estimate of water leaving the outlet gas. It was also very difficult to collect and measure the carbon deposited on the sides of the reactor. In most cases, the amount was not recoverable. When it was, the carbon was collected with small particles of ceramic coating that had flaked off the interior during the experiment, resulting in on erroneously high value. High pressure and steam created a corrosive environment for the liner.

Another problem encountered in the attempt to create a mass balance involved the length of the study. The nitrogen purge was continued for an extended amount of time, however, no experiment ever resulted in complete nitrogen in the analysis of the last sample collected. The number of samples collected were limited to the amount able to be analyzed by the gas chromatograph in 12 hours, with the samples collected during active reaction periods analyzed within a few hours of collection. A longer time period between collection and analysis resulted in erroneous results, indicating significant leakage. To account for this, only a fraction of the inlet mass was used for the mass balance, depending on the length of time syngas was introduced

into the system, and the flow rate of the inlet. The fractional inlet time is noted in the graph under "Temperature." If no fraction of inlet time is indicated, the entire mass introduced was used in the balance.

The overall error was lower with a solid load of 50 g of hematite in general, possibly because of the exothermic nature of the reaction. This would increase the velocity of the outlet gas, allowing more of the molecules to be sampled and recognized. The carbon deposition was greater, allowing greater ease in its collection and measure. There was also less noticeable moisture on the gaskets when the reactor was opened. Small errors above the instrumental error can probably be accounted for by unmeasured deposition.

From stoichiometry, and the step-wise decomposition of hematite to iron, a product of Fe_3O_4 should produce a 1.67g surplus of oxygen; FeO should produce a 5 g surplus; and elemental iron, a 15 g surplus of oxygen. Based loosely on this assumption, conditions at 800^{o}C and 250 psi produced mostly Fe_3O_4. Conditions at 725^{o}C and 50 psi produced FeO. Conditions of 725^{o}C and 515 psi along with 750^{o}C and 250 psi continued until the iron began re-oxidizing. Conditions at 725^{o}C and 250 psi appear to also have allowed the iron to re-oxidize, although the increase indicates the decomposition stopped near the wustite boundary.

From stoichiometry of a reactor loaded with 50 grams of the 1:7 mass ratio of Fe_2O_3: CaO, a total of 24.375 g of oxygen was expected to be lost if the entire 6.25g of Fe_2O_3 was converted to FeO and all of the 43.75g of CaO was completely carbonated to $CaCO_3$. A little over 21 grams was lost at the 800^{o}C, 515 psi experiment and an approximate 36g oxygen deficit was recorded for the experiment performed at 725^{o}C and 250 psi. Other mass deficits of oxygen indicate varying degrees of carbonation of the calcium oxide and decomposition or re-oxidation of the iron compounds. In order to understand this further, x-ray diffraction analysis of those experiments near the optimum condition for the production of high-purity hydrogen production were analyzed using x-ray diffraction and are discussed in the analysis of the CO_x conversion of the 1:7 solids mixture.

4.6.5 Cycling of Hydrogen Production and Regeneration of Solids

The first hydrogen-production cycle succeeded in producing an outlet comprised of around 18% hydrogen and 82% nitrogen (Figure 34). The carbon dioxide production in the regeneration process was very low, but did increase with increasing temperature. The oxidation

of the iron compound happened very quickly, as indicated by the reactor temperature (Figure 35), and high percentages of oxygen were always present in the outlet until the nitrogen purge. A small amount of CO_2 mixed only with nitrogen was present in the outlet sample after the purge.

The second hydrogen generation cycle produced a greater volume percentage of hydrogen, but also greater quantities of CO, CO_2, and CH_4 when compared to the first cycle. The high percentage of CO_2 and CO probably indicates incomplete decomposition of $CaCO_3$ in the regeneration cycle. An examination of the solids after the entire cycle revealed almost complete agglomeration (Figure 33). Previous hydrogen production experiments under the same conditions found that agglomeration was a function of both pressure and temperature. Continued fluidization throughout the entire cycle should be possible at lower pressures (50 psi or lower) and by maintaining a temperature low enough to be practical.

Figure 33: Solids of 1:7 Fe_2O_3:CaO Mixture After One Hydrogen Generation Cycle

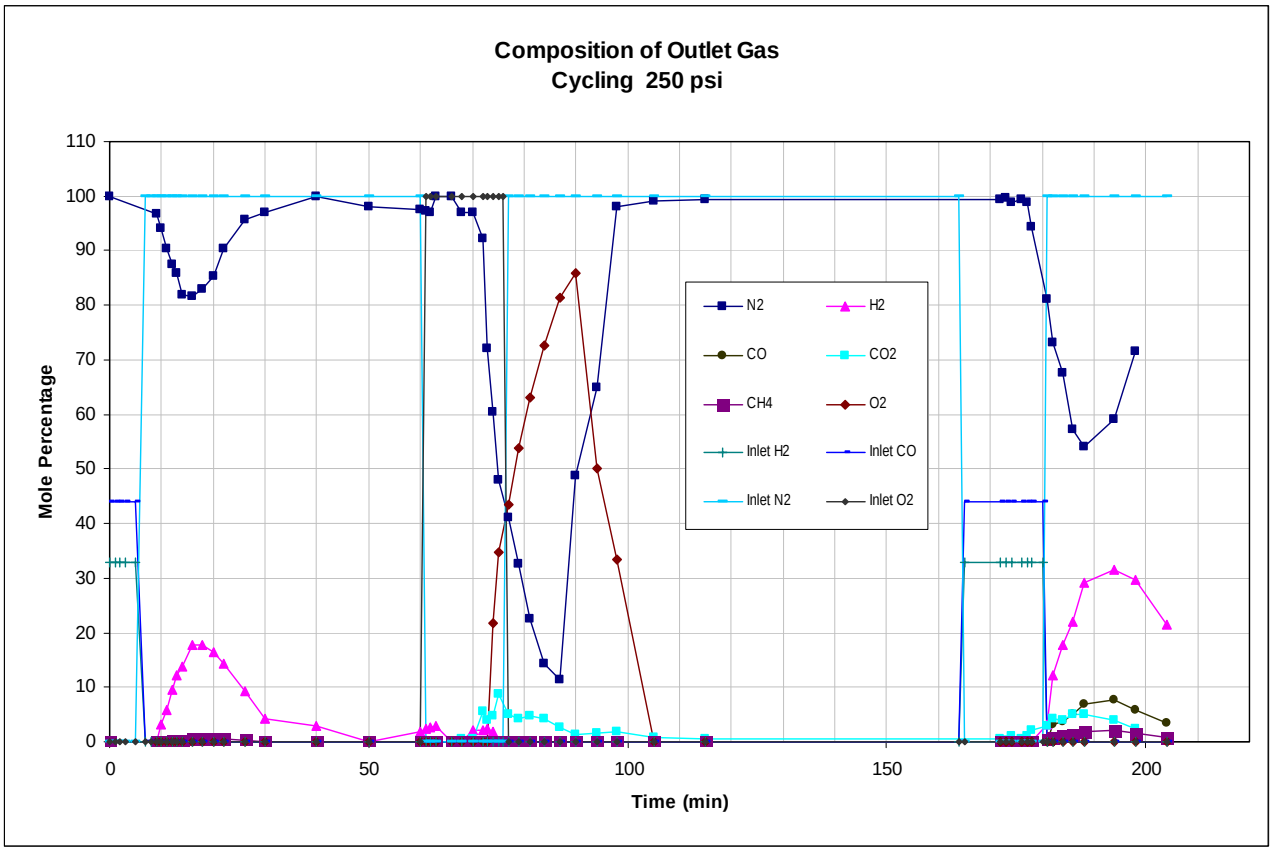

Figure 34: Composition of Outlet Gas During Cycling at 250psi

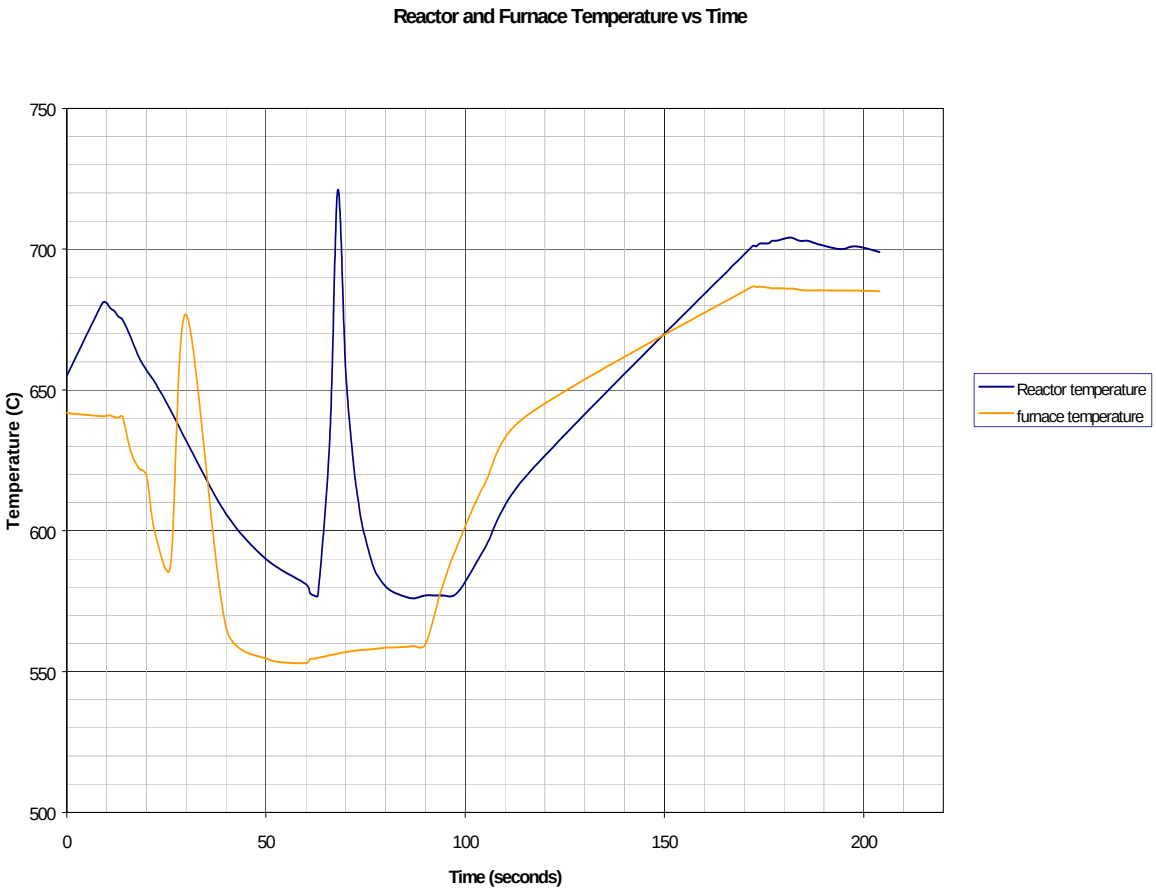

Figure 35: Reactor and Furnace Temperatures During Cycling at 250 psi

4.6.6 SEM Analysis

Solid samples after selected experiments as well as samples of Fe_2O_3 and CaO in as received conditions were evaluated using scannig electron microscopy analysis.

The decomposition of hematite in the fluidized bed changes the pore structure of the resulting iron particle, with temperature having a pronounced effect on the surface characteristics. The baseline scanning electron microscope image of a sample of the hematite used in the process (Figure 36) shows extensive surface pores and a variety of particle sizes.

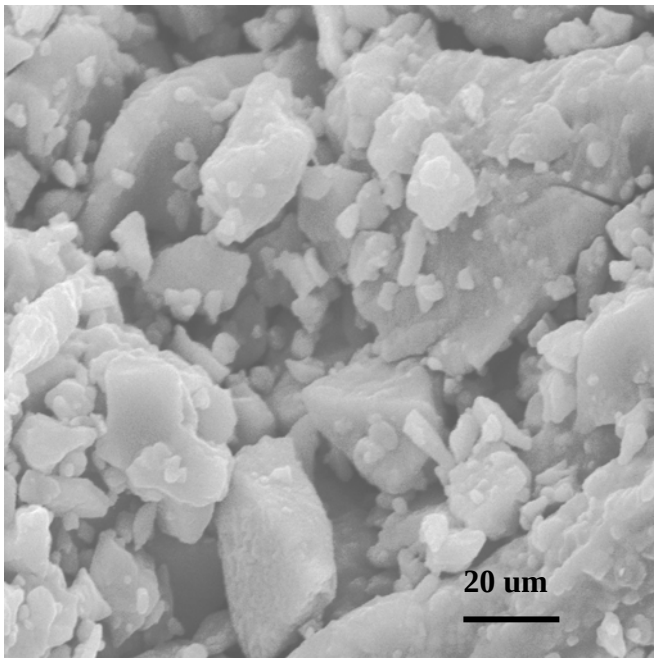

Figure 36: Fe_2O_3, Detail, Mag. 6000x, As Received

After decomposing, the particles displayed a glassy surface apparently as a result of a changing morphology (see Figures 37-39).

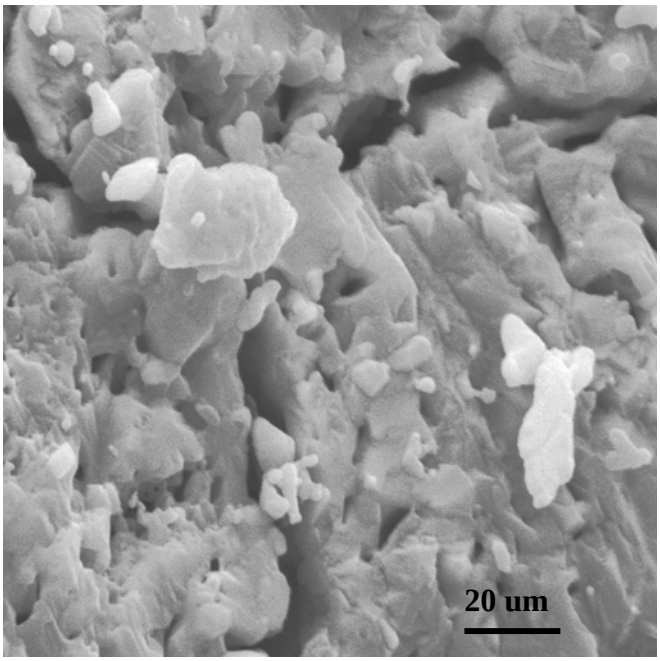

Figure 37: Fe_2O_3, Detail, Mag. 6000x, Test 800^{o}C 250 psig

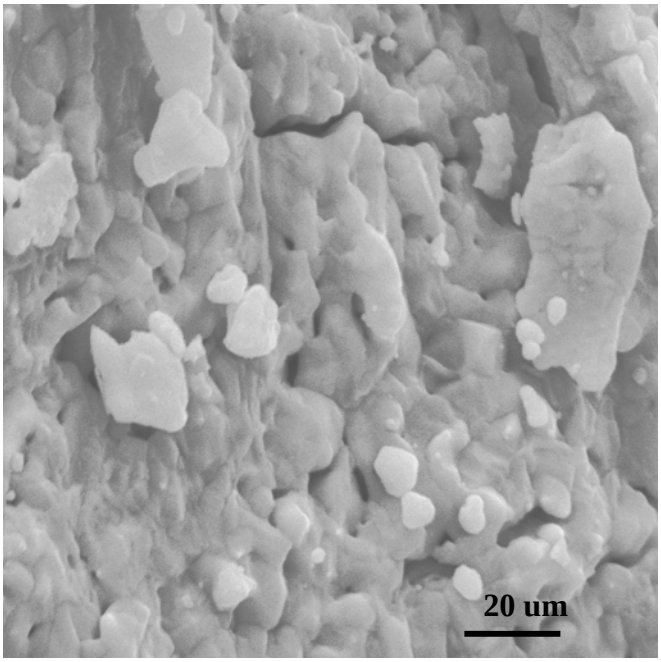

Figure 38: Fe_2O_3, Detail, Mag. 6000x, Test 725^{o}C, 515 psig

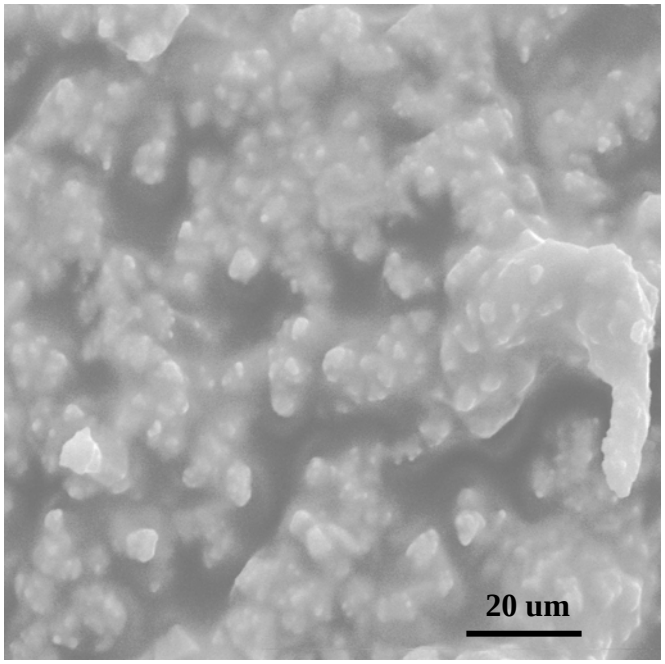

Figure 39: MIX, Fe_2O_3 Detail, Mag. 6000x, Test 725^{o}C, 50 psig

Inspection of the hematite/iron sample after one full cycle consisting of decomposition at 725°C and 250 psi, oxidation at 600°C and 250 psi, and decomposition at the original conditions resulted in SEM (Figure 40).

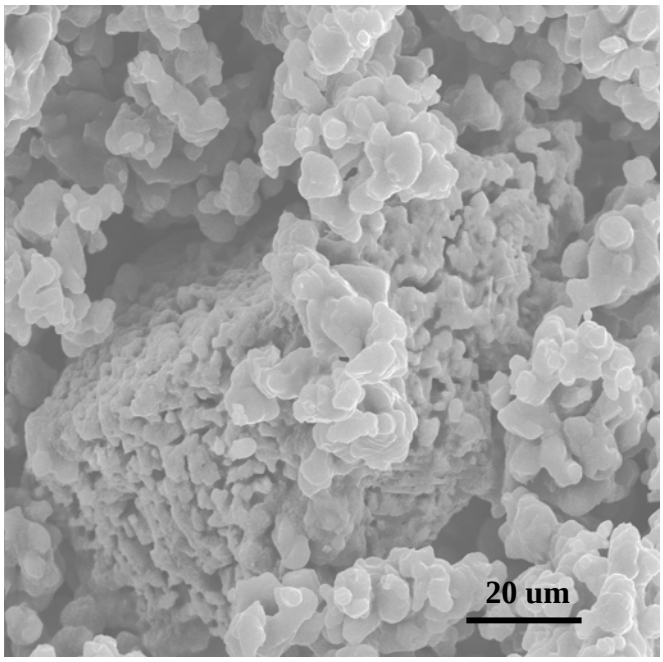

Figure 40: MIX, detail, mag.. 6000x, test 725C, 250 psgi., regeneration cycle.

The iron particle displays the spongy surface characteristic typical of the observed temperature effect noted in the other samples.

Calcium oxide was carbonated in the hydrogen production process in a mass ratio of 7:1 with the hematite. Scanning electron microscope images of a representative sample of the used CaO in as received condition are shown in Figure 41.

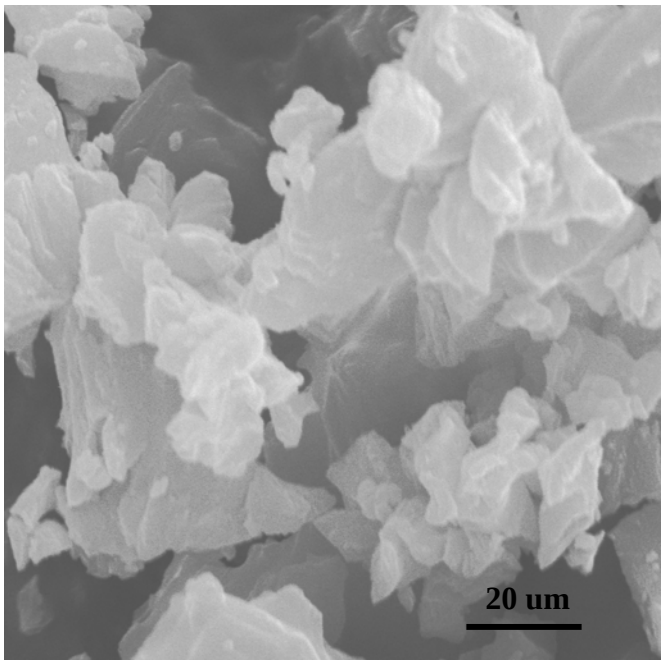

Figure 41: CaO, Detail, Mag. 6000x, As Received.

The stratified layering of the surface of the original CaO gives the sample a large surface area. After processing at 725°C and 50 psi, the layering is less noticeable and seems to disappear completely at 800°C and 515 psi (Fig 40 and 43). Surface porosity appears to decrease with both temperature and pressure. Pore size decreases from 50 psi to 515 psi at 725°C (Fig. 42 and 43). The structure of the $CaCO_3$ becomes almost filamentous at 800°C(Fig 44).

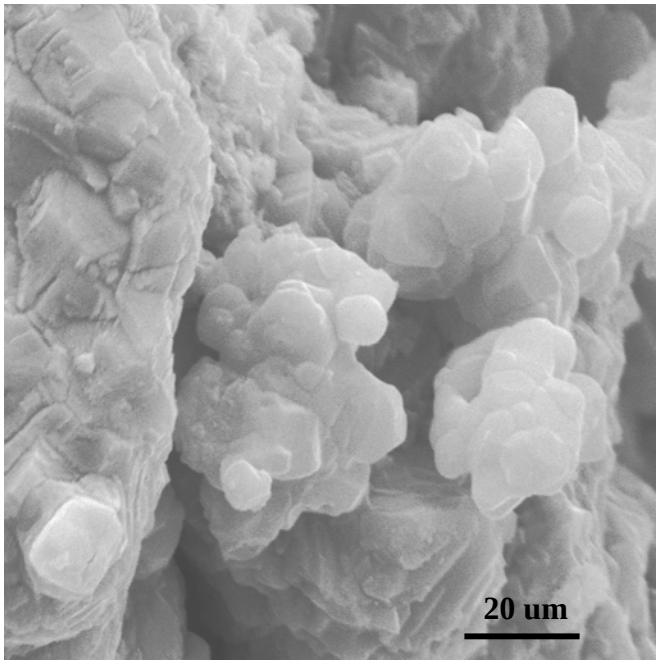

Figure 42: MIX, CaO Detail, Mag.. 6000x, 725^{o}C, 515 psig.

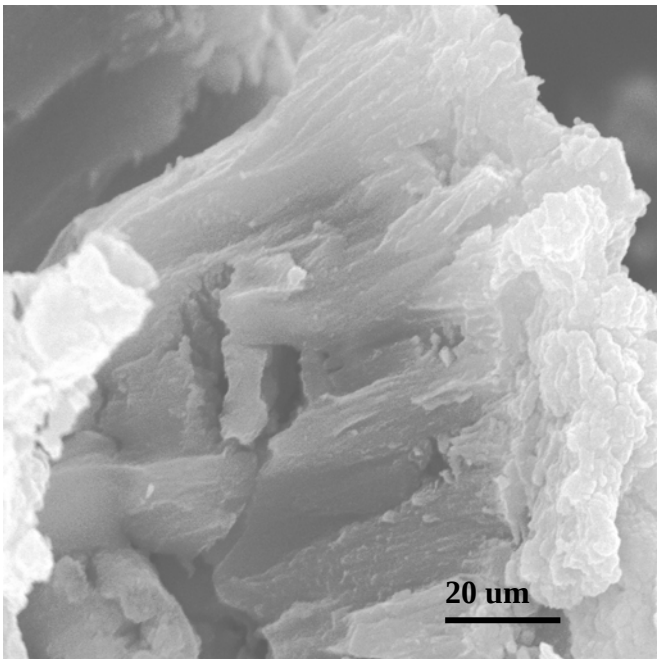

Figure 43: MIX, CaO Crack Detail, Mag.. 6000x, 725^{o}C, 515 psig.

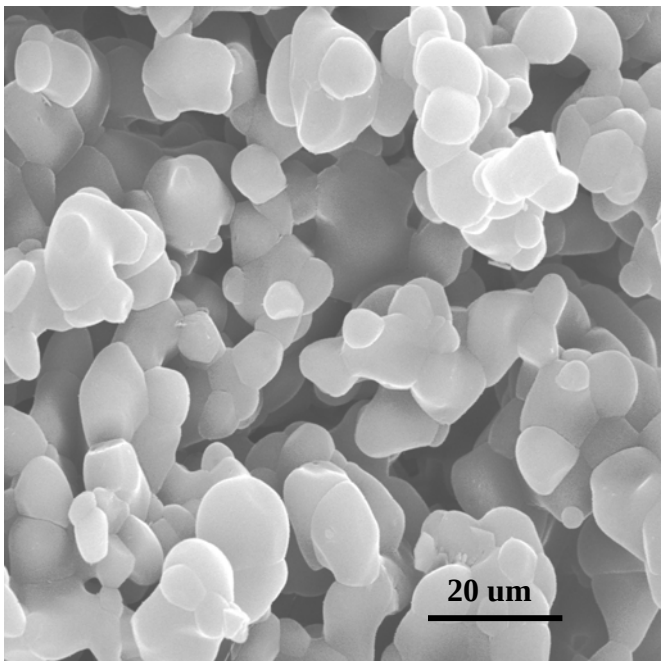

Figure 44: MIX, CaO Detail, Mag.. 6000x, 800^{o}C, 515 psig.

The $CaCO_3$ resulting from a complete cycle displayed extreme agglomeration and smaller pores when compared to $CaCO_3$ produced at 725°C and 50 psi (Figure 45). Composite views of the $CaCO_3$ produced under various conditions illustrate the increase in particle agglomeration with both temperature and pressure (Fig 43-45). SEM images of the resulting $CaCO_3$ after the process illustrate the agglomeration of the solid, also noticed macroscopically, that increased with both temperature and pressure.

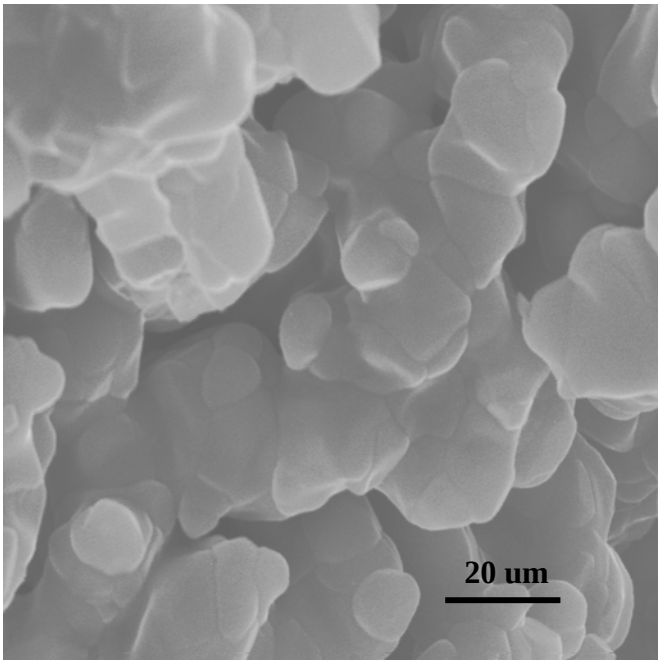

Figure 45: MIX, CaO Detail, Mag.. 6000x, Test 725^{o}C, 250 psig., regeneration cycle.

4.7 Cyclic Fixed-bed Reactor (Task 5)

The cyclic fixed-bed reactor system was originally designed to reform natural gas to syngas. This system was modified to reform natural gas to syngas and then convert syngas to H_2 and CO_2 in the downstream bed. Figure 46 shows typical hydrogen concentrations from the first bed during reforming (this gas is fed to the FeO reactor).

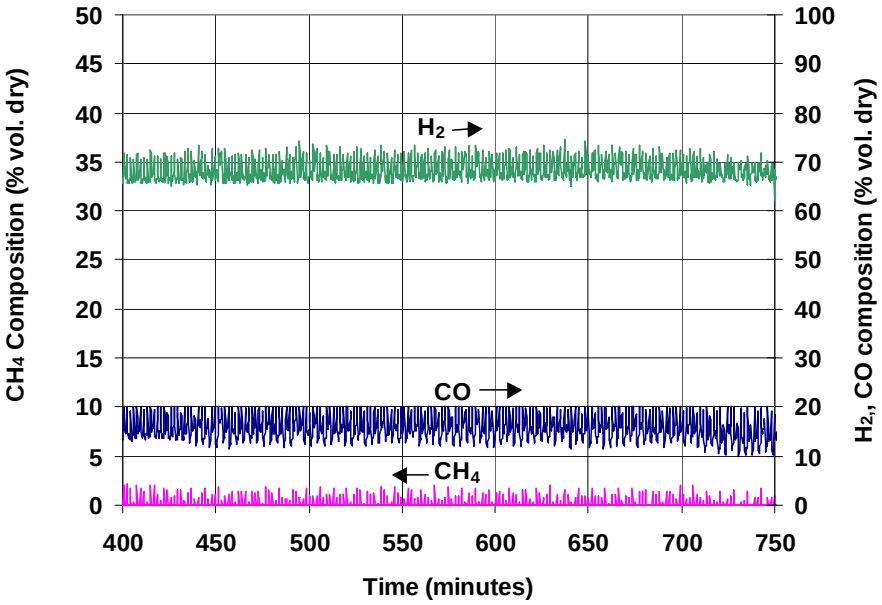

Figure 46: Typical Syngas Outlet concentrations of reactor 1 (Ni) Being Delivered to Reactor 2 (FeO, CaO) in Fixed Bed Reactor (From DOE Grant "Conversion of natural gas to PEM Fuel Cell grade H_2", Contract # DE-FC02-97EE50488)

The FeO reactor was loaded with iron oxide and calcium oxide catalyst. Using the exothermicity of the iron oxide and comparing that to the exothermicity of the current Ni catalyst a safe amount of FeO was calculated. The bed was loaded with 50 kg of FeO and 68 kg of CaO.

During initial runs the temperature in the second reactor decreased rapidly over only a couple of cycles. The amount of active FeO, due to the non-porous nature of the pellets, was unable to provide enough heat to sustain the hydrogen producing reaction. The equilibrium calculation chart (Figure 47) demonstrates the need for a temperature swing from 550°C to 850°C for successful adsorption of CO_2 and regeneration of $CaCO_3$. At high temperatures carbon dioxide is released from the calcium carbonate, while low temperatures are required for carbon dioxide capture and the reaction between iron oxide and carbon monoxide. The exothermic swing during initial testing was only 100°C and fell far short of the required 300°C temperature swing required.

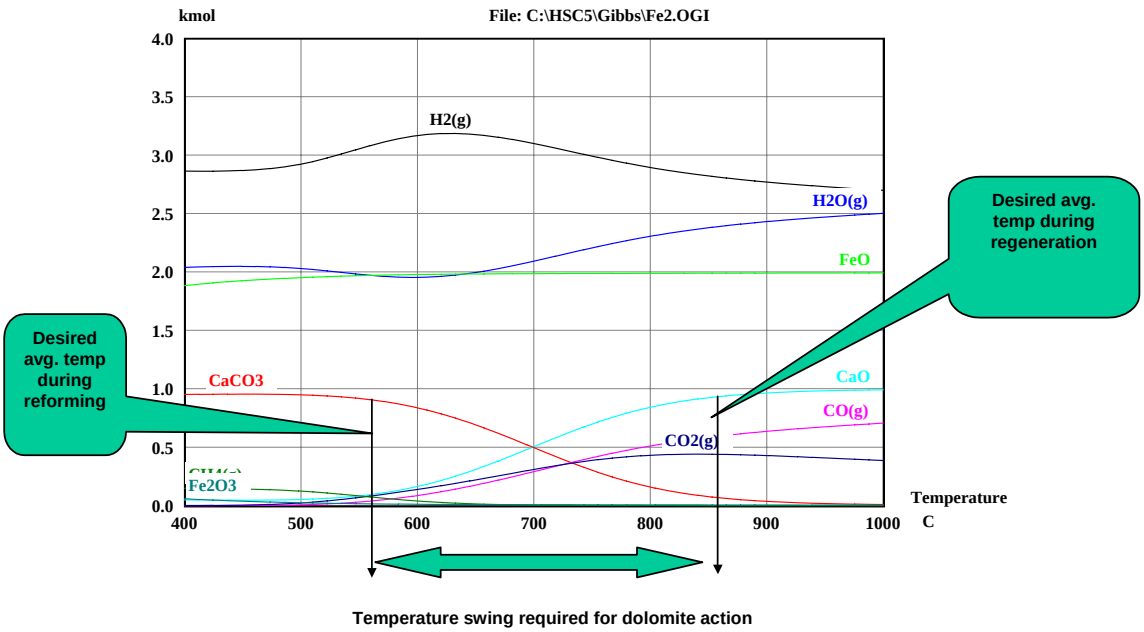

Figure 47: Theoretical Temperature Swing Requirement For FeO/CaO Fixed Bed Reactor

Based on this information reactor tests were run with the assumption that a large enough temperature swing (provided by burners) would guarantee the full regeneration of the catalyst. By using heat injection while flowing air across the iron oxide bed the bed was fully regenerated at a high temperature (850C). Figure 48 shows the changes in concentration in the reformate stream across the second reactor. Reforming in the first bed produced a syngas stream (with dry compositions of 65% hydrogen and 8% carbon monoxide). The hydrogen concentration of this gas stream was increased to 85% as CO_2 was adsorbed. The CO was also decreased from 7.5% to 1.5% due to the reaction with the iron oxide. Thus the concept of simultaneous production of high purity hydrogen with CO_2 separation was proved using the fixed bed 2-reactor bench-scale system.

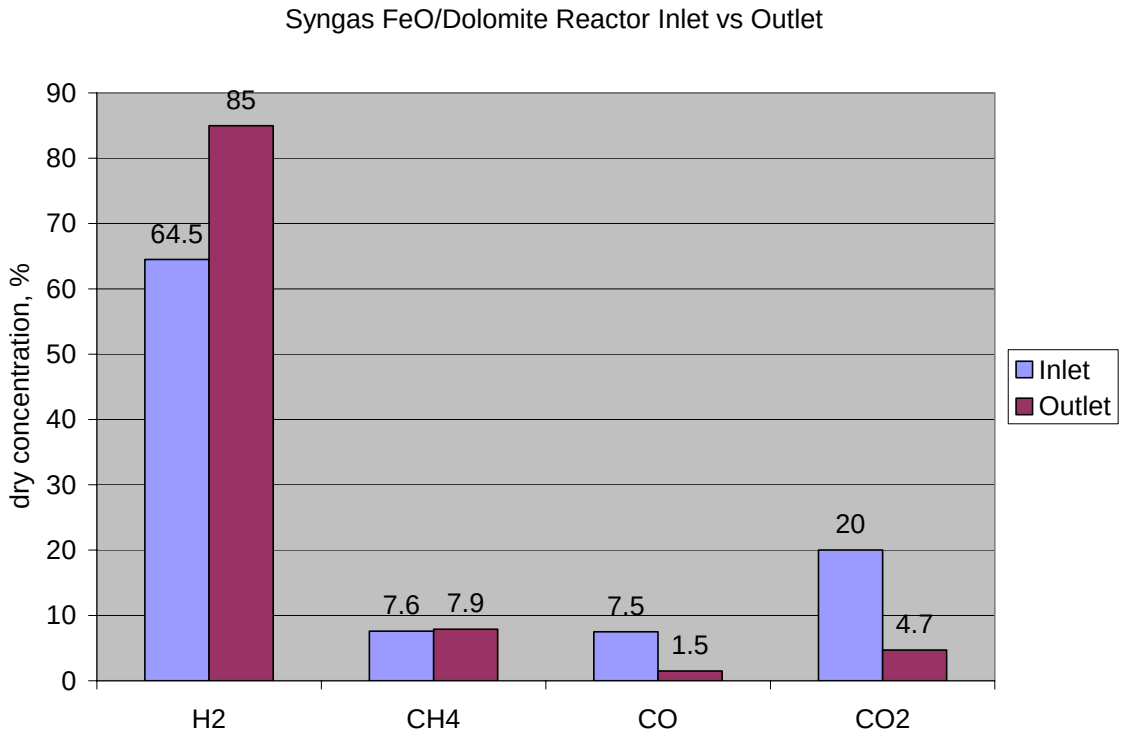

Figure 48: Syngas Fe_2O_3/CaO Bed Inlet and Outlet Concentrations (Fixed Bed)

5.0 – CONCLUSIONS

Tests in a lab-scale fluidized bed reactor demonstrated the process for the conversion of syngas to high purity H_2 and separated CO_2. The purity of hydrogen reached levels up to 95% on a dry basis. The tests indicated that CaO captured a significant portion of CO_2 produced forming $CaCO_3$.

Extensive thermodynamic analysis, of all likely reactions that can take place between the syngas and the solids, determined an optimum temperature and pressure operating range for generation of H_2 and separated CO_2. Over the optimum range of operation, the extent of the undesirable reactions, such as carbon forming Boudouard reaction and the parasitic methane formation, is minimum.

The kinetics of the iron oxide reactions is fast, whereas the kinetics of the calcium reactions is slow. That is why the mass ratio of CaO to Fe_2O_3 was chosen as 7 to 1. In the hydrogen production tests with a CaO to Fe_2O_3 mass ratio of 7 to 1, the pressure did not have a significant

effect on the hydrogen concentration. However, the concentrations of CO, CO_2 and CH_4 were affected significantly by pressure.

Blank runs with inert sand as the fluidization medium, showed that the water gas shift reaction (CO (g) + H_2O (g) = CO_2 (g) + H_2 (g)) reaches equilibrium very fast. High pressures resulted in formation of methane via the methanation reaction (CO (g) + 3 H_2 (g) = CH_4 (g) + H_2O (g)), whose equilibrium is expected to be favored at high pressures. The carbon forming Boudouard reaction (2 CO (g) = C (s) + CO_2 (g)), should not be significant under conditions of high temperatures and 23% steam in the feed mixture. Nevertheless, traces of carbon were observed in the fluidized bed reactor inlet, which reached temperatures of 400^o C.

In the laboratory scale fluidized bed reactor, tests were also performed with only iron oxide as the fluidized solid, to analyze the reduction of iron oxide. The iron oxide tests suggest that the CO adsorption/reaction with iron oxide is affected by potential side reactions, such as iron carbide (Fe_3C) formation and carbon formation. The deep reduction of iron oxide to form metallic iron could also play a role here. The latter reaction must be minimized if a steady state hydrogen production and oxygen regeneration cycle is to be sustained.

A hydrogen production and oxygen regeneration cycling test was performed at 725^{o}C and 250 psig in the laboratory scale fluidized bed reactor loaded with a mixture of iron oxide and $CaCO_3$ under a 1:7 mass ratio. A mixture of syngas was fed over the catalyst to produce hydrogen and then the solid bed was regenerated by flowing oxygen. Finally, the syngas was again fed over the regenerated $Fe_2O_3/CaCO_3$ mixture to produce hydrogen.

The first hydrogen-production cycle succeeded in producing an outlet comprised of around 18% hydrogen and 82% nitrogen. The carbon dioxide production in the regeneration process was very low, but did increase with increasing temperature. The oxidation of the iron compound happened very quickly, as indicated by the reactor temperature, and high percentages of oxygen were always present in the outlet until the nitrogen purge. A small amount of CO_2 mixed only with nitrogen was present in the outlet sample after the purge.

The second hydrogen generation cycle produced a greater volume percentage of hydrogen, but also greater quantities of CO, CO_2, and CH_4 when compared to the first cycle. The high percentage of CO_2 and CO probably indicates incomplete decomposition of $CaCO_3$ in the regeneration cycle. An examination of the solids after the entire cycle revealed almost complete agglomeration. Previous hydrogen production experiments under the same conditions found that

agglomeration was primarily a function of pressure. Continued fluidization throughout the entire cycle should be possible at lower pressures (50 psi or lower) and by maintaining a temperature low enough to be practical.

Indeed, Scanning Electron Microscopy (SEM) characterization of fresh and used catalysts showed pronounced changes in the catalyst morphology during the hydrogen production step. After the hydrogen production step, the particles became smaller in size, more round in the edges and develop a glassy appearance. SEM characterization of used CaO and Fe_2O_3 particles showed agglomerates of small CaO particles, clearly distinguishable from the spongy Fe_2O_3 particles. Changes in catalyst morphology may the most dominant factor affecting the process during repeated cycling between hydrogen production and oxygen regeneration. It should be noted that the exact conditions of the cycle test were not under control. A large exotherm occurred during the regeneration step. The temperature was monitored on the outside of the bed. Thus the maximum temperature of exposure is not known. Further the bed may have slumped during the change from hydrogen production to regeneration. Further testing with extra temperature modeling is recommended.

The cyclic fixed-bed reactor system was originally designed to reform natural gas to syngas. This system was modified to reform natural gas to syngas and then convert syngas to H_2 and CO_2 in the downstream portion of the bed. Testing demonstrated ability to adsorb the CO_2 and increase the hydrogen concentration of the syngas during hydrogen production. This bed was then regenerated at high temperature and low pressure, allowing CO_2 separation, and then returned to the hydrogen production stage. Hydrogen concentration was increased from 65% to 85% (dry concentration). Maintaining complete regeneration of the bed was the main factor in this cyclic process.

5.0.1 Recommendations

Agglomeration and probable surface changes make the use of 20 μm CaO particles impractical at pressures much above atmospheric pressure. Although optimum hydrogen production occurred around 250 psi, the agglomeration of the solids made fluidization impossible after the first hydrogen-production cycle. These characteristics of the solid prevented complete regeneration in a reasonable amount of time. The experiments at 800^{o}C shifted the $CaO/CaCO_3$ reaction toward decomposition.

In order for this solid to be regenerable, the process must occur as close to atmospheric pressure as possible. The reactor designed for this study was sized for gas flows up to 515 psi, and made it impossible to operate a complex cycle at the fluidization velocities required for the low pressures. The hydrogen production cycle performed well at low temperatures and pressures, and a low pressure/high temperature regeneration cycle could produce a viable recycled solid capable of good performance over many production cycles. The fixed bed reactor did operate at nearly atmospheric pressures and did regenerate if temperatures were increased. Temperature control schemes to control the amount of air to the reactor, amount of inert catalyst, and heat loss in the bed were designed and further testing. Porous iron oxide catalyst may also be used to keep the ratio of iron oxide to calcium oxide in the preferred range.

6.0 – REFERENCES

[1] U.S. Department of Energy; *World Energy Consumption Trends*, **2000**,1-14, Retrieved August 10, 2000 from the World Wide Web: http://www/eia.doe.gov/oiaf/ieo95/trends.html.

[2] U.S. Department of Energy; Vision 21 a Concept for Tomorrow's Pollution-Free Energy Plant. *Fossil Energy,* **2000**, 1-4. Retrieved August 1, 2000 from the World Wide Web:http://www/gils.doe.gov: 1782/cgi-bin/w3vdkghw;qryQIBJ15U_;doecrawl-021135.

[3] United States Environmental Protection Agency; Program Overview. *Acid Rain Program*, **2000**, 1-2. Retrieved August 11, 2000 from the World Wide Web: http://www.epa.gov/acidrain/overview.html

[4] U.S. Department of Energy; DOE Selects First Vision 21 Projects to Design the Energy Plant of the Future. *DOE Fossil Energy Techline*, **2000**, 1-5, Retrieved August 1,2000 from the World Wide Web: http://gils.doe.gov: **1782**/cgi-bin/w3vdkghw?qryKKB.CROS_;doecrawl-022399.

[5] Gupta, C. K., Sathiyamoorthy, D., 1999, *Fluid Bed Technology in Materials Processing*, CRC Press, Washington, D. C.

[6] Yates, J.G., 1983, Fundamentals *of Fluidized-be Chemical Processes,* Butterworths, London.

[7] O. Boudouard, *Ann. Chim. Phys*., 24 (1901) 85.

[8] Y.T. Chein and Y-C Ko, *Amer. Cer. Soc. Bull*., 62 (1983) 779.

[9] J. Fienman, Direct Reduction and Smelting Processes, *Iron Making Volume*, AISE Steel Foundation, Pittsburg, PA (1999) 763.

[10] B. H. Davis and E Iglesia, "Technology Development for Iron and Cobalt Fischer-Tropsch Catalysts", Quarterly Report- DE-FC26-98FT40308, April30, 1999.

[11] S. Sawai, Y. Iguchi, and S, Hayashi, *J. of the Iron and Steel Institute of Japan*, 84 (1998) 844.

[12] M. Shimokawabe, *Thermochim. Acta.*, 28 (1979) 287.

[13] M. V. C. Sastri, R. P. Viswanath; B. Viswanath, *Int. J. HydrogenEnergy*, 7 (1982) 951.

[14] K. Ishii, T. Akiyama, Y. Kashiwaya, S. Kondo, *Memoirs of the Faculty of Engineering*, Hokkaiod University, Sapporo, Japan, 17 (1986) 1.

[15] O. J. Wimmers, P. Arnoldy; J. A.Moulijn, *J. Phys. Chem*., 90 (1986) 1331.

[16] J. Jankowski, A. Sadowski, *Iron Making and Steel Making,* 23 (1996) 479.

[17] Y.K. Rao, P. Pichestapong, *Proc. of 9th Int. Conf. on High Temperature Materials Chemistry*, K.E. Spear (ed.), Electrochemical Society, (1997) 211.

[18] A. -H. A. El-Geassy, *Scandinavian Journal of Metallurgy*, 27 (1998) 205.

[19] I. J. Moon, C. H. Rhee, *Proc of the 1997 TMS Annual Meeting,* Feb 9-13, Orlando, FL, Minerals Metals and Materials Society, Warrendale, PA, USA, (1997) 649.

[20] I. J. Moon, C. H. Rhee, D. J. Min, *Steel Research*, 69 (1998) 302.

[21] H. W. Kang, W. S. Chung, and T. Murayama, *ISIJ International*, 38 (1998) 109.

[22] A. Habermann, F. Winter, H. Hofbauer, J. Zirngast, J. L. Schenk, J. L., *ISIJ International*, 40 (2000) 935.

[23] I. V. Murin, V. M. Smirnov, G. P. Voronkov, V. G. Semenov, B. M. Sinelnikiv, *Solid State Ionics*, 133 (2000) 203.

[24] M. J. Tiernan, P. A. Barnes,G. M. B. Parkes, *J. Phys Chem. B*, 105 (2001) 220.

[25] Y. Xiao, M. A. Reuter L. Holappa L., *Proceedings of the Ninth International Ferroalloys Congress and the Manganese 2001 Health Issues Symposium,* Ferroalloy Association, Quebec City, Canada, June 2001, (2001) 147.

[26] T. Mattison, A. Lyngfelt, P. Cho, *Fuel*, 80 (2001) 1953.

[27] Cuenca, M. Alvarez, Anthony, E. J., 1995, *Pressurized Fluidized Bed Combustion*, Blackie Academic & Professional, Glasgow, UK.

[28] Levenspiel, Octave, 1972, *Chemical Reaction Engineering*, John Wiley & Sons, New York, N. Y.

[29] Kunii, Daizo, Levenspiel, Octave, 1969, *Fluidization Engineering*, John Wiley & Sons, New York, N. Y.

[30] Reid, Robert C., Prausnitz, John M., Poling, Bruce E., 1987, *The Properties of Gases and Liquids*, McGraw-Hill Book Co., New York, N. Y.

[31] Sohn, Hong Young, Wadsworth, Milton E., 1979, *Rate Processes of Extractive Metallurgy*, Plenum Press, New York, N. Y.

[32] Borgwardt, R.H., 1985, "Calcination Kinetics and Surface Area of Dispersed Limestone Particles," AIChE Journal, Vol. 31, pp103-111.

[33] Hills, A. W. D., 1978, "The Importance of Convective Mass Transfer in the Reduction of Hematite," Metallurgical Transactions B, Vol. 9B, pp. 121-128.

[34] Boynton, Robert S., 1966, *Chemistry and Technology of Lime and Limestone*, John Wiley & Sons, New York, N. Y.

[35] Fuller, E. L., Yoos, T. R., 1987, "Surface Properties of Limestones and Their Activation Products," Langmuir, pp. 753-760.

[36] Fenouil, Laurent A., Towler, Gavin P., Lynn, Scott, 1994, "Removal of H_2S from Coal Gas Using Limestone: Kinetic Considerations," Ind. Eng. Chem. Res., Vol. 33, pp 265-272.

[37] Fenouil, Laurent A., Lynn, Scott, 1995, "Study of Calcium-Based Sorbents for High-Temperature H_2S Removal. 1. Kinetics of H_2S Sorption by Uncalcined Limestone," Ind. Eng. Chem. Res., Vol. 34, pp 2324-2333.

[38] Fenouil, Laurent A., Lynn, Scott, 1995, "Study of Calcium-Based Sorbents for High-Temperature H_2S Removal. 1. Kinetics of H_2S Sorption by Calcined Limestone," Ind. Eng. Chem. Res., Vol. 34, pp 2234-2347.

[39] Beruto, Dario, Boter, Rodolfo, Searcy, Alan W., 1984, "Thermodynamics and Kinetics of Carbon Dioxide Chemisorption on Calcium Oxide," The Journal of Physical Chemistry, Vol. 88, pp. 4052-4055.

[40] Borgwardt, Robert H., 1989, "Calcium Oxide Sintering in Atmospheres Containing Water and Carbon Dioxide," Ind. Eng. Chem. Res., Vol. 28, pp. 493-500.

[41] Silaban, A. and Harrison, D. P., 1995, "High Temperature Capture of Carbon Dioxide: Characteristics of the Reversible Reaction Between CaO(s) and CO_2(g)," Chem. Eng. Comm., Fol 137, pp. 177-190.

[42] Gupta, C. K., Sathiyamoorthy, D., 1999, *Fluid Bed Technology in Materials Processing*, CRC Press, Washington, D. C.

[43] Turkdogan, E. T., Vitners, J. V., 1971, "Gaseous Reduction of Iron Oxides: Part I. Reduction of Hematite in Hydrogen," Metallurgical Transactions, Vol. 2, pp. 3175-3196.

[44] Turkdogan, E. T., Vitners, J. V., 1972, "Gaseous Reduction of Iron Oxides: Part III. Reduction-Oxide of Porous and Dense Iron," Metallurgical Transactions, Vol. 3, pp. 1561-1574.

[45] Szekely, J, El-Tawil, Y., 1976, "The Reduction of Hematite Pellets with Carbon Monoxide-Hydrogen Mixtures," Metallurgical Transactions, Vol 2, pp. 3175-3196.

[46] Ray, Hem Shanker, 1993, *Kinetics of Mettalurgical Reactions*, International Science Publisher, New York, N. Y.

[47] Doherty, R. D., Hutching, K. M., Smith, J. D., Yoruk, S., 1985, "The Reduction of Hematite to Wustite in a Laboratory Fluidized Bed," Metallurgical Transactions B, Vol. 33, pp.425-432.

[48] Loreth, Hana, 2000, "Thermogravimetric Study of Fe_2O_3 powder-CO Gaseous Reduction," Unpublished Report Coal Research Center, Southern Illinois University, Carbondale, IL.

[49] Han, Chun, Harrison, Douglas, 1994, "Simultaneous Shift Reaction and Carbon Dioxide Separation for the Direct Production of Hydrogen," Chemical Engineering Science, Vol 49, pp. 5875-5883.

[50] Han, Chun, Harrison, Douglas P., 1997, "Multicycle Performance of a Single-Step Process for H_2 Production," Separation Science and Technology, Vol 32, pp. 681-697.

[51] Perry, John H.,Chilton, Cecil H., Kirkpatrick, Sidney D.,1963, *Chemical Engineers' Handbook.* 4^{th} ed., McGraw-Hill, New York, New York.

[52] Yates, J.G., 1983, Fundamentals *of Fluidized-be Chemical Processes,* Butterworths, London.

7.0 – NOMENCLATURE

A, B, C, D, D_1:	Concentrations of reactive species (mol-volume^{-1})
A_o, B_o, C_o, D_o, $D_{1,0}$:	Initial concentrations, (mol-volume^{-1})
C_t:	Total concentration, (mol-volume^{-1})
E	Activation energy (kJ-mol^{-1})
M	Molecular (atomic) weight
k_1, k_2, k_3:	Rate constants, (min^{-1})
k_o	Frequency factor (min^{-1})
t:	time (min)
W	mass (g)
α	k_2/k_1
β	k_3/k_1
β_1	k_4/k_1

8.0 – DEFINITION OF VARIABLES

A_v = bed cross-sectional area

c_i = concentration of reactant in the gas stream outside particle

D_e = effective gas diffusivity

d_p = particle diameter

F = fractional mass of oxygen removed

g = acceleration of gravity

K = association factor

k’ =specific rate constant of reaction per unit area of the pore wall

L = bed height

M = molecular weight

M_s = total mass of solids in bed

ΔP = pressure drop

R = radius of solid particle

R_{ep} = particle Reynolds number

S =internal area of porous medium per unit mass

T = temperature

T_c = critical temperature

$T^* = 1.222593\ T_r$

T_r = reduced gas temperature

t = time

u = gas velocity

u_{mf} = minimum fluidization velocity

u_t = terminal velocity

V = volume

V_c = critical volume

ρ_c = critical density

ρ_g = gas density

ρ_p = solid density

ρ_r = reduced gas density = $\frac{\rho}{\rho_c} = \frac{V_c}{V}$

μ = dynamic gas viscosity

ν = kinematic gas viscosity

ϕ_s = sphericity = area of particle/area of sphere of same radius

η = dense gas viscosity (μP)

η_o = low pressure gas viscosity (μP)

Ω_v = viscosity collision integral

$$\xi_T = \left(\frac{T_c}{M^3 P_c^4} \right)^{\frac{1}{6}} \text{ in } \mu P^{-1}$$

$$\mu_r = \frac{131.3\mu}{(V_c T_c)^{\frac{1}{2}}} \square = \text{dipole moment}$$

9.0 – LIST OF ABBREVIATIONS

ACR	Autothermal Cycling Reforming
CaO	Lime
$CaCO_3$	Limestone
DOE	Department of Energy
Fe_2O_3	Hematite
GE-EER	GE Energy and Environmental Research
PEM	Proton Exchange Membrane
SEM	Scanning Electron Microscopy
SIU	Southern Illinois University at Carbondale